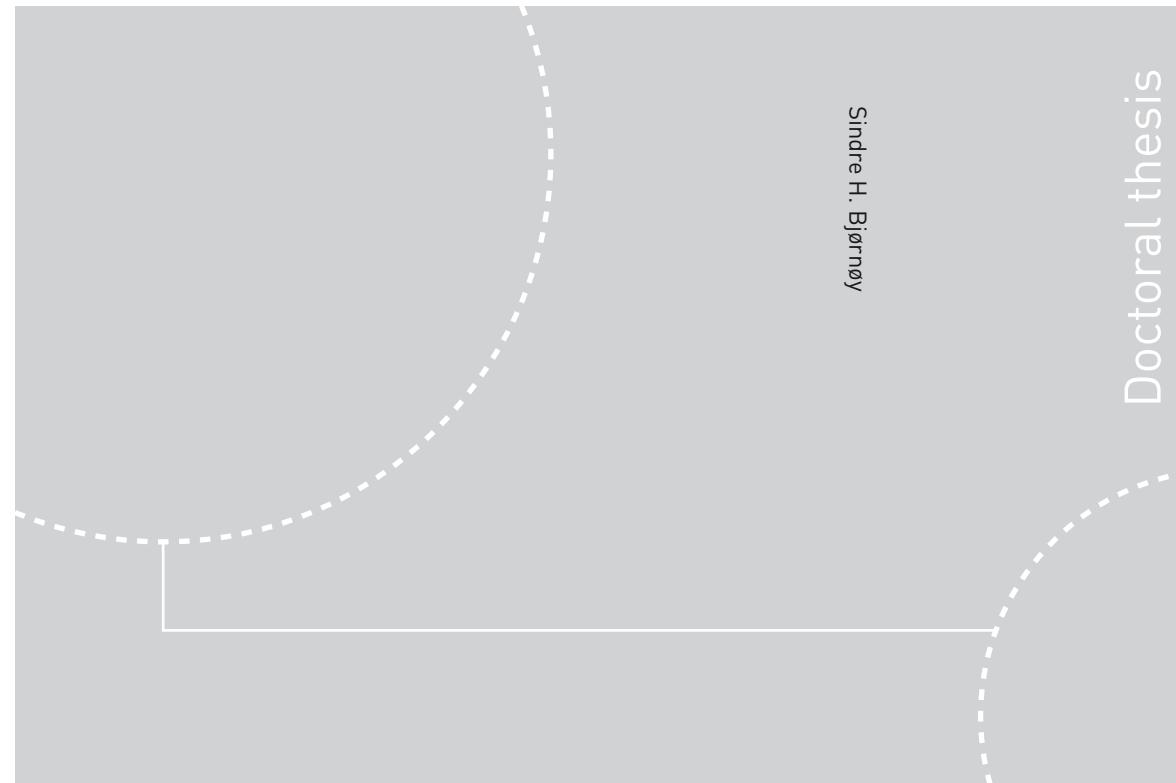


ISBN 978-82-326-2118-7 (printed ver.)
ISBN 978-82-326-2119-4 (electronic ver.)
ISSN 1503-8181



Doctoral theses at NTNU, 2017:18

Sindre H. Bjørnøy

Understanding crystallization in alginate-calcium phosphate composites

Doctoral theses at NTNU, 2017:18

NTNU
Norwegian University of
Science and Technology
Thesis for the Degree of
Philosophiae Doctor
Faculty of Natural Sciences
Department of Physics

 **NTNU**
Norwegian University of
Science and Technology

 **NTNU**
Norwegian University of
Science and Technology

 NTNU

Sindre H. Bjørnøy

Understanding crystallization in alginate-calcium phosphate composites

Thesis for the Degree of Philosophiae Doctor

Trondheim, January 2017

Norwegian University of Science and Technology
Faculty of Natural Sciences
Department of Physics



Norwegian University of
Science and Technology

NTNU

Norwegian University of Science and Technology

Thesis for the Degree of Philosophiae Doctor

Faculty of Natural Sciences
Department of Physics

© Sindre H. Bjørnøy

ISBN 978-82-326-2118-7 (printed ver.)
ISBN 978-82-326-2119-4 (electronic ver.)
ISSN 1503-8181

Doctoral theses at NTNU, 2017:18

Printed by NTNU Grafisk senter

Abstract

Tissue engineering seeks to mimic the properties and functionalities of biological tissue. In the context of bone repair, tissue engineering is becoming an increasingly important science in the active search for synthetic alternatives to autografts. The purpose of this work has been to develop and characterize an organic-inorganic composite material with potential applications within the field of bone tissue engineering. A simple, fast and cell-friendly fabrication of an alginate and calcium phosphate based composite was comprehensively explored and emphasis was put on the development of a thorough characterization protocol. Alginate, a biopolymer well-known for its ionotropic gelation and cell-encapsulation abilities, has been combined with calcium phosphate minerals to explore its potential as a scaffold material for hard tissue applications and as a model system to study mineral formation in the presence of an organic matrix. A one step counter-diffusion method was applied to simultaneously gel the alginate and precipitate the mineral. Characterization of this composite was performed using bulk, end-point techniques such as X-ray diffraction, and thermal gravimetric analysis to investigate mineral phase and content, respectively, as well as *in situ* optical characterization of gelling kinetics and mineralization. The *in situ* studies were performed in a model system to map the spatial distribution of mineral within the composite and the formation and maturation of the mineral crystals primarily using confocal Raman microspectroscopy and confocal laser scanning microscopy. A robust, cell-friendly fabrication protocol for a phase-pure brushite-alginate composite has been developed using brushite seed crystals. Using a correlative characterization scheme with spatiotemporal resolution developed in this work, the mineralization process during the formation of this composite was comprehensively described and shown to include the presence of amorphous calcium phosphate, which quickly dissolved and led to brushite growth in the presence of seeds and conversion to octacalcium phosphate in the absence of brushite seeds. Further maturation led to the formation of thermodynamically stable hydroxyapatite in both cases. The findings in this study may improve the design of scaffold materials based on alginate-calcium phosphate composites and contributes to the understanding of crystallization within hydrogel matrices.

Acknowledgements

I have had the pleasure of receiving support, advice and guidance from many friends and colleagues during my four years as a PhD-student. There is not enough room to thank everyone here, but know that if you are not mentioned, you are not forgotten.

First and foremost I would like to thank my supervisor Pawel Sikorski. He has ensured constant progress during my studies with his motivational and encouraging supervision, and his attention to social activities in our group has made my time at Biophysics a great experience.

I also direct a special thanks to my co-supervisors Berit L. Strand and Jens-Petter Andreassen as well as David C. Bassett and Seniz Ucar. These knowledgeable and skillful people have all been essential to this project, and I would not have been able to complete my PhD without their help and advice.

My fellow PhD-students and office-mates have provided a great academic and social framework during my time at NTNU. Especially Kai, Nina, Sofie, Jonas and Armend and later Peter, Liv, Jacob and Marieke have provided a lot of fun times and moral support on late evenings.

I would also like to thank my family for their support. A special thanks to my wife for always being the wonderful person that you are.

Thank you all!

List of papers

The following publications are included in this thesis.

(I) **Controlled mineralisation and recrystallisation of brushite within alginate hydrogels**

Bjørnøy, S. H., Bassett, D. C., Ucar, S., Andreassen, J-P. and Sikorski, P.
Biomedical Materials, 2016, 11, 015013.

Designed the study: PS, DCB and SHB. Performed the experiments: SHB and DCB. Analyzed the data: SHB and DCB. Contributed materials or analysis: SU. Wrote the paper: SHB and DCB. All authors contributed in the revision and discussion of the paper.

(II) **Gelling kinetics and *in situ* mineralization of alginate hydrogels: a correlative spatiotemporal characterization toolbox**

Bjørnøy, S. H., Mandaric, S., Bassett, D. C., Åslund, A. K. O., Ucar, S., Andreassen, J-P., Strand, B. L. and Sikorski, P.
Acta Biomaterialia, 2016, 44, p243-253

Designed the study: PS, SHB, DCB and SM. Performed the experiments: SHB and SM. Analyzed the data: SHB, PS and SM. Contributed materials or analysis: AKOÅ. Wrote the paper: SHB and PS. All authors contributed in the revision and discussion of the paper.

(III) **A correlative spatiotemporal microscale study of calcium phosphate formation and transformation within an alginate hydrogel matrix**

Bjørnøy, S. H., Bassett, D. C., Ucar, S., Strand, B. L., Andreassen, J-P. and Sikorski, P.
Acta Biomaterialia, 2016, 44, p254-266

Designed the study: PS and SHB. Performed the experiments: SHB. Analyzed the data: SHB. Contributed materials or analysis: SU. Wrote the paper: SHB. All authors contributed in the revision and discussion of the paper.

Related publications

1. **Nucleation and growth of brushite in the presence of alginate**

Ucar, S., Bjørnøy, S. H., Bassett, D. C., Strand, B. L., Sikorski, P., and Andreassen, J-P.

Crystal growth and design, 2015, 15(11), p5397-5405.

2. **Transformation of brushite to hydroxyapatite and effects of alginate additives**

Ucar, S., Bjørnøy, S. H., Bassett, D. C., Strand, B. L., Sikorski, P., and Andreassen, J-P.

Submitted to *Journal of Crystal Growth*, 2016

3. **Letter to the editor Re "Characterization of alginate-brushite in-situ hydrogel composites"**

Bjørnøy, S. H., Bassett, D. C., Ucar, S., Andreassen, J-P. and Sikorski, P.

Materials Science and Engineering C, 2017, 70, p930-931

Published conference abstracts

1. **DCPD-alginate composites: a bioactive material for bone tissue engineering**

Bjørnøy, S. H., Bassett, D. C. and Sikorski, P.

Front. Bioeng. Biotechnol. Conference Abstract: 10th World Biomaterials Congress, 2016

2. **Raman and SEM characterization of early stage calcium phosphate mineral formation in an alginate matrix**

Bjørnøy, S. H., Bassett, D. C., Mandaric, S. and Sikorski, P.

European Cells and Materials, 2015, 29 (Suppl. 1), p4

Contents

Abstract	i
Acknowledgements	iii
List of papers	v
Contents	vii
1 Introduction	1
1.1 Aim of thesis	3
2 Background	5
2.1 Bone	6
2.2 Biomaterials	8
2.2.1 Biopolymers	9
2.2.2 Calcium phosphate	12
2.3 Tissue engineering	13
2.4 Mineralization	16
2.4.1 Classical crystallization theory	17
2.4.2 Non-classical crystallization theory	20
2.4.3 The effect of additives	22
2.5 Characterization of biomaterials	24
2.5.1 Microscopy	25
2.5.2 Spectroscopy	29
2.5.3 Diffraction	32
2.6 Model system for gelling and mineralization	37
3 Summary and discussion of papers	41
3.1 Brief summary of papers	41
3.2 Discussion	44
4 Conclusions and outlook	49

Bibliography	51
---------------------	-----------

Papers	63
Paper I	63
Paper II	81
Paper III	99

Chapter 1

Introduction

Due to an increasing population and life expectancy, treatment of bone related injuries or diseases is increasing. The number of total hip replacements has doubled in the USA during 2000-2010 and in the UK during 2004-2014.[1, 2] Such a procedure involves removing a piece of highly complex material consisting of structured collagen, calcium phosphate nano-crystals, networks of blood vessels and an intricate combination of several cell types, a material otherwise known as bone, and replacing it with a piece of metal. These implants may provide the mechanical support necessary to restore lost function, but are often far from ideal. For example, since a metallic implant is much stiffer than bone stress shielding can occur which leads to reduced density of the surrounding bone which in turn can lead to implant failure. Biological tissues are complex materials consisting of many different cell types, extracellular matrix, blood vessels and signaling systems in a dynamic environment. In contrast, a metal implant is a static, simple material. In the search for better alternatives for implant materials, engineered scaffolds combined with cells and relevant growth factors to better match and mimic biological materials are being investigated. This intriguing and relatively new branch of science is termed tissue engineering.

Bone has a remarkable ability to heal itself, although the self-healing capabilities have their limits. Large bone defects, trauma injuries and the attachment of implants often require surgical intervention. The gold standard treatment for bone repair is transplantation of autologous bone, which involves taking a piece of healthy bone from the patient, often from the mandible or the iliac crest, and transplanting it to the affected site. The autologous bone, called an autograft,

has little risk of immune rejection and may promote the growth of new bone. However, the procedure requires a second surgical site, there is a risk of donor site morbidity and the amount of transplantable bone is limited. Alternatives to autografts include allografts and xenografts, which are bone grafts from other humans or animals, respectively. Allografts and xenografts have a higher risk of graft rejection in addition to a risk of transferable diseases. As the supply of these graft types are limited, a synthetic graft would be preferable, and it is for this reason synthetic tissue engineering scaffolds receive a great deal of attention.

This thesis concerns the development of organic-inorganic composite materials made from alginate and calcium phosphate (CaP), inspired from the naturally occurring matrix found in bone. Alginate is well known for its cell-encapsulation properties and low immunogenicity which make this material an excellent candidate in tissue engineering applications. Recent developments in gelling strategies has also rendered alginate as a viable candidate for 3D-printing.[3] Composites with alginate and CaP have been proposed for a variety of biomedical applications. For example, L  v  que *et al.* formed a CaP shell via counter-diffusion around alginate spheres to improve mechanical strength and to reduce the burst release of encapsulated drugs.[4] Despang *et al.* investigated the formation of aligned pores in cylinders made from pure alginate, alginate with incorporated hydroxyapatite (HAp) powder and alginate with *in situ* mineralized HAp.[5] These structures were intended as anisotropic scaffolds allowing for cell migration and vascularization. The *in situ* mineralized scaffolds endured a 20 % higher compression load than non-mineralized and powder-alginate mixture scaffolds. It has also been shown that alginate-CaP composites made via enzyme-mediated mineralization had increased mechanical properties and promoted osteoblastic differentiation of encapsulated human mesenchymal stem cells.[6, 7]

The alginate-CaP composite in this work is intended as a building block of a scaffold for bone tissue engineering. The ability to form beads, fibers and films with or without mineral content combined with the ability to encapsulate live cells results in a system with a large degree of flexibility in terms of scaffold design. The material itself can also be used as a model system for 3D-cell culturing for non-proliferating cells such as osteocytes, or to study mineral formation. To explore the potential of such a composite, detailed knowledge of fabrication parameters are needed. The degree of mineralization, polymorphism and stability of the formed mineral are properties of interest. Gel formation and kinetics are also important

factors in the system which require study. Characterization of the aforementioned properties and fabrication strategies for such a composite material are explored within this thesis.

1.1 Aim of thesis

The overall aim was to develop and characterize an alginate-calcium phosphate composite material with applications as a scaffold material and a model system for mineralization and 3D-cell culture.

To achieve this, more specific aims were to

- Develop fabrication protocols for alginate-CaP composites with brushite as the inorganic phase.
- Establish a model system and characterization protocols to study the mineral amount, mineral phase and morphology within the composite material.
- Study the gelling kinetics and investigate the effect of mineralization.
- Understand the mineral maturation process within the hydrogel during *in situ* mineralization and upon storage.

In this thesis, the concepts of biological materials, biomaterials and tissue engineering are introduced and some history and development of the research within these fields are presented. The theory of mineral formation is discussed in terms of classical crystallization theory and some aspects of non-classical crystallization theory. Mineralization in the presence of additives is also introduced. The alginate-CaP composite is discussed both as a biomaterial and in the context of mineralization. Further, some theory and important aspects in order to understand the capabilities and limitations of the characterization techniques used in this work are presented. Thorough characterization of the material is central in all of the papers included in this thesis and is important in order to assure the reproducibility of the results. The content of the papers are then presented and discussed in a broader context than in the individual papers. Results from related publications are also brought into this discussion in order to shed light on certain observations. Finally some conclusions are drawn and future outlooks explored.

Chapter 2

Background

Biological tissues are often recognized for their complex structure and outstanding properties. Order is present at a range of length scales, known as hierarchical structure, and the materials are often optimized with respect to several competing factors, for example stiffness, toughness and reduced weight. There are many examples of composite materials with remarkable mechanical properties in Nature. Such natural composites are made by combining the stiffness of minerals with the toughness of polymers. Nacre, also called mother of pearl, found in the inner layer of mollusks consists of 95 % aragonite and 5 % organic matter. The fracture toughness of nacre is up to nine times higher than pure aragonite.[8] The

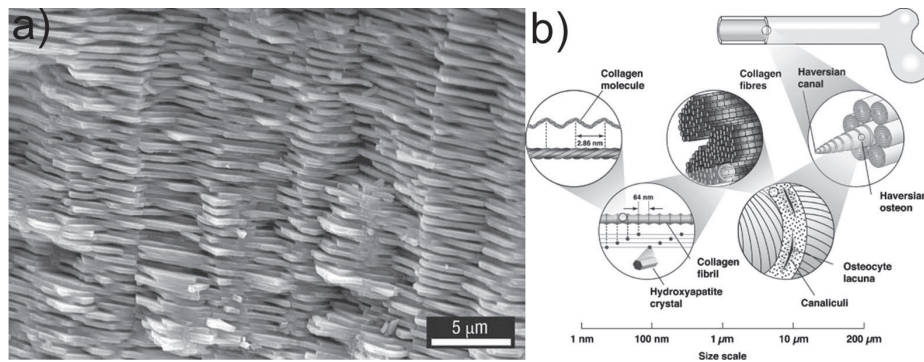


FIGURE 2.1: **a)** The brick and mortar structure of nacre; aragonite tablets surrounded by an organic matrix. **b)** A schematic depicting the complex hierarchical structure of bone. Image **a)** from [9]. Reprinted with permission from AAAS. Image **b)** from [10]. Copyright 2016 John Wiley and sons.

structure of this composite resembles the brick and mortar design engineers use for building walls. A scanning electron microscope image with micro scale aragonite

"bricks" can be seen Figure 2.1 a. When fracture occurs, the energy of the crack is dissipated into the tough organic matrix which reduces crack propagation. Another example of a biological material with remarkable architecture is the biosilica of the hexactinellid sea sponges. Aizenberg *et al.* described the structure of one sponge species and found a hierarchical design ranging from the nanoscale to the macroscale, see Figure 2.2.[11] The structure of bone has also been described by several researchers and as for many other biological composite materials, the properties of bone stem from the structuring of an organic network in combination with an inorganic mineral phase, as can be seen in Figure 2.1 b and described in more detail in the following section.[10, 12, 13]

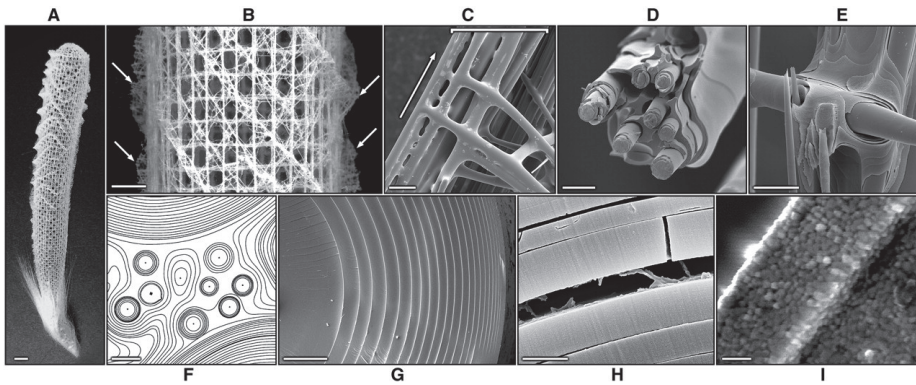


FIGURE 2.2: The mineralized skeletal system of the sea sponge *Euplectella* sp. **a)** The entire structure. Scale bar 1 cm. **b)** A magnified part of the cage structure. Scale bar 5 mm. **c)** An SEM image showing that each of the struts in the cage structure are made up from several smaller struts called spicules. Scale bar 100 μm . **d)** A partially etched single beam, showing the organization of internal spicules. Scale bar 20 μm . **e)** Partially etched junction revealing its layered structure. Scale bar 25 μm . **f)** Contrast-enhanced SEM image of the cross-section of a strut. Scale bar 10 μm . **g)** Cross-section of a single spicule showing a layered structure. Scale bar 5 μm . **h)** Higher magnification image of a spicule cross-section showing an organic matrix. Scale bar 1 μm . **i)** An image showing the nanoparticulate structure of the spicules. Scale bar 500 nm. From [11]. Reprinted with permission from AAAS.

2.1 Bone

One of the most striking features of bone is its structural complexity, ranging from the triple-helix tropocollagen molecules and oriented hydroxyapatite nanocrystals within collagen fibrils via larger fibers and arranged lamellar sheets all the way to

the macroscopic level of the bones we can see with the naked eye.[13] A schematic figure of this can be seen in Figure 2.1 b. This complex structural design is combined with the functional interplay between osteoblasts, osteoclasts and osteocytes in a highly vascularized, dynamic tissue, see Figure 2.3.[14] Bone is in a constant

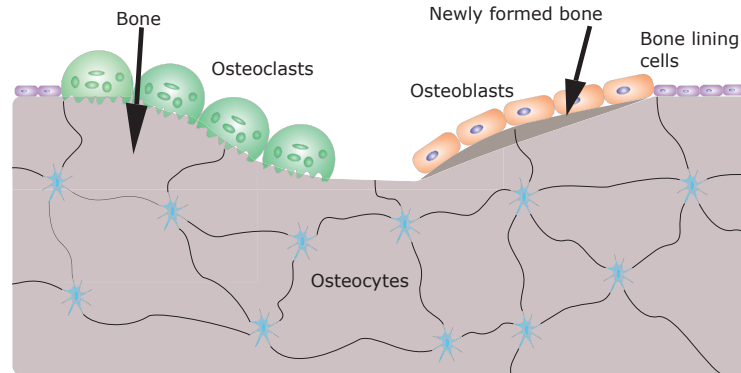


FIGURE 2.3: A schematic of bone homeostasis. Osteoclasts resorb existing bone, osteoblasts form new bone and osteocytes regulate the relative activity between resorption and bone formation. Blood vessels and bone structure have been omitted for simplicity.

state of remodeling, where new bone is formed as old bone is removed, a situation called bone homeostasis.[15] Upon trauma, the activity of these different cell-types can be altered to increase the rate of bone formation and heal minor fractures and injuries.[16] This is one aspect where tissue engineering seeks to improve upon more conventional treatment strategies, like metal implants, which are not resorbed *in vivo* and are prone to failure after a given amount of time. The self-healing property, a result of being a living tissue, is something the scientific community strives to mimic. Although progress has been made for polymeric materials, the multi-stage self-healing mechanisms of biological materials are far from realized in synthetic materials.[17]

The composition of bone varies depending on the type of bone, however, for compact bone it is generally accepted that the distribution of constituents is approximately 60-70 % mineral, 10 % water and the rest is organic content.[18] Although most of the organic content is collagen, approximately 10 % consists of what is known as non-collagenous proteins. These include proteoglycans, albumin, osteocalcin, osteopontin, bone sialoprotein and alkaline phosphatase.[19] Common for many of these proteins is their highly acidic nature and relatively small size (<50 kDa). Although the exact functions of the non-collagenous proteins are not fully

known, some of them have been shown to improve the efficiency of intra-fibrillar mineralization of collagen. This is described in more detail in section 2.4.3.

2.2 Biomaterials

A biomaterial does not, despite its name, have to be a biologically derived material. Historically, the word biomaterial has been used to describe any material used to restore, repair or augment damaged, lost or inadequate biological function. In this regard sutures, metal wires, gold teeth, titanium implants etc. are all considered biomaterials. Common for all of these is the lack of complexity as compared to biological materials. Currently, it is not possible to synthetically produce a material with the exact same properties as a true biological material. By elucidating important structural and functional elements from natural materials and employing these in the design process, one aims to improve the quality and effectiveness of biomaterials.

The definition of a biomaterial has changed several times based on the function and intended usage. Today, the development of biomaterials is categorized into three generations. The very first biomaterials were typically developed to be as inert as possible to not induce inflammatory responses. Hench provided an early definition in 1980 stating that the goal of biomaterials are to "achieve a suitable combination of physical properties to match those of the replaced tissue with a minimal toxic response in the host".[20] Later on, a second generation of biomaterials emerged, with a shift of focus from inertness to evoke a controlled reaction in a specific tissue by the incorporation of bioactive components. A typical example of such a biomaterial is bioactive glass, known for its bone-bonding abilities.[21] The release of metallic ions upon dissolution provides ions necessary for bone formation as well as triggering a range of cellular response, ranging from promoting osteoblast proliferation to increasing the expression of growth factors.[22] Another class of materials that emerged in the second generation of biomaterials was resorbable polymers. To combat the foreign body response, which can lead to fibrous encapsulation of an implanted biomaterial, the strategy for resorbable polymers was to create a material which degraded controllably and was gradually replaced by native tissue.[23, 24] For example, poly(lactic-co-glycolic) acid (PLGA) has received a great deal of interest due to its tunable degradability and compatibility with rapid prototyping technology (3D-printing).[25, 26] The third generation of

biomaterials seek to stimulate specific cellular responses at the molecular level.[27] The promising developments from the second generation were combined in the third generation, making bioactive, resorbable biomaterials. In addition, moieties designed to direct cell proliferation or differentiation may be incorporated in the materials to further facilitate the desired *in vivo* response.[28] Williams has tried to incorporate the recent developments in his dictionary and the modern definition of a biomaterial is a "material intended to interface with biological systems to evaluate, treat, augment or replace any tissue, organ or function of the body".[29] It is likely that future generations of biomaterials will continue this trend of increasing complexity to better mimic the form and function of the natural tissues as our knowledge of both natural processes and synthesis technology improves.

2.2.1 Biopolymers

The organic matrix in bone consists mainly of collagen, a molecule made from three polypeptides with large fractions of glycine, proline and hydroxyproline. There are many types of collagen (so far 28 have been identified), however, bone contains mostly collagen type I.[30] In bone, the collagen self-assembles into a hierarchical, fibrillar structure which is subsequently mineralized with aligned hydroxyapatite crystals. This fibrillar structure is recognized by an axial periodicity of 67 nm, often termed the banding structure, as it can be observed as transversal bands in electron- and atomic force microscopy. This banding pattern is a result of the shift of neighboring collagen molecules within a fibril, and consist of an overlap region and a gap region, see Figure 2.4. Collagen is a major part of the extracellular matrix in bone, tendons and skin. In addition to providing mechanical support, collagen also affects cell proliferation and differentiation.[31] Cell attachment often occurs, via integrins, to collagen or other ECM components such as fibronectin.[32]

Alginates are a family of polysaccharides derived from seaweed and, in some cases, bacteria. The chemical structure consists of β -D-mannuronic acid residues and its C5-epimer α -L-guluronic acid, termed M and G, respectively. Repeated sequences of G-units, termed G-blocks, have the ability to bind multivalent cations and in the presence of, for example, calcium ions, alginate chains can be physically cross linked by complexing calcium ions between G-blocks. The cross-linking of multivalent cations by alginate have been termed the egg-box model and binds two

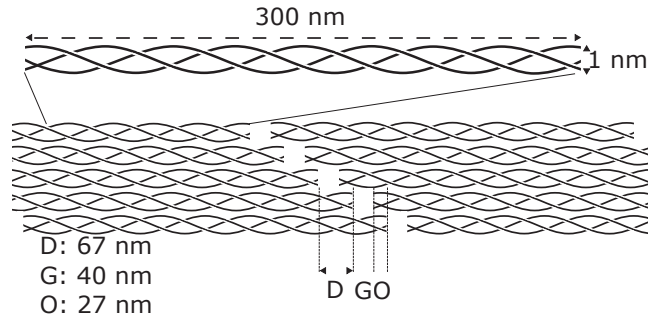


FIGURE 2.4: A schematic representation of a collagen molecule (top) and a collagen fibril (bottom) showing the dimensions of the periodicity, D, the gap region, G, and the overlap region, O.

or more alginate chains together, sometimes referred to as dimers and n -mers.[33] In this case, "mers" refer to whole alginate chains in contrast to conventional polymer-chemistry where (mono)mer usually means a single building block, like the G- and M-residues. The exact mechanism of how this happens is still under debate, and two schemes for this formation are shown in Figure 2.5. It has also been shown that alternating MG-blocks can form cross-links, and a similar egg-box model has been suggested.[34] The binding of calcium is thought to be of a cooperative nature, that is to say that once a calcium ion has formed a complex between four G-residues from two different alginate chains, the neighboring GG-Ca-GG complex between these two chains will form more easily. A suiting analogy is the zipper on a coat; it may take some time to get the two parts together, but once it is aligned closing the zipper requires much less effort.

The ability to form hydrogels at mild conditions in combination with its low toxicity and low immunogenicity has made alginate a popular choice for cell encapsulation.[36] The alginate acts as a semipermeable membrane which allows the exchange of nutrients, waste and wanted biomolecules, but protects the implanted cells from immune rejection without the need for immunosuppressive drugs. In order for such cell implants to be effective, one must control the pore size and the stability of the gel. Typically, the cells have no means of binding to or remodel the alginate gel, although it has been shown that the structure of alginate microcapsules can be disturbed by proliferating cells.[37] For other applications, such as an ECM-mimic cell-alginate interactions may be desired. By attaching oligopeptides of arginine, glycine and aspartic acid (RGD), a sequence recognized for its integrin-binding, cell-attachment to alginate may be improved.[38, 39] Work by

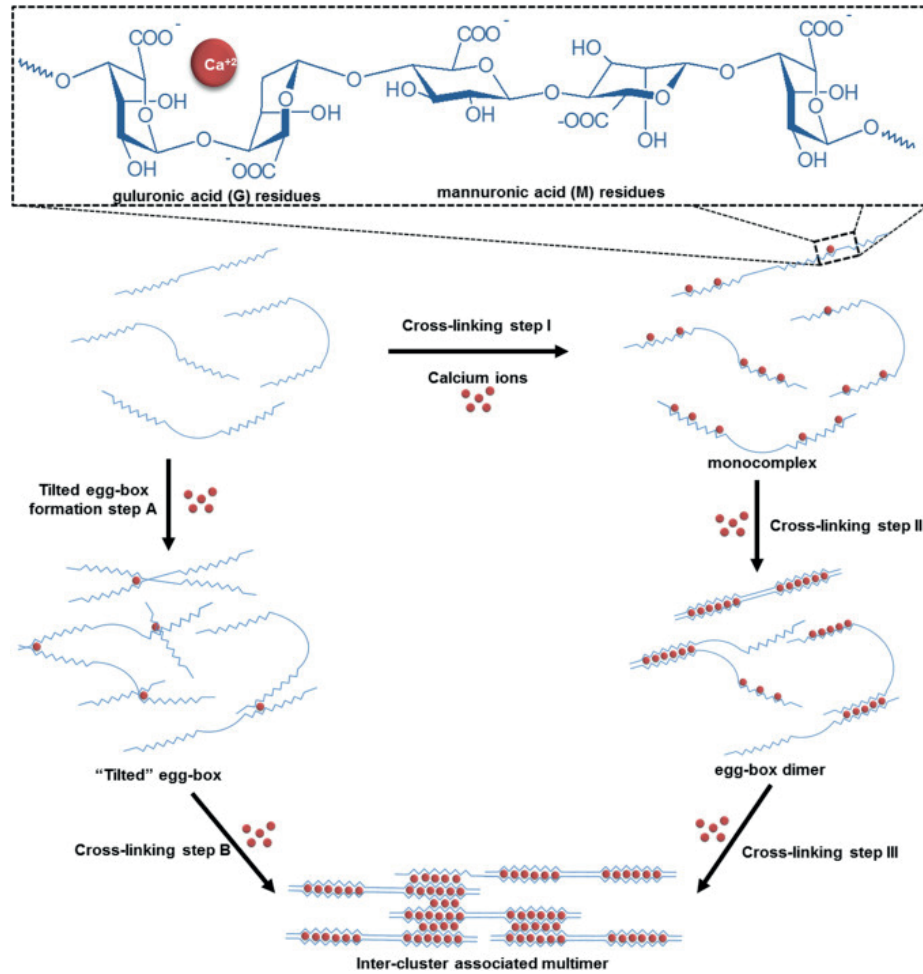


FIGURE 2.5: A schematic of alginate cross linking via a divalent cation such as calcium. Reprinted from [35], Copyright 2017 with permission from Elsevier.

Evangelista *et al.* has also shown that RGD-modified alginate can improve the attachment and differentiation of bone cells as compared to un-modified alginate.[40]

Other uses of alginate include a wide range of application such as a thickening agent or emulsifier, dental impression material, wound dressings and as a drug delivery vehicle.[41–44] The degradability of alginate gels can also be altered by changing the molecular weight of the polymer chains, or through partial oxidation.[41] Due to the versatility of alginate it is likely to remain a prevalent biomaterial of choice in future applications as a cell or drug delivery vehicle, scaffold material or ECM model for cell studies.

2.2.2 Calcium phosphate

The biominerals in focus of this work are the CaP-minerals, specifically the calcium orthophosphates, a complex system with several different crystallographic phases. In a biological context, the most relevant phases are (1) hydroxyapatite (HAp), which in Nature almost exclusively appears as calcium-deficient carbonate substituted HAp, found in bone, teeth and tendons, (2) octacalcium phosphate (OCP) and (3) amorphous calcium phosphate (ACP) both found as precursor phases in mineralization processes and (4) brushite (DCPD) found in pathological calcifications.[45] Depending on the Ca/P ratio (often determined by the acidity in the precipitating solution), several structures of ACP has been proposed, namely amorphous tricalcium phosphate (ATCP), ACP1 and ACP2.[46] Common for these are a labile nature and a lack of long-range order.

The CaP system also includes several other phases, some of which do not occur naturally, but are used as biomaterials due to their osteoconductive properties (for example β -tricalcium phosphate (β -TCP), tetracalcium phosphate (TTCP) and monetite (DCPA)).[47] An overview of several important properties of the different phases mentioned here can be seen in Table 2.1.

TABLE 2.1: An overview over some of the biologically relevant CaP-phases. Solubility values from [46, 48–51].

Name	Chemical formula	Ca/P ratio	Lattice system	Solubility (pK _{sp})
DCPD	CaHPO ₄ ·2H ₂ O	1.00	Monoclinic	6.6
DCPA	CaHPO ₄	1.00	Triclinic	6.9
ACP1	-	1.15-1.35	-	25.5
OCP	Ca ₈ H ₂ (PO ₄) ₆ (OH) ₂ ·5H ₂ O	1.33	Triclinic	48.4
ACP2	Ca(PO ₄) _{0.74} H _{0.22}	1.35	-	28.3
ATCP	Ca ₃ (PO ₄) ₂ ·nH ₂ O	1.5	-	24.8-26.5
β -TCP	Ca ₃ (PO ₄) ₂	1.50	Rhombohedral	28.9
HAp	Ca ₁₀ (PO ₄) ₆ (OH) ₂	1.67	Hexagonal	57.5
TTCP	Ca ₄ (PO ₄) ₂ O	2.00	Monoclinic	38.0

Early work regarding CaP- granules as bone fillers was mainly focused on HAp, as this is the mineral found in bone, and β -TCP.[52] The use of CaP-cements, CaP powders in combination with water which hardened upon mixing, became popular after their discovery in the mid 1970's.[53] CaP-cements are popular in non-load bearing applications due to their ease of use and clinical performance.[54]

The cements can be applied as injectable pastes via non-invasive surgical procedures and these pastes are also compatible with 3D-printing technologies enabling the fabrication of complex, individually tailored scaffolds.[55, 56] Despite many starting formulations, CaP-cements can in essence have two end-products, HAp or brushite (ACP is also possible, but will quickly convert to HAp).[52] The more soluble brushite cement was discovered by Mirtchi *et al.* in 1989.[57] The higher solubility of brushite leads to a more resorbable cement, and therefore brushite cements have received considerable attention.[58, 59] The use of brushite offers the possibility to provide a higher amount of relevant ions to the surrounding cells, however, larger constructs risk losing this ability by conversion to more stable CaP-phases.[60] The drawbacks of CaP-cements include their dense and brittle nature which may lead to poor resorption and fracture. In an attempt to improve the performance of a CaP-cement, Chen *et al.* used a macroporous cement in combination with prevascularization done in a co-culture of human umbilical vein endothelial cells (HUVEC) and human osteoblasts (HOB).[61] This resulted in the formation of micro capillary-like structures which are likely to improve the successful implantation of such a material. The increase in complexity of this material compared to a regular cement, a trend seen across the entire field of biomaterials is again evident in this case.

2.3 Tissue engineering

Tissue engineering is a branch of science concerned with mimicking natural tissue, and can be seen as a natural development of ever more advanced biomaterials. In their now famous 1993 Science paper, Langer and Vacanti paraphrase Skalak & Fox and Nerem and provide the often cited definition of tissue engineering: "Tissue engineering is an interdisciplinary field that applies the principles of engineering and the life sciences toward the development of biological substitutes that restore, maintain, or improve tissue function".[62–64] This definition is more reminiscent, even today, of science fiction rather than science. The idea that we can improve tissue function, i.e. make muscles stronger, bones more durable or hearts pump more blood at a higher rate is still not a reality. However, restoration of tissue function is more achievable and the field has made some remarkable progress in the last decades. For example, Vegas *et al.* were able to restore glycemic control

in diabetic mice for a period over 174 days by encapsulating glucose-responsive β -cells in chemically modified alginate.[65]

In its core, tissue engineering relies on the interplay between cells, signaling molecules or growth factors and a material providing mechanical support, often termed a scaffold.[66] The cells can either be native cells from the implant site or implanted cells seeded onto the scaffold.[67, 68] The scaffold may be synthetic, biologically derived or even decellularized extra-cellular matrix (ECM).[69–71] The ideal result is a construct which, at the time of implantation, fulfills the function of the replaced tissue while over time is degraded and replaced by healthy tissue.

Research activity in the field of tissue engineering has soared during the last two decades. Figure 2.6 shows a plot of the number of publications within the topics tissue engineering or regenerative medicine between 1990 and 2015, based on statistics from Web of Science. Despite the large activity, clinical examples of bone

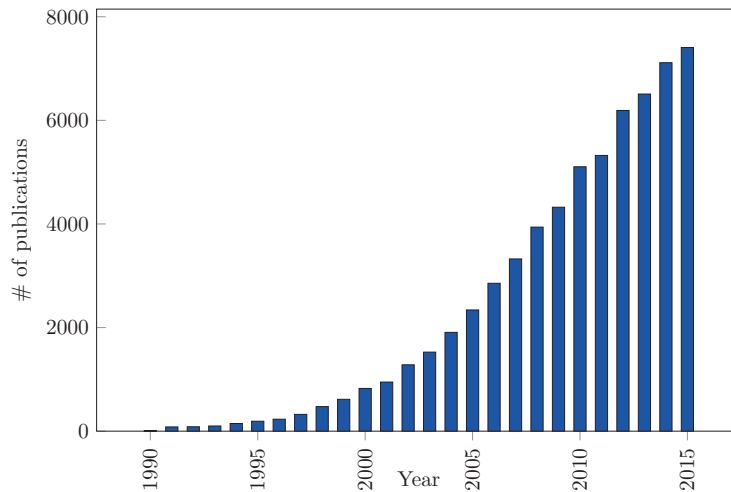


FIGURE 2.6: A plot of the number of publications with topics "tissue engineering" or "regenerative medicine" from 1990-2015. Data from ISI Web of Science (obtained October 2016).

tissue engineering, especially in load-bearing applications, remain scarce, although there are some promising pre-clinical results. Kolambkar *et al.* combined an electrospun polycaprolactone mesh cylinder filled with an alginate hydrogel with the local release of the growth factor bone morphogenetic protein-2 (BMP-2) in order to repair a critically sized defect in a rat model.[72] The results showed a significant increase in bone growth and the mechanical properties of the healed bone

was comparable to intact bone. Other strategies have also been investigated such as using demineralized bone matrix from different sources.[73] Liu *et al.* recently reviewed clinically relevant bone scaffolds and presented a range of regulatory approved bone graft solutions.[74] Many of these are based on demineralized bone matrices, and therefore limited in supply. However, one of the highlighted examples is a polycaprolactone scaffold from the company Osteopore (Singapore), which was integrated and started to mineralize upon implantation.[74–76] Although the path is long from these examples to routine clinical procedures, these results are encouraging for the scientists working within the field, who can see that the next milestone moves a little closer every day.

There are several requirements for an ideal bone scaffold material. Khan *et al.* lists five attributes which should be present in order to regenerate bone tissue; (1) biocompatibility - in this regard meaning low immunogenicity, (2) osteoconductivity - the materials ability to direct bone growth, (3) osteoinductivity - the materials ability to induce the differentiation of osteoprogenitor cells into osteoblasts via growth factors and proteins, (4) osteogenicity - the osteoblasts present are able to produce minerals and produce new bone and (5) osteointegration - the ability to form a solid bond between the newly mineralized tissue and the scaffold.[77] In addition to these requirements the scaffold should match the mechanical properties of bone, degrade at a rate comparable to the ingrowth of new bone, have an interconnected pore structure to allow migration of cells and promote vascularization.[24] It is evident that hydrogels do not comply with all of these requirements, especially with regards to mechanical properties. Nevertheless, hydrogels possess several key capabilities as a tissue engineering biomaterial and could be well considered as a component of a multimaterial solution. They can in many cases be introduced *in vivo* through injectable systems allowing for minimal invasive procedures.[78] The application of drug delivery using hydrogels as a controlled release matrix is a very active area of research.[79] An alginate hydrogel loaded with BMP-2, a growth factor relevant for bone formation, was shown to improve the bone forming compared to delivery with a collagen sponge.[80] The use of BMP-2 is, however, connected with controversy due to apparent under-reported adverse reactions.[81] The concentration of BMP-2 in some of the clinical applications were up to 2 mg/ml, while the normal serum level is in the pg/ml range.[82, 83] This large difference in concentration may be connected to some of the adverse effects observed. Considering the drug-delivery capabilities combined with the cell-encapsulation abilities

of certain hydrogels, it is evident that hydrogels have a large potential within the field of tissue engineering.

2.4 Mineralization

Nature incorporates inorganic constituents as a hardening and stiffening mechanism in many biological materials, resulting in well-designed composites. The combination of high strength and low weight, all produced in ambient conditions has inspired scientists and engineers for a long time. There is a range of known biominerals, some of which are shown in Table 2.2 although the most common are calcium based. A common scheme for the formation of mineralized tissue is the formation of a structural template consisting of an organic matrix which directs the formation of mineral crystals. This leads to highly organized hierarchical composite materials, for example diatom frustules, nacre and bone.[8, 12, 84] For a mineral crystal to form from a solution there has to be a driving force. The driving force for crystal formation is known as supersaturation, or the difference in chemical potential between the chemical constituents in solution and in the crystal phase.[85] The relative supersaturation is often used and is given as follows:

$$\sigma = S - 1 = \left(\frac{\text{IAP}}{K_{sp}} \right)^{1/\nu} - 1 \quad (2.1)$$

S denotes supersaturation, IAP is the ion activity product, K_{sp} is the solubility product and ν is the number of ion species in the crystal formula. From this we can see that the supersaturation is related to the concentration of a species via the activity product and that the supersaturation of a specific crystal phase is related to the solubility product of this phase, i.e. different crystal polymorphs can have different relative supersaturation depending on conditions such as pH and ionic strength. In addition to the chemical constituents of the mineral itself, biomineralization involves biomolecules which may inhibit or promote nucleation, promote the growth of certain crystal facets or change the crystallographic phase which is precipitated at certain conditions.[86–88] More passive effects such as confinement may also affect the polymorphism, morphology and orientation of crystals.[89–91] It is also important to note that a mineral does not need to exist in a crystalline form. Amorphous phases with no long-range order have been observed for many

mineral systems. These amorphous phases are often unstable and occur as precursor phases. According to Ostwald's rule of stages, it is the least stable phase which nucleates first in a supersaturated environment.[92] The role of amorphous phases in biological mineralization has been and still is under investigation.[93–95] A brief introduction to crystallization theory and the influence of additives is given below.

TABLE 2.2: A non-exhaustive list of different known biominerals. Adapted from Mann.[96] It is noted here that HAp exists in the form of calcium-deficient HAp in most vertebrates.

Mineral	Formula	Typical organism	Function
HAp	$\text{Ca}_{10}(\text{PO}_4)_6(\text{OH})_2$	Vertebrates	Endoskeleton
OCP	$\text{Ca}_8(\text{PO}_4)_6\text{H}_2\cdot 5\text{H}_2\text{O}$	Vertebrates	Precursor phase
ACP	Variable	Vertebrates	Precursor phase
Calcite	CaCO_3	Coccolithophores	Exoskeleton
Aragonite	CaCO_3	Corals	Exoskeleton
Vaterite	CaCO_3	Snails	Exoskeleton
ACC	$\text{CaCO}_3 \cdot n\text{H}_2\text{O}$	Crustaceans	Mechanical strength
Silica	$\text{SiO}_2 \cdot n\text{H}_2\text{O}$	Diatoms	Exoskeleton
Gypsum	$\text{CaSO}_4 \cdot 2\text{H}_2\text{O}$	Jellyfish	Gravity receptor
Celestite	SrSO_4	Acantharia	Micro-skeleton
Barite	BaSO_4	Loxodes	Gravity receptor
Magnetite	Fe_3O_4	Bacteria and chitons	Magnetoaxis and abrasive teeth

2.4.1 Classical crystallization theory

The formation of a mineral crystals starts with a nucleation event and the addition of further ions leads to a growing crystal. Classical crystallization theory describes this as the formation of a cluster of molecules above a critical size in a supersaturated solution. For a spherical cluster, or nucleus, with radius r , the change in chemical potential related to the formation of a particle of a certain volume and a surface energy term is given by:[97]

$$\Delta G = \frac{4}{3}\pi r^3 \Delta G_v + 4\pi r^2 \gamma \quad (2.2)$$

Here, ΔG is the total free energy, r is the nucleus radius, ΔG_v is the Gibbs free energy per unit volume of the solid phase and γ is the surface energy per unit

area. From this we can see that a formed nucleus is stable if the radius is above a critical size, r^* , see Figure 2.7. The nucleation and growth of crystals will continue as long as the solution is supersaturated. However, the rate of nucleation is given by:[98]

$$J = A \exp \left(-\frac{16\pi\gamma^3\nu^2}{3k^3T^3\ln(S)^2} \right) \quad (2.3)$$

where ν is the molecular volume, k is the Boltzmann constant and T the temperature. The growth rate is shown in Equation 2.4. It can be seen from Equation 2.3 that for low supersaturation (S close to 1 and σ close to 0) the nucleation rate has a sharp drop towards 0, while the growth rate is a parabolic function which decreases more steadily towards zero. This means that at low supersaturation, the available chemical species are consumed by growth of existing crystals and no new crystals will nucleate.

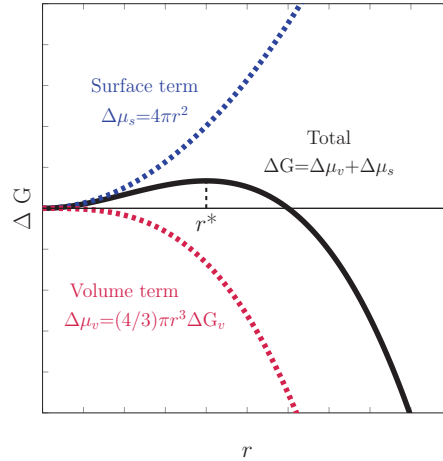


FIGURE 2.7: A schematic representation of Equation 2.2 showing the change of volume free energy, surface free energy and total free energy as a function of nucleus radius. The position of the critical sized nucleus is marked with r^* .

Crystal growth described by classical theory is divided into two processes; diffusion-limited growth and growth controlled by surface process.[97] The first case involves generation, diffusion and adsorption onto the crystal surface of the growth species. The second case involves the incorporation of these species into the solid crystal. A key assumption in classical crystallization theory is that crystal growth occurs via the attachment of monomer units. The rate of growth is described as:[98]

$$R = k\sigma^g \quad (2.4)$$

where k denotes a growth constant, σ denotes the relative supersaturation given in Equation 2.1 and g is the apparent order of growth. The apparent order of growth may provide information about the growth mechanism of a crystal. Several growth mechanisms have been proposed. Volmer envisioned an absorption layer at the crystal surface where solute atoms did not attach immediately, but merely lost one degree of freedom, i.e. surface diffusion could still occur.[98] After some time the atom could be integrated into the crystal lattice, most readily at a kink or a step in the lattice (Kossel model). This process would repeat until a complete layer covered the crystal surface and further growth could continue after a 2D-nucleation event on the complete surface. The reliance on nucleation events led this theory to underestimate crystal growth, especially at low supersaturation. For example, iodine crystals can be grown at 1 percent supersaturation at rates 10^{1000} times greater than predicted by this theory (Volmer and Schultz 1931 as referenced by Mullin).[98] A development on this model was introduced by Frank who suggested a screw dislocation in the flat crystal surface.[99] Such a feature would induce spiral growth of the crystal, and would always contain active sites where incorporation of new atoms into the lattice occur, removing the need for a nucleation event on a completed surface layer. Such spiral growth has been observed in many crystal systems, including α -Co(OH)₂, Ni(OH)₂ and gold (see Figure 2.8). It has been found that the apparent growth order for spiral growth is 2 at low supersaturation and 1 at high supersaturation.[98] If the growth order is above 2, it suggests that 2D-nucleation or island formation on the crystal surface may occur.

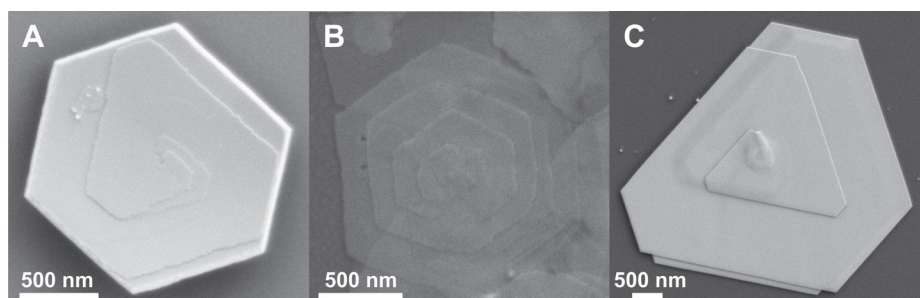


FIGURE 2.8: SEM-images of spiral growth on nanoplates of (a) α -Co(OH)₂, (b) Ni(OH)₂ and (c) gold. Reprinted with permission from [100]. Copyright 2011 American Chemical Society.

The classical theory adequately describes growth of crystals in well-defined systems, however, the remarkable single crystal morphologies observed in biomineralization, for example the coccolithophores, is hard to explain by mechanisms relying on monomer attachment. This has led to the development of several theories describing other mechanisms for crystal growth presented in the following section.

2.4.2 Non-classical crystallization theory

From a thermodynamic standpoint, the shape of any crystal formed via a classical pathway should ultimately reflect its unit cell. Different morphologies can arise, due to differences in surface energies of the crystal facets or a local difference in supersaturation. For example a snowflake reflects the hexagonal crystal structure of ice, but a diffusion-limited supply of water molecules leads to a dendritic growth of the crystal. There are, however, certain crystals which cannot be explained by thermodynamic and kinetic effects based on classical crystal growth. Meldrum and Cölfen list four examples of non-classical crystallization processes, namely the formation of intermediary clusters or liquid precursors as building blocks, crystallization via amorphous building blocks, oriented attachment of preformed crystalline building blocks and the formation of mesocrystals.[101]

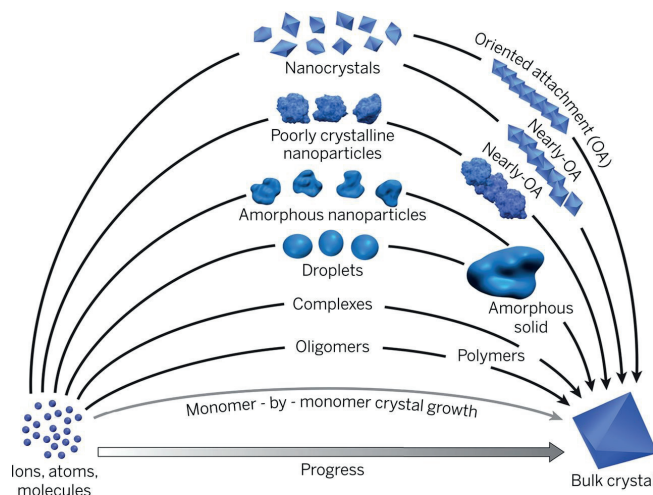


FIGURE 2.9: Suggested pathways for crystallization. From [102]. Reprinted with permission from AAAS.

Gong *et al.* showed convincing examples of oriented attachment of iron pyrite where either nanocrystals or nanosheets fused and formed larger cubic single crystals upon heat treatment, see Figure 2.10.[103] Meng *et al.* prepared $\alpha\text{-Fe}_2\text{O}_3$ crystals in the presence of sodium oleate and oleic acid in a hydrothermal synthesis.[104] The resulting crystals formed straight mono-crystalline chains of truncated bipyramidal crystals. These chains are reminiscent of chains of magnetic Fe_3O_4 found in magnetotactic bacteria, although these chains are not fused. [105]

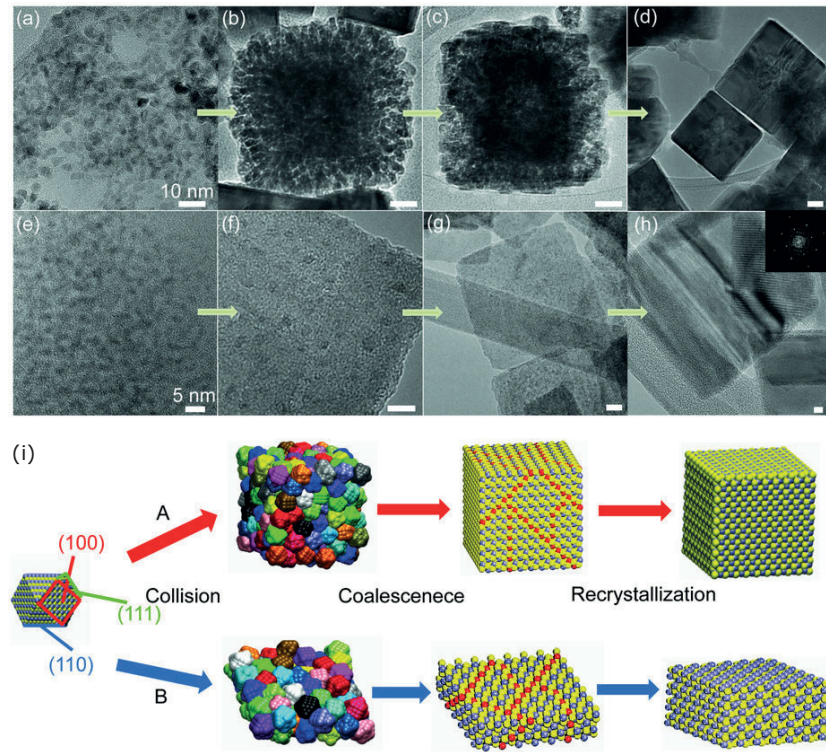


FIGURE 2.10: TEM-images of oriented attachment of nanocrystals (a-d) and nanosheets (e-h) and a schematic drawing of the same processes (i). Reprinted from [103] (CC-BY license)

In addition to growth mechanisms, several novel nucleation mechanisms has been observed or suggested. Gower *et al.* observed the existence of liquid-liquid phase separation in calcium carbonate systems.[106] As the experiments were done in the presence of poly-aspartate, the mechanism was termed polymer-induced liquid-precursor (PILP). PILP is described to behave more liquid like than amorphous particles which are considered more of a solid material. Later it has been shown that liquid-liquid phase separation can also occur without the presence of additives,

resulting in what is often called a dense liquid phase (DLP).[107] However, neither of these concepts can successfully describe the existence of pre-nucleation clusters (PNC).[108] In contrast to the classical theory, where a nucleus above a critical size will grow and form a crystal whereas a nucleus below this size will dissolve, PNCs consists of stable clusters of associated ions which do not lead to immediate growth. The existence of such clusters has been shown for calcium carbonate, initially by ion potential measurements and later by cryo-TEM.[109, 110]

A detailed description of these mechanisms is beyond the scope of this work, however, a short introduction has been given in to highlight the complexity of crystal formation in a biomimetic environment including charged polymers and inorganic additives. It is important to note that experimental evidence for many of these mechanisms are lacking, and the theories are often based on observations of crystals after the suggested pathways have been traversed.[102] It has been shown that crystal morphologies often associated with biological crystallization in the presence of additives may also form in additive-free systems explained by classical mechanisms.[111] Recently, the characterization techniques used to describe the existence of mesocrystal structure (a suggested form of crystal formed by particle attachment) have been criticized for not accounting for strain which may exist within the crystal structure.[112] Although the idea of crystal growth by particle attachment has been around for a long time, a major part of research activity has occurred during the last decade or so. As a result, the theories are so far more qualitative than quantitative in their descriptions of crystal growth. In our studies we have not come across any results which could not be explained by classical models. Therefore, the discussion regarding crystal growth and the effect of additives presented herein are done within the framework of classical crystallization theory.

2.4.3 The effect of additives

It has been shown that a range of organic and inorganic additives can affect crystal nucleation and growth.[113] In crystal growth, additives with specific binding preference for active sites can reduce the growth rate or even alter the growth mechanism for a crystal. In addition, preferred binding to crystal facets can alter the shape of the growing crystals by changing the relative growth rate of the facets. The effects of additives are especially interesting in the context of

biomineralization. The additives alter the nucleation properties of solutions and in many cases acts as a template direction mineral formation both in terms of polymorphs and macroscopic morphology. It has been shown that additives may stabilize metastable amorphous phases.[114] The stabilization of amorphous mineral phases is widespread in biominerals and have been shown for diatoms, sea urchins, mollusk larvae, crustaceans, chitons and recently zebrafish.[94, 115–117] Mahamid *et al.* has also demonstrated the existence of stabilized ACP-particles in mineral vesicles in mammalian bone formation.[118] If an amorphous phase formed early in the mineralization process is subjected to additives which prevent the dissolution, the lifetime of this unstable phase can be greatly increased. Other mechanisms such as poisoning of the crystal structure in crystal nuclei and inhibition of crystal growth have also been suggested.[119]

The effect of organic molecules on crystal formation is especially relevant for biomineralization and bone. Despite many years of research, the mineralization of bone is not yet fully understood. There is a vast amount of literature on the subject, but the exact mechanisms remain elusive. Most literature agree that during bone formation, a collagen matrix is created which is subsequently mineralized with nano-platelets of HA. However, how this mineral is situated is not universally accepted; although most literature suggest that the mineral exists within the collagen fibrils, some researchers have suggested that the majority of mineral is actually situated in the space between the fibrils.[30, 120–122] In addition, there is a debate about how the intrafibrillar mineral nucleates and grows within the fibrils. It has been suggested that the non-collagenous proteins contribute to the intrafibrillar mineralization of collagen. Price *et al.* proposed that this occurs by inhibiting nucleation outside the fibrils and due to a size-exclusion of the proteins, only ions are able to enter the collagen fibrils where crystals nucleate and grow.[123] Traub *et al.* has earlier seen a similar phenomenon, where HAp nucleates a short distance into the collagen fibril.[124] However, they noted that the nucleation occurred in a specific band region associated with the binding of two non-collagenous proteins and suggested that the nucleation was mediated by these proteins. This second pathway is extended in the PILP-theory where it is believed that the presence of non-collagenous proteins stabilize a liquid-like phase with a high content of ions.[125] The liquid behavior of the PILP allows for penetration into narrow spaces before crystallization, perhaps aided by specific interactions between the stabilizing polymers and the organic template (i.e. collagen fibril). In a different study, the infiltration and nucleation of oriented CaP within collagen

fibrils were observed regardless of the presence of a non-collagenous protein able to enter the fibril, suggesting that it is indeed collagen which directs the intrafibrillar nucleation and growth.[126] Although the exact mechanism for the nucleation and templating of HAp platelets within collagen fibrils is not yet known, it is evident from a range of experiments that organic additives play an important role to ensure that HAp nucleates within the fibrils.[127, 128]

Parallel to the work described in detail in this thesis, our group has also looked into the effect of alginate on the crystallization of CaP. Through carefully designed experiments the effects of small amounts of alginate on the growth and nucleation of CaP were investigated.[129] Specifically, the effect of alginate chains and short oligomers containing predominantly either M-residues or G-residues on the nucleation and growth of brushite was studied. In a seeded study, designed to investigate the influence on crystal growth, the presence of alginate in any form reduced the growth rate, probably through a blockage of active growth sites. In the case of M-blocks, a reduced growth rate was observed, however, there was no change in the apparent growth order, indicating that the blocking of growth sites was non-specific. In the case of G-blocks both a reduced growth rate and an increased apparent growth order was observed, which suggests that G-blocks binds specifically to growth sites on the crystal surface leading to a surface nucleation mechanism for further growth. The influence on nucleation was also investigated and it was shown that alginate, especially G-blocks, had an inhibitory effect on the nucleation of brushite. Similar studies regarding the inhibitory effect of alginate have also been performed on HAp precipitated directly and via the transformation from brushite.[130]

2.5 Characterization of biomaterials

Thorough characterization of a biomaterial is important in order to understand its interactions with the complex *in vivo* environment. For a material intended to interface with bone, properties such as bulk chemistry, surface chemistry, porosity, stability and mechanical properties are of high interest. In addition, crystal phase and morphology for crystalline materials and the relative amount of constituents in composite materials are important. In this work, great effort was put into characterizing the process of CaP-crystallization within an alginate network. In this respect, diffusion of ions, evolution of pH and crystal phase, morphology and

distribution were studied. The following section provides an overview and short introduction to some of the central techniques used in this work and offers some details regarding analysis of the resulting data.

2.5.1 Microscopy

My experience with microscopy can be summarized in two clichés; seeing is believing and looks can be deceiving. A microscopy image can give a lot of information about a sample regarding morphology and size. The demand for increased resolution and faster recording speed is pushing the development of optical microscopy as well as electron and scanning probe microscopy to ever new heights. However, one has to keep in mind that the resulting image is a combination of sample-probe interactions (the probe can be photons, electrons, physical probes etc), sample preparation, hardware contributions, image processing and not least the skill of the microscopist. Careful consideration of some or all of these contributions is often needed to interpret the resulting image. In optics, one usually describes the image as a convolution of an object function and a point spread function (PSF). The PSF is a result of diffraction events in the microscope and can be understood by considering light as wavelets instead of rays. The PSF can also include any aberrations from the microscope itself. If the PSF of a microscope is known, the image quality can be improved by deconvolution, although not beyond the diffraction limit which is dependent on the wavelength of the used light source. Recent developments in super-resolution microscopy has been able to surpass this diffraction limit by clever use of photoswitchable fluorescent markers in combination with laser manipulation (stimulated emission depletion-microscopy) or the activation of a subset of the fluorescent markers (stochastic optical reconstruction microscopy). These optical super-resolution techniques are not considered herein, and readers are referred to the literature within this field, for example this review by Huang *et al.* [131]. The resolution in an electron microscope is not limited by the wave nature of the electrons due to a much smaller wavelength, however, an analogous PSF can be found by considering the spatial distribution of the beam current density.

In all microscopy, and especially for electron microscopy, it is important to keep in mind the effects of sample preparation methods. Most electron microscopy is performed in vacuum, which means the sample has to be dehydrated prior to

imaging. If a hydrogel is to be imaged in an electron microscope, the water must be removed. If the sample is air-dried the structure will collapse. The main culprit responsible for this is the surface tension of water. The same effect that will make a water column rise in a capillary tube to form a meniscus will pull on the gel structure as the amount of water decreases. This occurs due the strong cohesive force of the hydrogen bonds in water, which are much stronger than interactions between water and air molecules at the surface. These forces lead to a minimization of the surface area. For a hydrogel which has stronger bonding to water than air, this surface area minimization leads to a collapse of the structure. To avoid this, water must be removed while reducing the destructive effects of surface tension. There are several methods to do this, including freeze-drying, critical point drying, chemical dehydration and embedding techniques, however, all of these techniques will induce changes in a previously hydrated sample. There is much effort in minimizing this effect, however one must remember that the imaged sample may not be representative of the native state.

In a scanning electron microscope (SEM) an electron beam is focused into a sharp point and scanned across the surface of a sample. Several interactions between the sample and the electrons in the beam are possible, see Figure 2.11. There is a certain interaction volume associated with the different interactions. This describes a volume in the sample where an interaction can occur and the resulting signal (electron or x-ray) can still escape from the sample surface in order to be detected. The size of the interaction volume increases with increasing acceleration voltage, and is sample dependent. The most common contrast mechanism relies on counting the amount of secondary electrons (SE) reaching a detector from each point scanned by the incident electron beam. Curvatures on the surface will affect the distance a generated SE has to travel to escape the sample surface and areas with positive curvature (i.e. protruding from the surface) appear brighter than areas with negative curvature.[132]

Another useful sample-beam interaction in the SEM is the backscattered electron (BSE), a quasi-elastic scattering of the electrons in the incoming beam. Incident high energy electrons scattered to large angles can escape from the sample surface and can be collected by a detector, often an annular detector some distance above the sample. The probability of backscattering increases with increasing atomic number, so BSE can resolve local mass density variations and is often called Z-contrast, where Z refers to the atomic number. The interaction volume in which

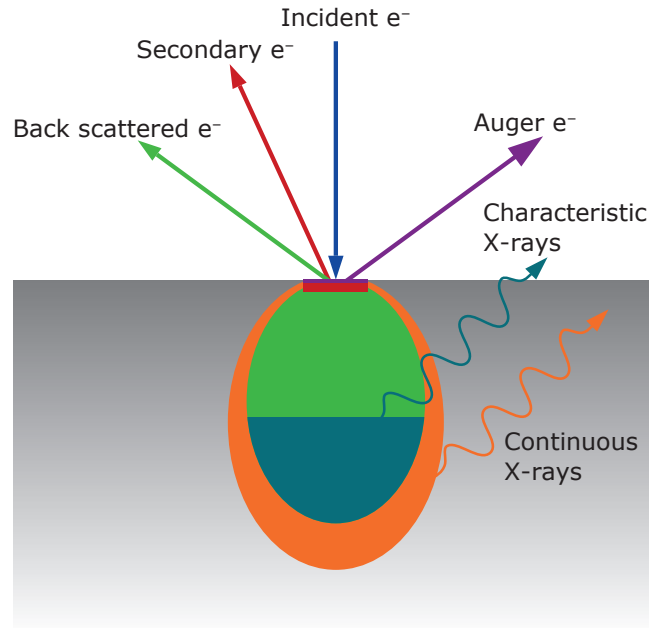


FIGURE 2.11: A schematic drawing of typical electron beam-sample interactions and their respective interaction volume. The differences in interaction volumes are not to scale, and only indicative of the spatial resolution of the different interactions. It can be seen that the spatial resolution decreases as the signal originates from SE, BSE and characteristic X-rays, respectively.

SE are generated is much smaller than the volume in which BSE are generated, resulting in a difference in the spatial resolution which can be obtained. The Stevens group at Imperial College London has developed a method which combines SE and BSE images from the same area in order to obtain the best of both worlds; high spatial resolution combined with density information.[133] Termed density-dependent contrast SEM (DDC-SEM), the technique combines colored images from SE and BSE channels and blends the images to provide a result which highlights areas with high density whilst providing the high resolution surface topography information. See Figure 2.12 for an example. The resulting image provides a false-colored SEM-image where the colors provide physical information, in contrast to conventional false-color SEM where color is provided simply to guide the eye.

Powerful as they may be, high magnification techniques such as electron microscopy do just that; they provide a highly magnified, detailed view of a small

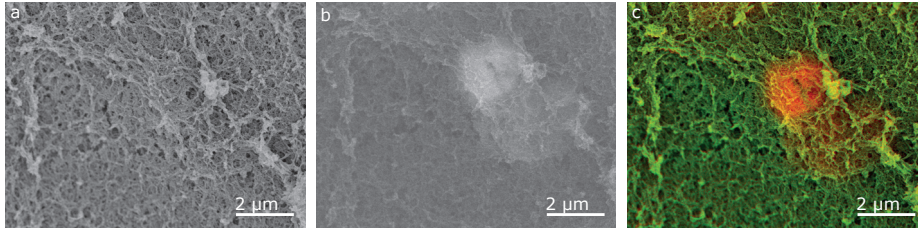


FIGURE 2.12: SEM-images illustrating DDC-SEM (unpublished data). **a)** SE-image of an alginate hydrogel surface. **b)** BSE-image revealing a mineral-particle below the surface. **c)** An aligned composite image of **a)** and **b)**. Red color indicates an increase in density.

part of the sample without providing any statistics on a bulk scale. The high resolving power of expensive techniques such as TEM may not be required to identify a certain parameter. It is often beneficial to apply lower magnification techniques early in a sample analysis work flow to obtain some initial overview and identify regions of interest. For example, the transient region of submicron ACP-particles discussed in Paper III was first observed with regular light microscopy. This may be one of the reasons for the surge of publications involving correlative techniques. Correlative microscopy, whether the combination of light microscopy and electron microscopy (CLEM) or other techniques is ever increasing in popularity.[134] CLEM combines the specific markers available to fluorescent microscopy with the resolving power of electron microscopes to obtain ultrastructure information about specific tissue, cell types or biological processes.[135]

Quantitative measurements based on fluorescent microscopy require extra care in the experimental design as compared to qualitative measurements. Changes in thickness of a region of interest and fluctuations in dye concentrations or laser intensity may cause artifacts in the measurements. Choice of detector types and settings may also influence the results by introducing noise in the measurements. Performing ratiometric measurements is a strategy to reduce such artifacts and relies on the combination of one dye which is sensitive to the investigated property and one dye which is not. By calculating the ratio between the measured signal for each of these dyes, the error is reduced by for example eliminating changes in the absolute intensity due to laser fluctuations.

2.5.2 Spectroscopy

Spectroscopy, in general, provides information about a sample via its interactions with electromagnetic radiation. The energy of the radiation varies depending on the application and will also affect the type of interaction with the sample. Typical interactions are absorption, emission and inelastic scattering and depending on the energy of the radiation these can induce electronic transitions, molecular vibrations, structural vibrations or other interactions which can be detected by measuring the intensity as a function of frequency.

In an electron microscope interactions between the electron beam and atoms in the sample can generate characteristic X-rays. The incident high-energy electron generates a secondary electron from a certain electron shell of an atom in the sample. An electron from a shell further away from the core migrates to fill the generated hole and the excess energy is released in the form of an X-ray. The energy of these X-rays is shell and element specific and this forms the basis of a technique called energy dispersive X-ray spectroscopy (EDS). EDS provides information about the elemental composition of a sample with (relatively) high resolution. In the SEM, the interaction volume where characteristic X-rays are generated is even larger than for BSE and the spatial resolution is often in the μm -range rather than nm-range. This interaction volume is highly sample-dependent and knowledge about the sample is often needed to correctly interpret the results. X-ray generating events can also occur due to electrons scattered to large angles and depending on the sample type, the decoupling of beam position and signal generation can lead to contradicting results if these effects are not accounted for. See Figure 2.13 for an example of this. In the presented case, CaP-nanoparticles were dispersed on a copper TEM-grid covered by a carbon film. When EDS was performed on particles located on the film, the results showed the presence of copper in the particles. When particles located on top of the copper-grid were analyzed, the results showed the absence of copper-signal from the region where the particles were situated. In reality, high energy electrons scattered to large angles from the nanoparticles generated characteristic X-rays from the copper grid of the sample holder which the software localized to the beam position.

Typically, spectroscopy concerns the interactions between electromagnetic radiation and a sample. The most common types of spectroscopy are UV-vis spectroscopy and fluorescence spectroscopy. These are complementary techniques

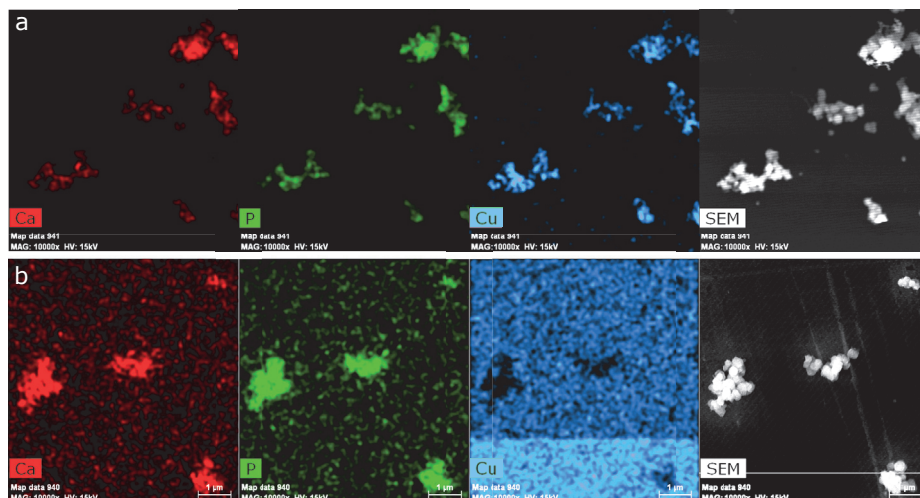


FIGURE 2.13: EDS-mapping with calcium, phosphorous and copper signal of CaP-particles on a carbon-coated copper-grid (unpublished data). **a)** Particles located on the copper grid. In **a)** the copper-signal is co-localized with the particles while in **b)** the copper-signal is reduced where particles are present.

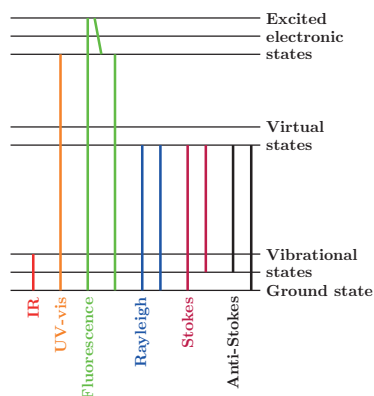


FIGURE 2.14: A Jablonski diagram showing the electronic transitions related to different spectroscopy techniques.

which probe electronic transitions in the sample. UV-vis spectroscopy measures the absorption, while fluorescence spectroscopy is concerned with the emission from the sample. Examples of transitions of different spectroscopy techniques are given in a simple Jablonski diagram in Figure 2.14.

Vibrational spectroscopy provides chemical information about the sample. Typical techniques are infrared (IR) spectroscopy and Raman spectroscopy. The first utilizes the absorption of infrared radiation which matches the vibrational frequency

of chemical bonds in the sample. The latter is a more complex interaction where a fraction of the incoming photons are scattered inelastically and the energy difference corresponds to a molecular vibration in the sample. These two techniques are complimentary, where an IR-induced vibration is dependent on a change in the molecules dipole, whereas a Raman-induced vibration is dependent on the polarizability of the molecule. This means that for a simple molecule, an IR-active vibration is Raman-inactive and vice versa, see Figure 2.15. The induced dipole moment of a molecule as a function of polarizability is given by:[136]

$$P = \alpha_0 E_0 \cos(2\pi\nu t) + \left(\frac{\delta\alpha}{\delta q} \right)_0 E_0 \cos(2\pi\nu t) q_0 \cos(2\pi\nu_{vib} t) \quad (2.5)$$

Here, α_0 is the polarizability at the molecule's equilibrium position, $E_0 \cos(2\pi\nu t)$ describes the electric field of the incident light, $q_0 \cos(2\pi\nu_{vib} t)$ describes the molecule's vibration about an equilibrium position with q_0 as its maximum displacement and the derivative describes the change in polarizability for a small amplitude of molecular vibration evaluated at the equilibrium position. Equation 2.5 can be rewritten to:

$$P = \alpha_0 E_0 \cos(2\pi\nu t) + \left(\frac{\delta\alpha}{\delta q} \right)_0 \frac{q_0 E_0}{2} [\cos(2\pi(\nu - \nu_{vib})t) + \cos(2\pi(\nu + \nu_{vib})t)] \quad (2.6)$$

where the first part describes regular Rayleigh scattering, the first term in the square brackets describes the loss in energy of the scattered light (Stokes scattering) while the last term describes a gain in energy of the scattered light (anti-Stokes scattering). It can be seen that molecules with no vibration-induced change in polarizability (i.e. $\delta\alpha/\delta q = 0$) are not Raman active.

One of the main advantages of Raman spectroscopy is the minimal amount of sample preparation required to perform measurements. In contrast to IR-spectroscopy, the water-vibrations in the Raman-spectra are rather weak and so does not mask other signals. This means that Raman-spectroscopy can be performed directly on hydrated samples which is a major benefit regarding biological samples. This was exploited by Crane *et al.* who showed evidence of OCP as a precursor phase in forming bone in mice.[138] The importance of studying biological materials in their native hydrated state has recently been highlighted by Duer.[139] Indeed in the work performed for this thesis, early XRD-studies of dehydrated samples rarely showed any sign of OCP, whereas *in situ* studies using Raman spectroscopy of similar samples provided convincing evidence for its presence.

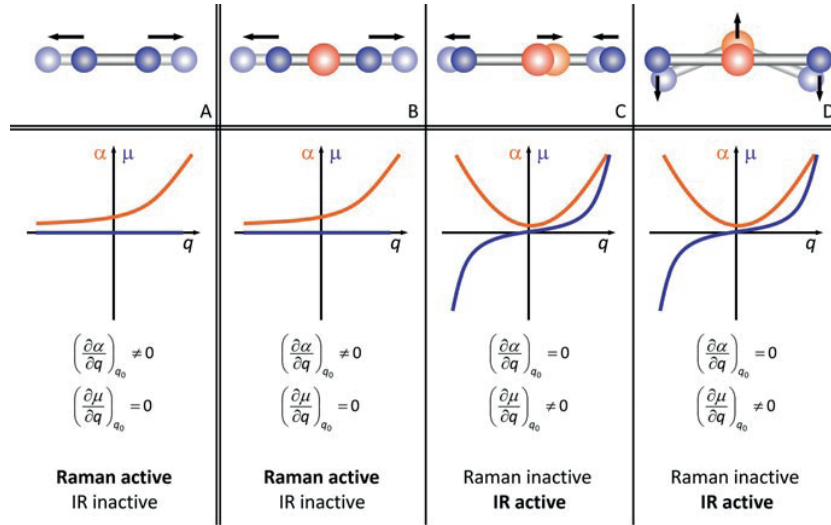


FIGURE 2.15: An overview of simple molecular vibrations and their Raman and IR activity. Reprinted from [137], copyright 2010 with permission of Springer.

Despite all its advantages, one has to keep in mind that the Raman signal is inherently weak and can easily be masked by auto-fluorescence from the sample. Strategies to avoid this includes the use of a NIR-laser to reduce fluorescence generation, bleaching by irradiation over time and enhancing the anti-Stokes signal which is not affected by background fluorescence.[140–142]

2.5.3 Diffraction

One important technique in this work has been X-ray diffraction (XRD), a technique that measures the intensity of X-rays scattered from the sample at different angles. The repeating structure of a crystal can be described as different planes of atoms with a given distance between them. These planes are usually described by a vector normal to the plane given in Miller indices. Parallel planes with a given orientation and spacing are described by the normal vector $[hkl]$, where h , k and l are integers. As X-rays are scattered from a set of planes, constructive interference occurs at selected degrees depending on the distance between the planes and the wavelength of the incident X-ray. This is shown schematically in Figure 2.16 and mathematically by the elegant Bragg equation:

$$n\lambda = 2d_{hkl} \sin \theta \quad (2.7)$$

where n is an integer, λ is the X-ray wavelength, d is the interplanar distance and θ is the diffraction angle. For a given X-ray wavelength, an integer n , corresponding to the order of reflection, and a spacing d_{hkl} , corresponding to the distance between sets of atomic planes, the resulting θ will give the angle at which reflections from these planes are in phase. By scanning a range of angles and measuring the scattered intensity, a fingerprint spectra for a given crystal structure can be obtained.

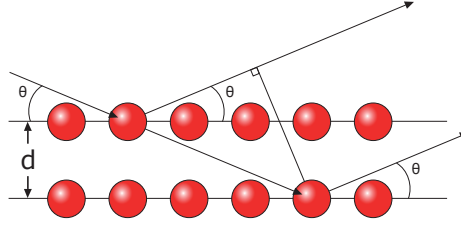


FIGURE 2.16: A schematic drawing showing the scattering from two planes in a crystal.

This simple geometrical approach gives a qualitatively description of the diffraction process, but it does account for the physical process behind the diffraction, which is interference of the scattered waves. Thus, it does not provide any information about the intensity of the scattering at the different angles. The following description is adapted from references [132, 143, 144]. The direction of a propagating wave, such as an X-ray, can be specified by a vector \mathbf{k} so that $|\mathbf{k}| = 2\pi/\lambda$, where λ is the wavelength of the x-ray. The space defined by sets of such vectors are called reciprocal space and have inverse dimensions compared to real space, i.e. a short distance in real space is a long distance in reciprocal space.

The scattering amplitude describes the amplitude of a spherical wave from a scattering center. For a scattering center, such as an atom or a group of atoms, the scattering amplitude in a given direction described by the vector \mathbf{G} and the time-average electron density function, $\rho(\mathbf{r})$, is given by the Fourier integral:

$$F(\mathbf{G}) = \int \rho(\mathbf{r}) e^{2\pi i(\mathbf{r}\mathbf{G})} dv_{\mathbf{r}} \quad (2.8)$$

where $dv_{\mathbf{r}}$ represents an element of the scattering volume. The vector \mathbf{G} describes the path difference between the original plane wave and the scattered plane wave. Equation 2.8 can be derived by first considering the case of a wave scattered by two discrete scattering centers and extending this case to include n scattering centers,

then introduce a continuous distribution instead of discrete scattering points, see Vainshtein for details.[143] In other words, the scattering amplitude in reciprocal space is given as a Fourier transform of the electron density function in real space.

The structure of an ideal crystal can be described as an infinite number of repeated unit cell with cell dimensions given by a , b and c and angles α , β and γ . This can also be described by the real space vectors \mathbf{a} , \mathbf{b} and \mathbf{c} . For such a periodic structure the Fourier transform, in contrast to the continuous set of values from Equation 2.8, leads to a set of discrete values and the orientation of scattering centers (i.e. atoms) inside this unit cell determines the resulting diffraction pattern. For a periodic function determined by the crystal structure the Fourier transform in Equation 2.8 becomes a set of Fourier coefficients

$$F_{hkl} = \frac{1}{V} \int_V \rho(\mathbf{r}) e^{2\pi i(\mathbf{r} \cdot \mathbf{H})} dV_{\mathbf{r}} \quad (2.9)$$

where V is the unit cell volume and \mathbf{H} is a vector in reciprocal space defined as:

$$\mathbf{H} = h\mathbf{a}^* + k\mathbf{b}^* + l\mathbf{c}^* \quad (2.10)$$

with h , k and l as integers and \mathbf{a}^* , \mathbf{b}^* and \mathbf{c}^* defining the unit cell of the crystal in reciprocal space. The real space lattice and the reciprocal space lattice are related by:

$$\mathbf{a}^* = \frac{\mathbf{b} \times \mathbf{c}}{V}; \quad \mathbf{b}^* = \frac{\mathbf{a} \times \mathbf{c}}{V}; \quad \mathbf{c}^* = \frac{\mathbf{a} \times \mathbf{b}}{V}; \quad V = \mathbf{a} \cdot \mathbf{b} \times \mathbf{c} \quad (2.11)$$

Due to the discretization of the periodic function, F_{hkl} is non-zero only if h , k and l are integers. Equation 2.9 is analogous to

$$F(hkl) = \sum_j f_j e^{2\pi i(\mathbf{r}_j \cdot \mathbf{H})} = \sum_j f_j e^{2\pi i(hx_j + ky_j + lz_j)} \quad (2.12)$$

which is known as the structure amplitude where, f_j is the atomic scattering amplitude for a single atom in the unit cell located at \mathbf{r}_j and summed over the number of atoms within the unit cell given by j . It can be shown that

$$|\mathbf{H}_{hkl}| = 1/d_{hkl} \quad (2.13)$$

hence the structure amplitude provides the same information about reflection angles and plane distance as in the Bragg equation, however, it also provides the intensity at the different angles making it much more useful for structure determination.

The use of Fourier transforms in the description of crystals has a few implications. Firstly, Equation 2.8 implies that by measuring $F(\mathbf{G})$ we could deduce the entire electron density of our crystal and perfectly describe its structure. However, an XRD-experiment measures the intensity or $|F(\mathbf{G})|^2$ (the product of the scattering amplitude and its complex conjugate) thereby losing the phase-information needed to describe the structure. Hence, a starting model of the structure has to be refined in order to model the structure giving the intensity of a measured diffraction experiment. Secondly, the assumption of ideal crystals falls short in the real world. Any real crystal has a finite size and some imperfections. For a crystal with finite size, the electron density function falls to zero outside the sides of the crystals. This leads to a broadening of the diffraction spots as the Fourier transform again becomes a continuous function. The smaller the crystal size, the broader diffraction peaks become, a relation which is utilized in Rietveld refinement described below.

XRD is conventionally carried out using bulk powder samples and a large area illuminated by X-rays which provides information averaged across the whole sample without any spatial information. Analysis can be performed with focused spots, however, this requires more specialized equipment and in many cases synchrotron sources for the X-rays, although home lab set ups are becoming increasingly available.

XRD spectra do not only provide fingerprint identification of crystal structure. The peak shape, width and shifts contain more information about the sample. The scattered intensity in XRD is directly related to the crystal structure and careful examination of the spectrum can provide useful information. The peak width is related to the coherence length, a representation of the distance between imperfections in the crystal structure, often termed crystallite size. The coherence length can be calculated by applying the Scherrer equation:[145]

$$t = \frac{K\lambda}{\beta_{1/2} \cos \theta} \quad (2.14)$$

where t is the crystallite size, K is the Scherrer constant (usually close to 1), λ is the wavelength of the X-rays, $\beta_{1/2}$ is the full width at half maximum (FWHM) of the peak and θ is the angle of the peak. It can be seen that a reduction in crystallite size leads to a broadening of diffraction peaks. This can also be understood in terms of a change in the periodicity of the lattice structure and an approximation to a finite sized crystal rather than close to infinite, hence broadening the peaks of the Fourier transform. Lattice strain can induce changes in the unit cell dimensions and a reduction in the periodicity will also broaden the peaks, but due to a difference in the θ -dependence between these two mechanisms, the origin for peak broadening can be determined, for example using a Williamson-Hall plot.[146] Uniform lattice strain will on the other hand lead to a shift in peak position, not in peak broadening.

The Rietveld method is a full profile fitting method which accounts for the peak shapes by considering both instrument effects, lattice parameters and crystal structure to accurately fit peak shapes, positions and intensities. By fitting the resulting spectrum with this method, quantitative results of a sample with multiple phases can be obtained. Rietveld fitting seeks to minimize the the square sum of errors between the measured spectrum, y_i^0 , and a calculated fit y_i^c ,

$$\sum (y_i^0 - y_i^c)^2 \rightarrow \min \quad (2.15)$$

where y_i^c is given by

$$y_i^c = y_{bi}^c + S \sum_{k=1}^n m_k L_k |F_k|^2 G(\Delta 2\theta_{ik}) P_k \quad (2.16)$$

Here, y_{bi}^c is the calculated background, S is the scale factor and the sum describes the peak location, shape and intensity, for details see Wiles and Young.[147] For a sample containing several phases, the weight fraction can be calculated from the refined scale factors via

$$W_i = \frac{S_i \rho_i V_i^2}{\sum_j S_j \rho_j V_j^2} \quad (2.17)$$

where S is the scale factor, ρ is the density and V is the unit cell volume for i ; the phase in question and j ; all phases present.[148] For further details, the interested reader is pointed to relevant literature.[147, 149–151]

2.6 Model system for gelling and mineralization

Alginate hydrogels are often made in the form of beads or fibers. During this project, we saw the need for a simple, easy to use model system compatible with several characterization techniques in order to study gelling kinetics and the mineralization of such geometries. By placing a droplet of alginate between two glass slides, separated by a short distance, an effective semi-2D cross-section of such a bead could be studied. The use of glass slides made the cross section compatible with a range of optical techniques. Due to a difference in refractive index between gelled and ungelled alginate, the diffusion of calcium could be studied by phase contrast microscopy. For mineralized samples, the mineral phase and relative amount could be measured with Raman microspectroscopy. By recording multiple spectra from a single position during the mineralization process, insight into the maturation process could also be obtained. Due to the symmetry in the system, it is possible to extend the information of this simple 2D-model into 3D thereby providing a description of the processes within a spherical bead or a cylindrical fiber.

The counter-diffusion system during bead formation is schematically depicted in Figure 2.17. The simple case in Figure 2.17 a have been studied by Mikkelsen and Elgsæter who developed a reaction-diffusion model for the concentration profiles of alginate and calcium.[152] Initially, the system can be divided into two parts, an alginate solution and a calcium-solution. When these solutions are brought into contact with each other, calcium diffuses into the alginate-solution where it binds to alginate and becomes immobilized. Alginate molecules diffuse into the calcium-solution although the diffusion coefficient is much lower for these large molecules. In addition, when alginate chains forms cross-links with other chains, they too become immobilized. A set of coupled differential equations were suggested:

$$\frac{\partial c}{\partial t} = D_c \nabla^2 c - N_c \frac{\partial g}{\partial t} \quad (2.18)$$

$$\frac{\partial a}{\partial t} = \nabla [D_a \nabla a] - \frac{\partial g}{\partial t} \quad (2.19)$$

$$\frac{\partial g}{\partial t} = kca^2 + kacg \quad (2.20)$$

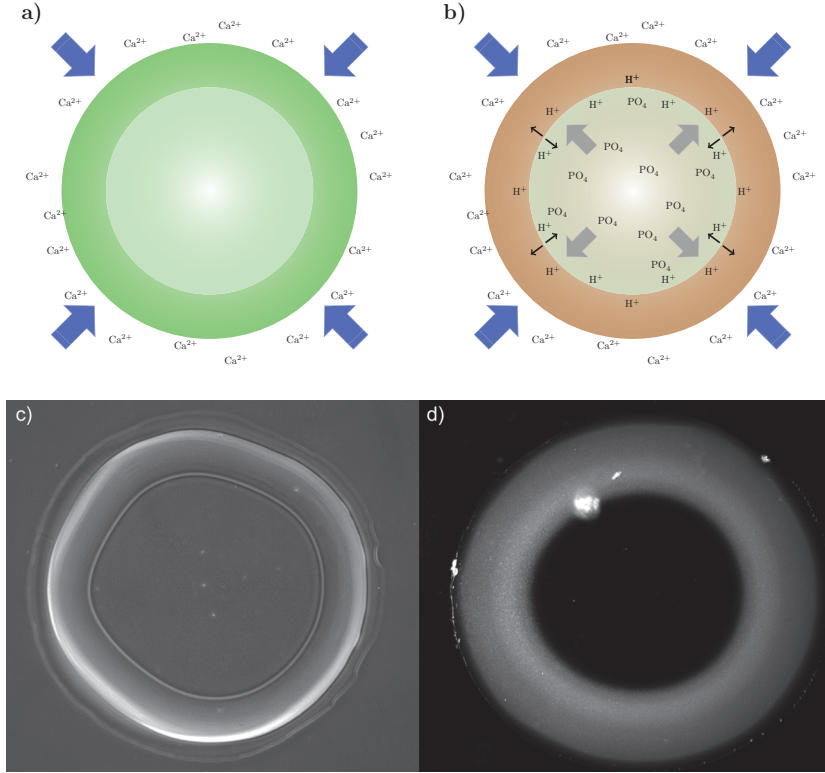


FIGURE 2.17: A representation of the counter-diffusion processes occurring during bead formation. The schematic in **a)** shows the gel formation while **b)** depicts the mineralization process. Blue arrows mark the main direction of Ca^{2+} diffusion, grey arrows show PO_4^- diffusion and black arrows denote H^+ diffusion. The image in **c)** is a phase-contrast optical image of the gelling process of a pure alginate sample. The gel front is clearly visible. The image in **d)** is a dark-field image showing the mineralization of a similar sample. The bright spot is a piece of dust.

where c is the concentration of calcium ions, a is the concentration of free alginate monomers in terms of moles of carboxyl groups and g is the concentration of alginate monomers bound to a calcium ion (gelled alginate). N_c is a stoichiometric coefficient describing the amount of calcium ions bound per carboxyl group. Finally, D_c and D_a are the diffusion coefficients for calcium ions and free alginate chains respectively. It is important to note that this model assumes that the binding rate of a free alginate chain to another free alginate chain or to an n -mer of chains is much larger than the binding rate of an n -mer to an m -mer where n and m are both equal to or larger than 2. Again, "mers" refer to whole alginate chains, not G- and M-residues. As the initial concentrations of alginate and calcium are

determined by experimental conditions, the model has in essence four adjustable parameters, N_c , k , D_c and D_a . The diffusion of calcium and alginate can be found in the literature and the two remaining parameters can be found by fitting the model to experimental observations. Interested readers are directed to the work by Mikkelsen and Elgsæter for further details.[152]

For the case in Figure 2.17 b, the system becomes much more complicated. To be able to model the mineralization, the counter-diffusing phosphate concentration must also be calculated. This is dependent on the induction time for nucleation, nucleation rate as well as stoichiometry and solubility of the precipitating phase(s). When we consider that some of these parameters are pH-dependent and the precipitation of CaP itself will change the pH, one can appreciate how daunting of a task this is. For a system with a large number of degrees of freedom, high quality experimental data is needed to provide model verification. No attempt to model the complicated system was performed in this work, however, we believe the characterization system presented here is a valuable tool to collect experimental data which can be included in such a model.

Chapter 3

Summary and discussion of papers

3.1 Brief summary of papers

Paper I

The effect of pH on the precipitation of CaP within an alginate hydrogel matrix was investigated with the fabrication of a brushite-alginate composite in mind. Phosphate-containing alginate solution was added drop-wise into a gelling solution containing Ca^{2+} resulting in a counter-diffusion precipitation system. By independently varying the pH in the two solutions, the effect of pH on the resulting mineral phase and amount was studied. In most cases this resulted in a mixture of several CaP-phases. By employing brushite crystal seeds dispersed in the alginate solution, composites with a relatively high mineral content (up to 85 % dry mass corresponding to 10 % wet mass) of phase pure brushite could be produced. The mineral content in the composites was determined by a combination of powder-XRD analysis and thermogravimetric analysis (TGA). Briefly TGA-curves for control samples of pure alginate, pure brushite and pure HAp were obtained and a linear combination of these was fitted to match the end-point of experimental samples where the relative content of brushite and HAp was calculated based on XRD-analysis. The bioactivity, the ability to form HA upon soaking in simulated body fluid (SBF), was investigated for the composites made with different amounts of crystal seeds. It was found that the mineral in composites made with a low amount of seed crystals transformed more rapidly into HA,

an indication that the newly formed mineral was less stable than the preformed seeds. The same trend was observed by FTIR-analysis. This was further corroborated by SBF-soaking of control samples which contained brushite seeds, but not subjected to *in situ* mineralization. These showed no conversion of the preformed seeds. In addition, soaking of pure alginate beads showed no formation of HAp demonstrating the increased bioactivity of the composite material.

In previous work from our group, cells were successfully encapsulated *in situ* in hydrogel composites prepared at mild conditions.[7] In the presented work, cells were encapsulated in hydrogel composites prepared under conditions of high ionic strength and at pH 5. The viability of murine pre-osteoblast cells (MC3T3-E1) was assessed by a combination of a LIVE/DEAD assay and an Alamar-Blue assay. The results showed no significant difference between mineralized samples and control samples with cells encapsulated in pure alginate under lower ionic strength and physiological pH.

In summary, the paper presents a well-characterized composite material with the potential to supply both ions and cells relevant for bone-formation as demonstrated by the HAp-formation and cell-viability tests.

Paper II

In order to further investigate the complex environment of the counter-diffusion system, presented in the previous paper, a semi-2D model system was developed. By placing a droplet of alginate solution between two microscopy slides separated by a spacer, a cross-section of the reaction within a bead or a fiber could be studied with a range of characterization techniques. Phase contrast imaging was employed to trace the gel formation as calcium diffused into the alginate solution and this data was fitted to a reaction-diffusion model describing the gel formation. Automated scripts were developed to measure the progression of the gelling front from video data, which is a valuable tool to analyze experiments of this nature. Although a model of alginate gelation has been previously developed, this work provided high resolution spatial and temporal experimental data to validate the model and extended the predictability of the model by including a range of calcium concentrations. Excellent fits between the model and experimental observations

were obtained, providing a tool to predict gelation time for different gelling conditions (changes in calcium concentration) and geometries (cylinders and spheres of different sizes). The model predicts a moving depletion zone and a slightly increased alginate concentration in the outer boundary of the gel. Both these phenomena were observed experimentally using a fluorescently labeled alginate and imaged with a confocal laser scanning microscope (CLSM).

In addition, it was demonstrated that CLSM in combination with a pH-sensitive fluorescent dye could be used to monitor pH gradients within the hydrogel. A protocol for imaging, calibration and image-analysis was developed and presented. Finally, confocal Raman microspectroscopy (CRM) was used to determine the crystallographic phase of CaP-mineral precipitated *in situ* within the alginate hydrogel matrix. CRM requires very little sample preparation allowing the experimental set up presented in the paper to be analyzed with CRM in the hydrated state during gelling and mineralization.

In summary, the paper introduces a simple experimental setup compatible with several advanced characterization techniques. This setup provided the ability to use experimental observations of gelling kinetics to refine a reaction-diffusion model in addition to spatiotemporally monitor changes in pH and mineral phase during *in situ* mineralization.

Paper III

Using the same experimental set up as described in Paper II, the *in situ* mineralization of the model gel system was investigated in detail. Phase contrast microscopy was used to measure the gel front velocity for samples with different phosphate concentrations and in the presence of brushite seed crystals. As expected, an increase in phosphate concentration led to a decrease in the gel front velocity as calcium ions were consumed in mineral precipitation. This mineralization was studied with CRM, either by recording a spectrum from a certain position every 30 seconds, or by scanning the beam across the sample to provide spatial information about the mineral distribution. By careful analysis of the phosphate peak positions and peak shapes, the presence of both ACP and OCP was found in early stages of mineralization. ACP was observed during the first 120 seconds of mineral formation, matching observations done both with optical microscopy and

electron microscopy. OCP was found to be the main phase present after 1 hour within the alginate matrix. Over time OCP transformed into HAp and the phase change was also correlated with a change in crystal morphology.

The same measurements were performed on samples containing brushite seed crystals. The presence of ACP was observed both by CRM and electron microscopy for these samples. The seeds directed the mineral formation and brushite was formed within the alginate matrix. Upon storage this transformed into HAp. No OCP was observed for this sample type. In addition SBF-soaking of seeded samples, similar to the experiments performed in Paper I was studied with CRM and SEM. It was found that the *in situ* mineralized samples promoted HAp growth upon SBF-soaking, while the control samples which only contained seed crystals did not. HAp-formation was observed as a dense band, spanning 100-200 μm from the hydrogel edge towards the center of the samples. Further into the network, HAp was formed in the close proximity of a previously located brushite crystal. These observations suggested that the dissolution of brushite from *in situ* mineralized samples provided the necessary supersaturation for HAp formation within the hydrogel network.

This paper provides detailed observations about the initial mineralization of alginate hydrogels and the maturation the mineral phase undergoes upon storage. It shows that under the high supersaturation conditions used in the experiments, ACP was formed as the initial mineral phase regardless of the presence of seed crystals. The seeds affected the further crystallization process and upon dissolution of ACP, brushite was formed in the presence of brushite seed crystals whereas OCP and HAp was formed in the absence of seeds. It was argued that the peak shape of the main phosphate peak in the Raman spectrum for CaP can be used to distinguish between OCP and HAp, rather than a unique, but low-intensity HPO_4 -peak. The paper provides new insight on the formation of CaP-alginate composite materials and provides a non-destructive characterization platform which we believe can be applied to a range of mineral-hydrogel composites.

3.2 Discussion

At the moment tissue engineers are not capable of replicating true biological materials. However, the increased clinical demand for transplants (whether bone, other

tissues or whole organs) and the large research activity within the field points towards a future where more complex biomaterials will be a reality. To determine just how complex the synthetic replacements have to be, the understanding of fundamental properties must be improved. This includes the development of both *in vivo* characterization techniques and improved model systems where it may be easier to isolate variables and study their effect.

The work in this thesis has been focused on two main parts, namely the development of a specific composite material based on alginate and CaP and the more general characterization scheme of such a composite material, which is applicable to a wider range of biomaterials. A major focus has been on developing a correlative characterization scheme using complimentary techniques, both microscopy and spectroscopy, to describe dynamic events. Paper I concerns the fabrication of a composite material with emphasis on controlling the CaP-phase and amount in a simple, yet cell-friendly process. The effects of initial pH and buffer concentrations were investigated and a thorough characterization of mineral phase and content of the resulting composite was performed. This work spurred several interesting questions, which may be summarized in two main questions: Why is the precipitation of brushite within the alginate solution so different to the precipitation from regular solutions? What are the dynamics in the process? To answer these questions two parallel studies were performed; one concerned with elucidating the fundamental interactions between alginate and CaP and the other investigating the behavior of the composite in conditions similar to the conditions used in the fabrication process.

The result of these studies has provided insight into the effect of alginate on the growth of brushite crystals. The fundamental studies were performed in an experimental setup which provided careful control over supersaturation conditions and pH.[129, 130] It was shown that alginate has an inhibitory effect on both the nucleation and growth of brushite and this effect was more pronounced for G-blocks. These observations have improved our understanding of why the crystallization of brushite within the alginate hydrogel is so different from the crystallization in solution. The investigation of the composite in conditions more relevant for its application is described in paper II and III. The use of the 2D model system provided a better understanding of the processes which occur in individual beads or fibers, rather than the bulk, end-point analyses performed in paper I. This setup allowed the observations of mineral formation and evolution, as well as pH

changes, with spatiotemporal resolution. It was seen that in the high supersaturation conditions used in this work, nucleation of amorphous CaP occurred even in seeded conditions. The results from the fundamental investigations were used to interpret the mechanisms of the mineralization process. The hydrogel itself affects the ion transport in the system, and is more dependent on diffusion rather than in a stirred solution. In combination with the inhibition of crystal nucleation, the crystallization process of CaP in the alginate hydrogel is shifted towards the more stable OCP and HAp rather than passing through the more labile brushite phase as would be expected from the Ostwald rule of stages. The understanding gained from studying the fundamental and dynamic processes of gelling and mineral formation within the alginate hydrogel may aid in the rational design of biomaterials based on alginate and CaP. Parameters such as precursor concentrations, gelling time and feature dimensions can be altered in order to optimize mineral content, mechanical properties and cell survival.

The experience gained from paper I also resulted in a comment on a paper describing the fabrication of a similar composite material by another group.[153] To be able to fabricate an alginate-CaP composite with repeatable composition in terms of phase-purity, mineral amount and gel stability one needs to consider the precursor ratios and the dynamics of the precipitation reactions, not only the initial conditions of the experiment.

Although the characterization in this study has been performed in conditions related to the specific alginate-CaP composite, the methods are applicable to any optically transparent hydrogel system. We have performed some preliminary experiments on the mineralization of collagen gels under the same conditions as for the alginate hydrogel in the 2D system and recorded Raman spectra from the resulting samples. This approach resulted in heavily mineralized collagen fibrils with similar Raman-signatures as described for the alginate gels. It is also interesting to note that the mineral evolution observed in both the alginate and collagen gels, fabricated in conditions far from an *in vivo* environment, is remarkably similar to observations from the developing bone in an *in vivo* study on zebrafish.[154] Similar changes in the ν_1 phosphate peak observed by Raman spectroscopy were seen in both cases where a dual peak of an OCP-like phase were seen initially which over time shifted to a higher wavenumber single peak, indicative of HAp. This suggests that the characterization system described herein may be a useful tool in order to investigate biomimetic mineralization under more relevant conditions

than solution-based batch experiments. The flexibility of choosing different types of hydrogel, introduce selected additives and even include cells provides a powerful model system which hopefully can aid in the understanding of the mineralization of organic matrices.

Readers familiar with the field of biomaterials may notice an absence of cells in most of this work. The reasoning for this was to gain a detailed understanding of the composite material's behavior, prior to introducing yet another variable. By doing so, we are better equipped to interpret the results when the material is used in combination with one or several cell types. However, both the composite material and characterization scheme has been developed with the presence of living cells in mind and the optical characterization techniques (CRM, pH measurements, phase contrast imaging) are all compatible with *in situ* cell studies.

Chapter 4

Conclusions and outlook

This thesis demonstrates the fabrication and characterization of an organic-inorganic composite material based on alginate and CaP. This composite material provides a flexible platform where simple geometries such as beads, fibers and films can be made with varying CaP content and phase. Mineralization in a cell-friendly one-step process has previously been shown for HAp, and this work has shown a strategy to achieve cell-friendly mineralization with the more soluble brushite. I propose two main applications of this material. In first instance this composite can be used as a model system to study the crystallization of CaP within a hydrogel. I have demonstrated that the gelling and crystallization dynamics could be studied *in situ* in a simple semi 2D flow cell geometry. This setup could be monitored using optical techniques such as CRM and CLSM which provides information about chemical composition and pH with spatiotemporal resolution. I believe this setup to also be useful for studying mineralization processes in more biomimetic hydrogel systems and could, for example, be used to study the influence of non-collagenous protein mimics on CaP formation. A natural progression of the work presented herein would be to include relevant cell types in this model and study the influence on the mineralization within the hydrogel. As a second application, by taking advantage of the well-known cell encapsulation capabilities of alginate, I envisage a system where different cell types can be encapsulated within the hydrogel or seeded on the surface to create 3D co-cultures of for example osteoblasts, osteoclasts and osteocytes. Combined with the possibilities of making beads, fibers and films this provides a highly flexible system where larger constructs with tailored cell-content and anisotropic properties can be fabricated.

What lies ahead? Prediction is a dangerous game. Just ask Robert Metcalfe, co-inventor of Ethernet, who in 1995 predicted that the Internet would suffer a catastrophic collapse by 1996. I will nevertheless take my chances and try to speculate where the field of tissue engineering is headed. A reoccurring theme in this thesis has been the complexity of biological materials. This complexity does not only exist in the hierarchical structure of tissue, but is also present in the blood supply and cell signaling required to maintain the tissue. I am doubtful if we will ever be able to faithfully replicate a functional organ or a complex tissue such as bone on the lab bench, and I believe the development of resorbable biomaterials is the way to go. The solution is to provide a scaffold with enough functionality to fill the void (structural or functional) temporarily and promote or even improve the innate self-healing capabilities of the body. Such scaffolds will probably be based on combinations of ECM-like hydrogels with signaling molecules or relevant cells (i.e. bone cells and endothelial cells for vascularization in bone scaffolds) with mechanically strong materials such as ceramics or structural, but degradable polymers. The combination of semi-individualized design with 3D-printing will be widespread, but if we are able to control simple self-assembly strategies, they are probably easier to scale up. To reach this point, we need a better understanding of the fundamental processes in natural tissue which can only be achieved by further research and the development of better model systems that can be easily and independently reproduced. Hopefully the work in this thesis takes us a small step in the right direction.

Bibliography

- [1] M. L. Wolford, K. Palso, and A. Bercovitz. Hospitalization for Total Hip Replacement Among Inpatients Aged 45 and Over: United States, 2000–2010. NCHS data brief, no 186. Technical report, National Center for Health Statistics, 2015.
- [2] NJR StatsOnline. National Joint Registry Database, NHS Hip procedures 2004–2014. Technical report, National Joint Registry, 2016.
- [3] D. C. Bassett, A. G. Håti, T. B. Melø, B. T. Stokke, and P. Sikorski. Competitive ligand exchange of crosslinking ions for ionotropic hydrogel formation. *Journal of Materials Chemistry B*, 4(37):6175–6182, 2016.
- [4] I. Levêque, K. H. Rhodes, and S. Mann. Biomineral-inspired fabrication of semi-permeable calcium phosphate-polysaccharide microcapsules. *Journal of Materials Chemistry*, 12(8):2178–2180, 2002.
- [5] F. Despang, A. Börner, R. Dittrich, G. Tomandl, W. Pompe, and M. Gelsky. Alginate/calcium phosphate scaffolds with oriented, tube-like pores. *Materialwissenschaft und Werkstofftechnik*, 36(12):761–767, 2005.
- [6] M. Xie, M. O. Olderoy, Z. Zhang, J.-P. Andreassen, B. L. Strand, and P. Sikorski. Biocomposites prepared by alkaline phosphatase mediated mineralization of alginate microbeads. *RSC Advances*, 2(4):1457–1465, 2012.
- [7] M. Westhrin, M. Xie, M. Ø. Olderøy, P. Sikorski, B. L. Strand, and T. Standal. Osteogenic Differentiation of Human Mesenchymal Stem Cells in Mineralized Alginate Matrices. *Plos One*, 10(3):e0120374, 2015.
- [8] J. Sun and B. Bhushan. Hierarchical structure and mechanical properties of nacre: a review. *RSC Advances*, 2(20):7617–7632, 2012.
- [9] S. Deville, E. Saiz, R. K. Nalla, and A. P. Tomsia. Freezing as a Path to Build Complex Composites. *Science*, 311(5760):515–518, 2006.
- [10] R. O. Ritchie, R. K. Nalla, J. J. Kruzic, W. Ager III, G. Balooch, and J. H. Kinney. Fracture and ageing in bone: Toughness and structural characterization. *Strain*, 42(4):225–232, 2006.
- [11] J. Aizenberg, J. C. Weaver, M. S. Thanawala, V. C. Sundar, D. E. Morse, and P. Fratzl. Skeleton of *Euplectella* sp.: Structural Hierarchy from the Nanoscale to the Macroscale. *Science*, 309(5732):275–278, 2005.

- [12] J.-Y. Rho, L. Kuhn-Spearing, and P. Zioupos. Mechanical properties and the hierarchical structure of bone. *Medical engineering & physics*, 20(2): 92–102, 1998.
- [13] S. Weiner and H. D. Wagner. THE MATERIAL BONE: Structure-Mechanical Function Relations. *Annual Review of Materials Science*, 28 (1):271–298, 1998.
- [14] T. Bellido. Osteocyte-driven bone remodeling. *Calcified Tissue International*, 94(1):25–34, 2014.
- [15] G. A. Rodan. Bone homeostasis. *Proceedings of the National Academy of Sciences of the United States of America*, 95(23):13361–13362, 1998.
- [16] A. Schindeler, M. M. McDonald, P. Bokko, and D. G. Little. Bone remodeling during fracture repair: The cellular picture. *Seminars in cell & developmental biology*, 19(5):459–466, 2008.
- [17] D. Y. Wu, S. Meure, and D. Solomon. Self-healing polymeric materials: A review of recent developments. *Progress in Polymer Science*, 33(5):479–522, 2008.
- [18] D. J. Schneck and J. D. Bronzino, editors. *Biomechanics Principles and applications*. CRC Press, 2002.
- [19] E. Bonucci. *Biological Calcification*. Springer-Verlag Berlin Heidelberg, 2007.
- [20] L. L. Hench. Biomaterials. *Science*, 208(4446):826–831, 1980.
- [21] M. N. Rahaman, D. E. Day, B. Sonny Bal, Q. Fu, S. B. Jung, L. F. Bonewald, and A. P. Tomsia. Bioactive glass in tissue engineering. *Acta Biomaterialia*, 7(6):2355–2373, 2011.
- [22] A. Hoppe, N. S. Gldal, and A. R. Boccaccini. A review of the biological response to ionic dissolution products from bioactive glasses and glass-ceramics. *Biomaterials*, 32(11):2757–2774, 2011.
- [23] J. M. Anderson, A. Rodriguez, and D. T. Chang. Foreign body reaction to biomaterials. *Seminars in Immunology*, 20(2):86–100, 2008.
- [24] A. R. Amini, C. T. Laurencin, and S. P. Nukavarapu. Bone Tissue Engineering: Recent Advances and Challenges. *Critical Reviews in Biomedical Engineering*, 40(5):363–408, 2012.
- [25] P. Gentile, V. Chiono, I. Carmagnola, and P. V. Hatton. An overview of poly(lactic-co-glycolic) Acid (PLGA)-based biomaterials for bone tissue engineering. *International Journal of Molecular Sciences*, 15(3):3640–3659, 2014.
- [26] A. V. Mironov, A. M. Grigoryev, L. I. Krotova, N. N. Skaletsky, V. K. Popov, and V. I. Sevastianov. 3D printing of PLGA scaffolds for tissue engineering. *Journal of Biomedical Materials Research Part A*, 105(1):104–109, 2016.

- [27] L. L. Hench and J. M. Polak. Third-generation biomedical materials. *Science*, 295(5557):1014–1017, 2002.
- [28] F. M. Chen, M. Zhang, and Z. F. Wu. Toward delivery of multiple growth factors in tissue engineering. *Biomaterials*, 31(24):6279–6308, 2010.
- [29] D. F. Williams. *The Williams dictionary of biomaterials*. Liverpool University Press, 1999.
- [30] P. Fratzl, editor. *Collagen. Structure and mechanics*. Springer Science & Business Media, 2008.
- [31] A. V. Taubenberger, M. A. Woodruff, H. Bai, D. J. Muller, and D. W. Hutmacher. The effect of unlocking RGD-motifs in collagen I on pre-osteoblast adhesion and differentiation. *Biomaterials*, 31(10):2827–2835, 2010.
- [32] H. K. Kleinman, R. J. Klebe, and G. R. Martin. Role of collagenous matrices in the adhesion and growth of cells. *Journal of Cell Biology*, 88(3):473–485, 1981.
- [33] G. T. Grant, E. R. Morris, D. A. Rees, P. J. Smith, and D. Thom. Biological interactions between polysaccharides and divalent cations: The egg-box model. *FEBS Letters*, 32(1):195–198, 1973.
- [34] I. Donati, S. Holtan, Y. A. Mørch, M. Borgogna, M. Dentini, and G. Skjåk-Braek. New hypothesis on the role of alternating sequences in calcium-alginate gels. *Biomacromolecules*, 6(2):1031–1040, 2005.
- [35] M. A. Patel, M. H. AbouGhaly, J. V. Schryer-Praga, and K. Chadwick. The effect of ionotropic gelation residence time on alginate cross-linking and properties. *Carbohydrate Polymers*, 155(2017):362–371, 2017.
- [36] T. Andersen, B. L. Strand, K. Formo, E. Alsberg, and B. E. Christensen. Alginates as biomaterials in tissue engineering. In *Carbohydrate Chemistry : Volume 37*, chapter 9, pages 227–258. The Royal Society of Chemistry, 2012.
- [37] A. M. Rokstad, B. L. Strand, K. Rian, B. Steinkjer, B. Kulseng, G. Skjåk-Braek, and T. Espevik. Evaluation of different types of alginate microcapsules as bioreactors for producing endostatin. *Cell Transplantation*, 12:351–364, 2003.
- [38] N. G. Genes, J. A. Rowley, D. J. Mooney, and L. J. Bonassar. Effect of substrate mechanics on chondrocyte adhesion to modified alginate surfaces. *Archives of Biochemistry and Biophysics*, 422(2):161–167, 2004.
- [39] S. J. Bidarra, C. C. Barrias, K. B. Fonseca, M. A. Barbosa, R. A. Soares, and P. L. Granja. Injectable in situ crosslinkable RGD-modified alginate matrix for endothelial cells delivery. *Biomaterials*, 32(31):7897–7904, 2011.

- [40] M. B. Evangelista, S. X. Hsiong, R. Fernandes, P. Sampaio, H.-J. Kong, C. C. Barrias, R. Salema, M. A. Barbosa, D. J. Mooney, and P. L. Granja. Upregulation of bone cell differentiation through immobilization within a synthetic extracellular matrix. *Biomaterials*, 28(25):3644–3655, 2007.
- [41] A. D. Augst, H. J. Kong, and D. J. Mooney. Alginate hydrogels as biomaterials. *Macromolecular bioscience*, 6(8):623–633, 2006.
- [42] W. Cook. Alginate dental impression materials: chemistry, structure, and properties. *Journal of biomedical materials research*, 20(1):1–24, 1986.
- [43] T. Hashimoto, Y. Suzuki, M. Tanihara, Y. Kakimaru, and K. Suzuki. Development of alginate wound dressings linked with hybrid peptides derived from laminin and elastin. *Biomaterials*, 25(7):1407–1414, 2004.
- [44] J. Zhang, Q. Wang, and A. Wang. In situ generation of sodium alginate/hydroxyapatite nanocomposite beads as drug-controlled release matrices. *Acta biomaterialia*, 6(2):445–454, 2010.
- [45] R. Z. LeGeros. Calcium Phosphate-Based Osteoinductive Materials. *Chemical Reviews*, 108(11):4742–4753, 2008.
- [46] C. Combes and C. Rey. Amorphous calcium phosphates: Synthesis, properties and uses in biomaterials. *Acta Biomaterialia*, 6(9):3362–3378, 2010.
- [47] S. V. Dorozhkin and M. Epple. Biological and medical significance of calcium phosphates. *Angewandte Chemie International Edition*, 41(17):3130–3146, 2002.
- [48] J. C. Elliott. *Structure and Chemistry of the Apatites and Other Calcium Orthophosphates*. Elsevier Science B.V., 1994.
- [49] M. Tung, N. Eidelman, B. Sieck, and W. Brown. Octacalcium Phosphate Solubility Product from 4 to 37-Degree-C. *Journal of Research of the National Bureau of Standards*, 93(5):613–624, 1988.
- [50] L. Wang and G. H. Nancollas. Calcium orthophosphates: Crystallization and Dissolution. *Chemical Reviews*, 108(11):4628–4669, 2008.
- [51] B. O. Fowler and S. Kuroda. Changes in heated and in laser-irradiated human tooth enamel and their probable effects on solubility. *Calcified Tissue International*, 38(4):197–208, 1986.
- [52] M. Bohner. Calcium orthophosphates in medicine: from ceramics to calcium phosphate cements. *Injury*, 31:S–D37–47, 2000.
- [53] H. Monma and T. Kanazawa. The hydration of α -tricalcium phosphate. *Journal of the Ceramic Association, Japan*, 84:209–213, 1976.
- [54] U. Gbureck, J. E. Barralet, K. Spatz, L. M. Grover, and R. Thull. Ionic modification of calcium phosphate cement viscosity. Part I: hypodermic injection and strength improvement of apatite cement. *Biomaterials*, 25(11):2187–2195, 2004.

- [55] O. Gauthier, I. Khairoun, J. Bosco, L. Obadia, X. Bourges, C. Rau, D. Magne, J. M. Bouler, E. Aguado, G. Daculsi, and P. Weiss. Noninvasive bone replacement with a new injectable calcium phosphate biomaterial. *Journal of Biomedical Materials Research*, 66A(1):47–54, 2003.
- [56] U. Gbureck, T. Hölzel, C. J. Doillon, F. A. Müller, and J. E. Barralet. Direct Printing of Bioceramic Implants with Spatially Localized Angiogenic Factors. *Advanced Materials*, 19(6):795–800, 2007.
- [57] A. A. Mirtchi, J. Lemaître, and E. Munting. Calcium phosphate cements: action of setting regulators on the properties of the beta-tricalcium phosphate-monocalcium phosphate cements. *Biomaterials*, 10(9):634–638, 1989.
- [58] F. Tamimi, Z. Sheikh, and J. Barralet. Dicalcium phosphate cements: brushite and monetite. *Acta biomaterialia*, 8(2):474–487, 2012.
- [59] B. Kanter, M. Geffers, A. Ignatius, and U. Gbureck. Control of in vivo mineral bone cement degradation. *Acta Biomaterialia*, 10(7):3279–3287, 2014.
- [60] U. Klammert, A. Ignatius, U. Wolfram, T. Reuther, and U. Gbureck. In vivo degradation of low temperature calcium and magnesium phosphate ceramics in a heterotopic model. *Acta Biomaterialia*, 7(9):3469–3475, 2011.
- [61] W. Chen, W. Thein-Han, M. D. Weir, Q. Chen, and H. H. K. Xu. Pre-vascularization of biofunctional calcium phosphate cement for dental and craniofacial repairs. *Dental materials : official publication of the Academy of Dental Materials*, 30(5):535–544, 2014.
- [62] R. Langer and J. P. Vacanti. Tissue Engineering. *Science*, 260:920–926, 1993.
- [63] R. Skalak and C. F. Fox. *Tissue engineering: proceedings of a workshop*. Liss, 1988.
- [64] R. M. Nerem. Cellular engineering. *Annals of Biomedical Engineering*, 19(5):529–545, 1991.
- [65] A. J. Vegas, O. Veisoh, M. Gürtler, J. R. Millman, F. W. Pagliuca, A. R. Bader, J. C. Doloff, J. Li, M. Chen, K. Olejnik, H. H. Tam, S. Jhunjhunwala, E. Langan, S. Aresta-Dasilva, S. Gandham, J. J. McGarrigle, M. A. Bochenek, J. Hollister-Lock, J. Oberholzer, D. L. Greiner, G. C. Weir, D. A. Melton, R. Langer, and D. G. Anderson. Long-term glycemc control using polymer-encapsulated human stem cell-derived beta cells in immune-competent mice. *Nature Medicine*, 22(3):306–311, 2016.
- [66] J. Patterson, M. M. Martino, and J. a. Hubbell. Biomimetic materials in tissue engineering. *Materials Today*, 13(1-2):14–22, 2010.
- [67] Y. T. Matsunaga, Y. Morimoto, and S. Takeuchi. Molding cell beads for rapid construction of macroscopic 3D tissue architecture. *Advanced materials*, 23(12):H90–H94, 2011.

- [68] F. G. Lyons, A. A. Al-Munajjed, S. M. Kieran, M. E. Toner, C. M. Murphy, G. P. Duffy, and F. J. O'Brien. The healing of bony defects by cell-free collagen-based scaffolds compared to stem cell-seeded tissue engineered constructs. *Biomaterials*, 31(35):9232–9243, 2010.
- [69] K. Rezwan, Q. Chen, J. Blaker, and A. R. Boccaccini. Biodegradable and bioactive porous polymer/inorganic composite scaffolds for bone tissue engineering. *Biomaterials*, 27(18):3413–3431, 2006.
- [70] S. B. Lee, Y. H. Kim, M. S. Chong, S. H. Hong, and Y. M. Lee. Study of gelatin-containing artificial skin V: Fabrication of gelatin scaffolds using a salt-leaching method. *Biomaterials*, 26(14):1961–1968, 2005.
- [71] C. J. Damien and J. R. Parsons. Bone graft and bone graft substitutes: A review of current technology and applications. *Journal of Applied Biomaterials*, 2(3):187–208, 1991.
- [72] Y. M. Kolambkar, K. M. Dupont, J. D. Boerckel, N. Huebsch, D. J. Mooney, D. W. Hutmacher, and R. E. Guldberg. An alginate-based hybrid system for growth factor delivery in the functional repair of large bone defects. *Biomaterials*, 32(1):65–74, 2011.
- [73] P. Kasten, R. Luginbühl, M. van Griensven, T. Barkhausen, C. Krettek, M. Bohner, and U. Bosch. Comparison of human bone marrow stromal cells seeded on calcium-deficient hydroxyapatite, β -tricalcium phosphate and demineralized bone matrix. *Biomaterials*, 24(15):2593–2603, 2003.
- [74] Y. Liu, J. Lim, and S.-H. Teoh. Review: Development of clinically relevant scaffolds for vascularised bone tissue engineering. *Biotechnology Advances*, 31(5):688–705, 2013.
- [75] I. Zein, D. W. Hutmacher, K. C. Tan, and S. H. Teoh. Fused deposition modeling of novel scaffold architectures for tissue engineering applications. *Biomaterials*, 23(4):1169–1185, 2002.
- [76] D. W. Hutmacher, J. C. H. Goh, and S. H. Teoh. An introduction to biodegradable materials for tissue engineering applications. *Annals of the Academy of Medicine Singapore*, 30(2):183–191, 2001.
- [77] Y. Khan, M. J. Yaszemski, A. G. Mikos, and C. T. Laurencin. Tissue engineering of bone: material and matrix considerations. *The Journal of Bone and Joint Surgery*, 90 Suppl 1(Suppl 1):36–42, 2008.
- [78] K. H. Bae, L.-S. Wang, and M. Kurisawa. Injectable biodegradable hydrogels: progress and challenges. *Journal of Materials Chemistry B*, 1(40):5371–5388, 2013.
- [79] T. R. Hoare and D. S. Kohane. Hydrogels in drug delivery: Progress and challenges. *Polymer*, 49(8):1993–2007, 2008.

- [80] Y. M. Kolambkar, J. D. Boerckel, K. M. Dupont, M. Bajin, N. Huebsch, D. J. Mooney, D. W. Hutmacher, and R. E. Guldberg. Spatiotemporal delivery of bone morphogenetic protein enhances functional repair of segmental bone defects. *Bone*, 49(3):485–492, 2011.
- [81] E. J. Carragee, E. L. Hurwitz, and B. K. Weiner. A critical review of recombinant human bone morphogenetic protein-2 trials in spinal surgery: emerging safety concerns and lessons learned. *The Spine Journal*, 11(6):471–491, 2011.
- [82] J. R. Dimar, S. D. Glassman, K. Burkus, P. W. Pryor, J. W. Hardacker, and L. Y. Carreon. Clinical and Radiographic Analysis of an Optimized rhBMQ-2 Formulation as an Autograft Replacement in Posterolateral Lumbar Spine Arthrodesis. *Journal of Bone and Joint Surgery*, 91(6):1377–1386, 2009.
- [83] J. B. Albillos, H. C. Tenenbaum, C. M. L. Clokie, D. R. Walt, G. I. Baker, D. J. Psutka, D. Backstein, and S. A. F. Peel. Serum levels of BMP-2, 4, 7 and AHSR in patients with degenerative joint disease requiring total arthroplasty of the hip and temporomandibular joints. *Journal of Orthopaedic Research*, 31(1):44–52, 2013.
- [84] M. Sumper and E. Brunner. Learning from Diatoms: Nature’s Tools for the Production of Nanostructured Silica. *Advanced Functional Materials*, 16(1):17–26, 2006.
- [85] D. Kashchiev and G. M. van Rosmalen. Review: Nucleation in solutions revisited. *Crystal Research and Technology*, 38(78):555–574, 2003.
- [86] A. George and A. Veis. Phosphorylated Proteins and Control over Apatite Nucleation, Crystal Growth, and Inhibition. *Chemical Reviews*, 108(11):4670–4693, 2008.
- [87] H. Cölfen, L. Qi, Y. Mastai, and L. Börger. Formation of Unusual 10-Petal BaSO₄ Structures in the Presence of a Polymeric Additive. *Crystal Growth & Design*, 2(3):191–196, 2002.
- [88] G. Falini, S. Albeck, S. Weiner, and L. Addadi. Control of Aragonite or Calcite Polymorphism by Mollusk Shell Macromolecules. *Source: Science, New Series*, 27124087(5245):67–69, 1996.
- [89] A. K. Rajasekharan and M. Andersson. Role of Nanoscale Confinement on Calcium Phosphate Formation at High Supersaturation. *Crystal Growth & Design*, 15(6):2775–2780, 2015.
- [90] Y.-W. Wang, H. K. Christenson, and F. C. Meldrum. Confinement Increases the Lifetimes of Hydroxyapatite Precursors. *Chemistry of Materials*, 26(20):5830–5838, 2014.
- [91] B. Cantaert, E. Beniash, and F. C. Meldrum. Nanoscale confinement controls the crystallization of calcium phosphate: relevance to bone formation. *Chemistry - A European Journal*, 19(44):14918–14924, 2013.

- [92] T. Threlfall. Structural and Thermodynamic Explanations of Ostwald's Rule. *Organic Process Research and Development*, 7(6):1017–1027, 2003.
- [93] J. D. Termine and A. S. Posner. Amorphous/Crystalline Interrelationships in Bone Mineral. *Calcified Tissue Research*, 1(1):8–23, 1967.
- [94] J. Mahamid, A. Sharir, L. Addadi, and S. Weiner. Amorphous calcium phosphate is a major component of the forming fin bones of zebrafish: Indications for an amorphous precursor phase. *Proceedings of the National Academy of Sciences of the United States of America*, 105(35):12748–12753, 2008.
- [95] G. Campi, A. Ricci, A. Guagliardi, C. Giannini, S. Lagomarsino, R. Cancedda, M. Mastrogiacomo, and A. Cedola. Early stage mineralization in tissue engineering mapped by high resolution X-ray microdiffraction. *Acta biomaterialia*, 8(9):3411–3418, 2012.
- [96] S. Mann. *Biom mineralization : principles and concepts in bioinorganic materials chemistry*. Oxford University Press, 2001.
- [97] G. Cao and Y. Wang. *Nanostructures and Nanomaterials: Synthesis, Properties, and Applications*. World Scientific, 2004.
- [98] J. W. Mullin. *Crystallization*. Butterworth-Heinemann, 4th edition, 2001.
- [99] F. C. Frank. The influence of dislocations on crystal growth. *Discussions of the Faraday Society*, 5:48–54, 1949.
- [100] S. A. Morin, A. Forticaux, M. J. Bierman, and S. Jin. Screw Dislocation-Driven Growth of Two-Dimensional Nanoplates. *Nano Letters*, 11(10):4449–4455, 2011.
- [101] F. C. Meldrum and H. Cölfen. Controlling Mineral Morphologies and Structures in Biological and Synthetic Systems. *Chemical Reviews*, 108(11):4332–4432, 2008.
- [102] J. J. De Yoreo, P. U. P. A. Gilbert, N. A. J. M. Sommerdijk, R. L. Penn, S. Whitlam, D. Joester, H. Zhang, J. D. Rimer, A. Navrotsky, J. F. Banfield, A. F. Wallace, F. M. Michel, F. C. Meldrum, H. Colfen, and P. M. Dove. Crystallization by particle attachment in synthetic, biogenic, and geologic environments. *Science*, 349(6247):aaa6760–1–aaa6760–9, 2015.
- [103] M. Gong, A. Kirkeminde, and S. Ren. Symmetry-Defying Iron Pyrite (FeS₂) Nanocrystals through Oriented Attachment. *Scientific reports*, 3:2092, 2013.
- [104] L.-r. Meng, W. Chen, C. Chen, H. Zhou, Q. Peng, and Y. Li. Uniform α -Fe₂O₃ Nanocrystal Moniliforme-Shape Straight-Chains. *Crystal Growth & Design*, 10(2):479–482, 2010.
- [105] D. Faivre and D. Schuler. Magnetotactic Bacteria and Magnetosomes. *Chemical Reviews*, 108:4875–4898, 2008.

- [106] L. B. Gower and D. J. Odom. Deposition of calcium carbonate films by a polymer-induced liquid-precursor (PILP) process. *Journal of Crystal Growth*, 210(4):719–734, 2000.
- [107] S. E. Wolf, L. Müller, R. Barrea, C. J. Kampf, J. Leiterer, U. Panne, T. Hoffmann, F. Emmerling, and W. Tremel. Carbonate-coordinated metal complexes precede the formation of liquid amorphous mineral emulsions of divalent metal carbonates. *Nanoscale*, 3(3):1158–1165, 2011.
- [108] D. Gebauer, M. Kellermeier, J. D. Gale, L. Bergström, and H. Cölfen. Prenucleation clusters as solute precursors in crystallisation. *Chemical Society reviews*, 43(7):2348–2371, 2014.
- [109] D. Gebauer, A. Völkel, and H. Cölfen. Stable prenucleation calcium carbonate clusters. *Science*, 322(5909):1819–1822, 2008.
- [110] E. M. Pouget, P. H. H. Bomans, J. A. C. M. Goos, P. M. Frederik, G. de With, and N. A. J. M. Sommerdijk. The Initial Stages of Template-Controlled CaCO₃ Formation Revealed by Cryo-TEM. *Science*, 323:1455–1458, 2009.
- [111] J.-P. Andreassen, R. Beck, and M. Nergaard. Biomimetic type morphologies of calcium carbonate grown in absence of additives. *Faraday Discussions*, 159:247–261, 2012.
- [112] Y.-Y. Kim, A. S. Schenk, J. Ihli, A. N. Kulak, N. B. J. Hetherington, C. C. Tang, W. W. Schmahl, E. Griesshaber, G. Hyett, and F. C. Meldrum. A critical analysis of calcium carbonate mesocrystals. *Nature Communications*, 5:328–356, 2014.
- [113] N. A. J. M. Sommerdijk and G. de With. Biomimetic CaCO₃ mineralization using designer molecules and interfaces. *Chemical Reviews*, 108(11):4499–4550, 2008.
- [114] S. Bentov, S. Weil, L. Glazer, A. Sagi, and A. Berman. Stabilization of amorphous calcium carbonate by phosphate rich organic matrix proteins and by single phosphoamino acids. *Journal of Structural Biology*, 171(2):207–215, 2010.
- [115] N. A. J. M. Sommerdijk and H. Cölfen. Lessons from Nature—Biomimetic Approaches to Minerals with Complex Structures. *MRS Bulletin*, 35(02):116–121, 2010.
- [116] S. Hild, O. Marti, and A. Ziegler. Spatial distribution of calcite and amorphous calcium carbonate in the cuticle of the terrestrial crustaceans *Porcellio scaber* and *Armadillidium vulgare*. *Journal of Structural Biology*, 163(1):100–108, 2008.
- [117] S. Weiner, I. Sagi, and L. Addadi. Choosing the Crystallization Path Less Traveled. *Science*, 309(August):1027–1028, 2005.

- [118] J. Mahamid, A. Sharir, D. Gur, E. Zelzer, L. Addadi, and S. Weiner. Bone mineralization proceeds through intracellular calcium phosphate loaded vesicles: a cryo-electron microscopy study. *Journal of structural biology*, 174(3): 527–535, 2011.
- [119] L. Addadi, S. Raz, and S. Weiner. Taking advantage of disorder: Amorphous calcium carbonate and its roles in biomineralization. *Advanced Materials*, 15(12):959–970, 2003.
- [120] M. J. Olszta, X. Cheng, S. S. Jee, R. Kumar, Y.-Y. Kim, M. J. Kaufman, E. P. Douglas, and L. B. Gower. Bone structure and formation: A new perspective. *Materials Science and Engineering: R: Reports*, 58(3-5):77–116, 2007.
- [121] I. Jäger and P. Fratzl. Mineralized Collagen Fibrils: A Mechanical Model with a Staggered Arrangement of Mineral Particles. *Biophysical Journal*, 79(4):1737–1746, 2000.
- [122] C. Hellmich and F.-J. Ulm. Are mineralized tissues open crystal foams reinforced by crosslinked collagen?—some energy arguments. *Journal of Biomechanics*, 35(9):1199–1212, 2002.
- [123] P. A. Price, D. Toroian, and J. E. Lim. Mineralization by inhibitor exclusion. The calcification of collagen with fetuin. *Journal of Biological Chemistry*, 284(25):17092–17101, 2009.
- [124] W. Traub, T. Arad, and S. Weiner. Origin of Mineral Crystal Growth in Collagen Fibrils. *Matrix*, 12(4):251–255, 1992.
- [125] L. B. Gower. Biomimetic Model Systems for Investigating the Amorphous Precursor Pathway and Its Role in Biomineralization. *Chemical Reviews*, 108(11):4551–4627, 2008.
- [126] F. Nudelman, K. Pieterse, A. George, P. H. H. Bomans, H. Friedrich, L. J. Brylka, P. A. J. Hilbers, G. de With, and N. A. J. M. Sommerdijk. The role of collagen in bone apatite formation in the presence of hydroxyapatite nucleation inhibitors. *Nature materials*, 9(12):1004–1009, 2010.
- [127] K. Bleek and A. Taubert. New developments in polymer-controlled, bioinspired calcium phosphate mineralization from aqueous solution. *Acta biomaterialia*, 9(5):6283–6321, 2013.
- [128] H. Ping, H. Xie, B.-L. Su, Y.-b. Cheng, W. Wang, H. Wang, Y. Wang, J. Zhang, F. Zhang, and Z. Fu. Organized intrafibrillar mineralization, directed by a rationally designed multi-functional protein. *Journal of Materials Chemistry B*, 3(22):4496–4502, 2015.
- [129] S. Ucar, S. H. Bjørnøy, D. C. Bassett, B. L. Strand, P. Sikorski, and J.-P. Andreassen. Nucleation and Growth of Brushite in the Presence of Alginate. *Crystal Growth & Design*, 15(11):5397–5405, 2015.

- [130] S. Ucar, S. H. Bjørnøy, D. C. Bassett, B. L. Strand, P. Sikorski, and J.-P. Andreassen. Transformation of brushite to hydroxyapatite and effects of alginate additives. *Journal of Crystal Growth*, page In Press, 2016.
- [131] B. Huang, M. Bates, and X. Zhuang. Super-Resolution Fluorescence Microscopy. *Annual Review of Biochemistry*, 78(1):993–1016, 2009.
- [132] D. Brandon and W. D. Kaplan. *Microstructural characterization of materials*. John Wiley & Sons, Inc., 2nd edition, 2008.
- [133] S. Bertazzo, E. Gentleman, K. L. Cloyd, A. H. Chester, M. H. Yacoub, and M. M. Stevens. Nano-analytical electron microscopy reveals fundamental insights into human cardiovascular tissue calcification. *Nature materials*, 12(6):576–583, 2013.
- [134] F. J. Timmermans and C. Otto. Contributed Review: Review of integrated correlative light and electron microscopy. *Review of Scientific Instruments*, 86(1):011501, 2015.
- [135] P. de Boer, J. P. Hoogenboom, and B. N. G. Giepmans. Correlated light and electron microscopy: ultrastructure lights up! *Nature methods*, 12(6):503–513, 2015.
- [136] J. R. Ferraro, K. Nakamoto, and C. W. Brown. *Introductory Raman spectroscopy*. Academic Press, 2nd edition, 2003.
- [137] T. Dieing, O. Hollricher, and J. Toporski. *Confocal Raman Microscopy*. Springer Science & Business Media, 2010.
- [138] N. J. Crane, V. Popescu, M. D. Morris, P. Steenhuis, and M. A. Ignelzi. Raman spectroscopic evidence for octacalcium phosphate and other transient mineral species deposited during intramembranous mineralization. *Bone*, 39(3):434–442, 2006.
- [139] M. J. Duer. The contribution of solid-state NMR spectroscopy to understanding biomineralization: Atomic and molecular structure of bone. *Journal of Magnetic Resonance*, 253:98–110, 2015.
- [140] Y. K. Min, T. Yamamoto, E. Kohda, T. Ito, and H. O. Hamaguchi. 1064 nm near-infrared multichannel Raman spectroscopy of fresh human lung tissues. *Journal of Raman Spectroscopy*, 36(1):73–76, 2005.
- [141] M. Müller and A. Zumbusch. Coherent anti-Stokes Raman scattering microscopy. *ChemPhysChem*, 8(15):2157–2170, 2007.
- [142] J. Zięba-Palus and A. Michalska. Photobleaching as a useful technique in reducing of fluorescence in Raman spectra of blue automobile paint samples. *Vibrational Spectroscopy*, 74:6–12, 2014.
- [143] B. K. Vainshtein. *Diffraction of X-rays by chain molecules*. Elsevier Publishing Company, 1st edition, 1966.

- [144] L. Reimer. *Transmission Electron Microscopy*. Springer, 1997.
- [145] Y. Waseda, E. Matsubara, and K. Shinoda. *X-Ray Diffraction Crystallography*. Springer Science & Business Media, 2011.
- [146] G. Williamson and W. Hall. X-ray line broadening from filed aluminium and wolfram. *Acta Metallurgica*, 1(1):22–31, 1953.
- [147] D. Wiles and R. Young. A new computer program for Rietveld analysis of X-ray powder diffraction patterns. *Journal of Applied Crystallography*, 14: 149–151, 1981.
- [148] D. L. Bish and J. E. Post. Quantitative mineralogical analysis using the Rietveld full-pattern fitting method. *American Mineralogist*, 78(9-10):932–940, 1993.
- [149] H. M. Rietveld. A profile refinement method for nuclear and magnetic structures. *Journal of Applied Crystallography*, 2(2):65–71, 1969.
- [150] D. L. Bish and S. A. Howard. Quantitative phase analysis using the Rietveld method. *Journal of Applied Crystallography*, 21:86–91, 1988.
- [151] B. D. Cullity. *Elements of X-Ray Diffraction*. Prentice Hall, 3rd edition, 2001.
- [152] A. Mikkelsen and A. Elgsaeter. Density distribution of calcium-induced alginate gels. A numerical study. *Biopolymers*, 36(1):17–41, 1995.
- [153] S. H. Bjørnøy, D. C. Bassett, S. Ucar, J.-P. Andreassen, and P. Sikorski. Letter to the Editor re “Characterization of alginate-brushite in-situ hydrogel composites”. *Materials Science and Engineering: C*, 70(1):930–931, 2017.
- [154] A. Akiva, M. Kerschnitzki, I. Pinkas, W. Wagermaier, K. Yaniv, P. Fratzl, L. Addadi, and S. Weiner. Mineral formation in the larval zebrafish tail bone occurs via an acidic disordered calcium phosphate phase. *Journal of the American Chemical Society*, 138(43):14481–14487, 2016.

Paper I

Biomedical Materials



PAPER

Controlled mineralisation and recrystallisation of brushite within alginate hydrogels

Sindre H Bjørnøy¹, David C Bassett¹, Seniz Ucar², Jens-Petter Andreassen² and Pawel Sikorski¹

¹ Department of Physics, Norwegian University of Science and Technology, 7491 Trondheim, Norway

² Department of Chemical Engineering, Norwegian University of Science and Technology, 7491 Trondheim, Norway

E-mail: pawel.sikorski@ntnu.no

Keywords: alginate, biomineralisation, hybrid materials, hydrogels, brushite

Online supplementary data available from [online](#)

RECEIVED
16 July 2015

REVISED
16 October 2015

ACCEPTED FOR PUBLICATION
10 November 2015

PUBLISHED
2 February 2016

Abstract

Due to high solubility and fast resorption behaviour under physiological conditions, brushite ($\text{CaHPO}_4 \cdot 2\text{H}_2\text{O}$, calcium monohydrogen phosphate dihydrate, dicalcium phosphate dihydrate) has great potential in bone regeneration applications, both in combination with scaffolds or as a component of calcium phosphate cements. The use of brushite in combination with hydrogels opens up possibilities for new cell-based tissue engineering applications of this promising material. However, published preparation methods of brushite composites, in which the mineral phase is precipitated within the hydrogel network, fail to offer the necessary degree of control over the mineral phase, content and distribution within the hydrogel matrix. The main focus of this study is to address these shortcomings by determining the precise fabrication parameters needed to prepare composites with controlled composition and properties. Composite alginate microbeads were prepared using a counter-diffusion technique, which allows for the simultaneous crosslinking of the hydrogel and precipitation of an inorganic mineral phase. Reliable nucleation of a desired mineral phase within the alginate network proved more challenging than simple aqueous precipitation. This was largely due to ion transport within the hydrogel producing concentration gradients that modified levels of supersaturation and favoured the nucleation of other phases such as hydroxyapatite and octacalcium phosphate, which would otherwise not form. To overcome this, the incorporation of brushite seed crystals resulted in good control during the mineral phase, and by adjusting the number of seeds and amount of precursor concentration, the amount of mineral could be tuned. The material was characterised with a range of physical techniques, including scanning electron microscopy, powder x-ray diffraction and Rietveld refinement, Fourier transform infrared spectroscopy, and thermogravimetric analysis, in order to assess the mineral morphology, phase and amount within the organic matrix. The mineral content of the composite material converted from brushite into hydroxyapatite when submerged in simulated body fluid, indicating possible bioactivity. Additionally, initial cell culture studies revealed that both the material and the synthesis procedure are compatible with cells relevant to bone tissue engineering.

1. Introduction

In cell-based tissue engineering (TE) there is a need for synthetic materials that can act as scaffolds for cells. These materials must be biocompatible, preferably biodegradable, and be able to provide an environment that ensures attachment, proliferation and sustained function of specific cell types [1, 2]. For bone TE, an ideal scaffold should have appropriate mechanical properties, provide an environment for nutrient and

growth factor exchange and have a certain porosity for cell migration and vascularisation [3]. Hydrogels are a class of polymeric networks capable of retaining large amounts of water and have shown good promise as TE scaffolds [4, 5]. Their hydrated form allows for the diffusion of nutrients and the delivery of bioactive agents, but their high water content also means that hydrogels are inherently soft materials with low mechanical strength and are therefore more suitable for soft tissues [6]. However, hydrogel-based scaffolds

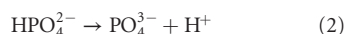
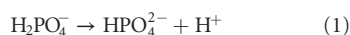
do possess the potential to be non-invasive, injectable temporary scaffolds which can deliver cells, growth factors, drugs or combinations of these to a damaged site [7]. Hydrogels can also be used in combination with load-bearing structures in order to promote the growth of new healthy bone and to aid in overcoming some of the challenges of metal implants, i.e. corrosion or implant rejection [8, 9].

Human bone tissue consists mainly of hydroxyapatite (HAp) nanocrystals in an ordered collagen matrix. The interplay between the stiff, but brittle, inorganic phase and the soft, but tough, organic phase, combined with a hierarchical design provides the extraordinary mechanical strength of this natural composite [10]. Adding an inorganic phase, such as HAp, to a hydrogel is one approach to improve the mechanical properties of the biomaterial, although so far the level required for load-bearing applications has not been reached [11–16]. However, cell response to mechanical stimuli has gained attention lately and tuning the mechanical properties of a scaffold may hold great potential [17]. It has also been shown that alginate mineralised with HAp improves cell adhesion, and the mineral itself can act as an osteoconductive surface [18–20].

For many years HAp has been the calcium phosphate (CaP) phase of choice for application in bone augmentation procedures owing to its likeness to natural bone mineral and stability under physiological conditions. There are, however, several other CaP phases that may dissolve or transform *in vivo* to allow or encourage natural remodelling procedures, thereby creating a bioactive implant. Both brushite ($\text{CaHPO}_4 \cdot 2\text{H}_2\text{O}$) and octacalcium phosphate (OCP) have been suggested as natural precursor phases to HAp, although *in vivo* evidence of this is rarely found [21]. Brushite has, over the past two decades, received a great deal of attention as a potential bioceramic in the repair of osseous tissue [22, 23]. The solubility of brushite is higher than that of HAp and OCP (pK_{sp} of 6.6, 58.6 and 48.7, respectively, at 37 °C) [24] and it therefore transforms readily into these phases in physiological conditions. The increased solubility offers a considerable advantage over alternative calcium phosphate-based materials as it may provide the space and necessary ions for natural bone remodelling and regeneration [23]. It has also been shown that the resorption rate of brushite is higher than for HAp [25]. There are, however, some issues with the long-term fate of large volumes of implanted brushite, as it has been shown to transform into more stable phases like OCP and HAp [26, 27]. This effect seems to be site-specific and is likely related to the *in vivo* fluid exchange in the sample location [28, 29]. Such behaviour has implications for the choice of brushite to fill large bone lesions. Interest in brushite as a biomaterial is mounting, and while there are many examples of promising HAp-alginate composites, there is very little literature regarding brushite in combination with hydrogels. Brushite powder has

been incorporated into an alginate matrix for fertiliser purposes and the recrystallisation of brushite in alginate at a cement-hydrogel interface has been studied by Raman-spectroscopy [30, 31]. A recent attempt was made by Amer *et al* to precipitate brushite *in situ* with alginate [32]. While mineral was formed within the hydrogel, little attention was paid to the reaction conditions or biocompatibility, which resulted in poorly defined composites and unstable gels. During preliminary experiments, we found that taking such an approach for the synthesis of a brushite alginate composite was unsatisfactory in terms of reaction control and reproducibility. Therefore, we sought to improve this synthesis by controlling the inherently dynamic reaction conditions of pH by using appropriate buffers and employed crystal seeds as a means to encourage the growth of phase pure brushite within the alginate matrix without recourse to use extreme reaction conditions that would be toxic to cells [33].

The driving force for the nucleation and growth of a specific phase in solution is supersaturation, i.e. the difference in chemical potential of a molecule in the solution and one in the crystal [34]. According to the literature, brushite is thermodynamically stable below approximately pH 4, but due to the nucleation and growth kinetics of different CaP phases, brushite can be precipitated at higher pH [35, 36]. However, it has been seen that for increasing precursor concentration, the pH at which brushite nucleates decreases [37, 38]. The pH affects the solubility and hence the supersaturation of the different phases in the $\text{Ca}(\text{OH})_2\text{--H}_3\text{PO}_4\text{--H}_2\text{O}$ system. The precipitation of CaP consumes, depending on the phase, either PO_4^{3-} or HPO_4^{2-} , which leads to a decrease in pH due to:



An indication of the bioactivity of a biomaterial for bone tissue engineering can be obtained by the formation of bone-like apatite on its surface when it is soaked in simulated body fluid (SBF) [39]. Despite the criticism and limitations of this technique [40–42], SBF has been regularly used to indicate the apatite-forming and bone-bonding abilities of biomaterials, and is generally accepted as a good initial test for *in vitro* behaviour. Here this technique was employed to study the transformation of brushite into HAp within an alginate–brushite composite, not to predict the *in vivo* behaviour of the material.

Our group has previously developed several strategies to mineralise alginate beads with HAp [14, 43]. In this study we investigated the mineralisation of alginate in the pH range of 5–7 with the specific aim of creating a bioactive composite material of alginate and brushite with controllable phase and mineral content, where the synthesis and/or material itself is cell-compatible.

2. Materials and methods

2.1. Chemical reagents

All the chemical reagents were purchased from Sigma-Aldrich, Norway unless otherwise stated. De-ionized water (DIW with a resistivity of 10–15 MΩcm) was used in all of the experiments.

2.2. Preparation of brushite-seeds

The brushite crystals were synthesised as follows. 500 ml of 0.4 M $\text{Ca}(\text{NO}_3)_2 \cdot 4\text{H}_2\text{O}$ and 500 ml of 0.4 M KH_2PO_4 and 26 mM KOH were prepared and bubbled with nitrogen gas. The solutions were mixed and the pH was monitored. The precipitates formed were aged by stirring for 2 h after the changes in pH stopped, before they were filtered and washed with DIW and ethanol. The crystals were dried at room temperature and their size was measured using a Coulter Counter Multisizer 3 (Beckman Coulter).

2.3. Composite beads made by counter-diffusion precipitation

The beads were made in a similar way to that which we have previously described [43]. Briefly, alginate with a guluronic acid residue fraction of $F_G = 0.68$, corresponding to 68% (FMC Biopolymer) was dissolved in DI-water to a final concentration of 1.8 wt% containing 0.9 wt% sodium chloride. A mixture of $\text{Na}_2\text{HPO}_4 \cdot 7\text{H}_2\text{O}$ and $\text{NaH}_2\text{PO}_4 \cdot 2\text{H}_2\text{O}$ was added to a phosphate concentration of 300 mM, where the ratio was decided by the final pH (5–7). The solution was stirred for at least 1 h. A gelling solution was made by dissolving calcium chloride in DI-water to give a final concentration of 1 M. Tris(hydroxymethyl)aminomethane (TRIS) or sodium acetate (NaAc) was used to buffer the solution at pH 7, or 6 and 5, respectively. The alginate solution was drawn from a needle with the help of a syringe pump and an electrostatic potential between the needle tip and the gelling bath. The needle diameter was 400 μm and it was electrostatically charged at a potential of 7 kV to ensure a uniform bead diameter of ~500 μm.

2.4. Composite beads made by counter-diffusion precipitation with brushite-seeds

For the seeded beads, brushite-powder was ground using an agate mortar and pestle to disrupt the aggregates formed during the drying process, and mixed with alginate solution (1.8% alginate, 0.9% NaCl, 300 mM PO_4^{3-} , pH 5) to a final concentration of 0.1 wt%, 1 wt% and 5 wt% of wet mass. The alginate solution was stirred for at least 1 h to ensure homogeneous mixing. Control beads with no phosphate precursor were made with the same seed concentration. The beads were made using the same technique described previously, however, only gelling bath with 1 M CaCl_2 , 0.9 wt% NaCl, and 100 mM sodium acetate at pH 5 was used.

2.5. Incubation in SBF

Simulated body fluid (SBF) was made following the instructions given by Kokubo and Takadama [39].

Beads made from 4 ml alginate solution were added into plastic tubes filled with 50 ml SBF-solution and placed at 37 °C. Beads containing originally 0.1 wt%, 1 wt% and 5 wt% brushite-seeds were kept in SBF-solution for 24 h, 72 h and 168 h, respectively, before they were removed and characterised. Non-mineralised beads without seeds were kept for 168 h in SBF before characterisation as a control.

2.6. Material characterisation

The beads were optically imaged in the wet state using an inverted microscope (Eclipse TS100, Nikon, Japan).

SEM analysis (Hitachi S-5500 S(T)EM) was performed with an acceleration voltage of 1–10 kV. The sample beads were dehydrated in increasing concentrations of ethanol. The ethanol was then substituted with acetone before they were critical point dried (Emitech K850 critical point dryer). The beads were placed on SEM-stubs with carbon tape and sputter coated (Cressington 208 HR) with a 5–10 nm layer of platinum/palladium (80/20). The chosen beads were cut in the wet state by embedding them in an alginate cylinder, gelled with the *in situ* technique [44], or agarose cylinder, where a 2% agarose solution was heated on a hot plate and the beads were introduced before the gel had set. These cylinders were cut into 100 or 200 μm sections using a vibrating blade microtome (VT1000S, Leica Biosystems, Nussloch GmbH, Germany). These sections were then dried and mounted using the same procedure as for the whole beads.

Powder XRD (D8 Advance DaVinci, Bruker AXS GmbH, Germany) was performed in the range of 5–75° with a step size of 0.013° and a step time of 0.67 s. The alginate-CaP composites were air-dried and crushed with a mortar and pestle before they were analysed. Rietveld analysis (Topas4.2, Bruker) was performed in order to assess the relative number of mineral phases. The background parameters, sample displacement, scale factor, crystallite size and cell parameters were refined. In order to check the reliability of the Rietveld analysis on the samples, an analysis of mixes of pure mineral samples with known sample ratios was performed.

Thermogravimetric analysis (TGA) (Netzsch STA449C TGA, Netzsch-Gerätebau GmbH, Germany) was performed in the temperature range of 25–1000 °C at a heating rate of 20 °C min⁻¹ under an air flow of 80 ml min⁻¹. A 20 min hold between 70–100 °C was performed in order to remove any adsorbed water. In order to estimate the mineral content in the beads, curves describing the sample residual mass $m(T)$ were modelled by adding a fraction f of the curve for the pure minerals to a fraction $1-f$ of the curve for pure alginate, where the fraction f denotes the assumed mineral content. For cases where there was more than one mineral phase the relative amount of the mineral, as found with Rietveld analysis, was used:

$$\Delta m(T) = f_H \Delta m_H(T) + f_B \Delta m_B(T) + (1 - f_H - f_B) \Delta m_{\text{Alg}}(T) \quad (3)$$

where $\Delta m_H(T)$ and $\Delta m_B(T)$ are the mass loss curve for pure HAp and brushite mineral phases, $\Delta m_{Alg}(T)$ is the mass loss curve for the alginate gel, and f_H and f_B are the fractions of HAp and brushite. The total mineral fraction ($f_H + f_B$) was then fitted in order for the modelled TGA curves to match the experimental data at at 1000 °C. An example of this can be seen in figure S1 in the supplementary information (stacks.iop.org/BMM/11/015013/mmedia). The error was calculated based on the control samples.

Attenuated total reflection Fourier transform infrared (ATR-FTIR) spectroscopy (Nicolet 8700 ATR-FTIR spectrometer, ThermoFisher Scientific, USA) was performed in the range of 550–4000 cm^{-1} at room temperature. An average of 32 scans was taken.

2.7. Cell experiments

Murine calvarial pre-osteoblast cells, MC3T3-E1 subclone 4 (ATCC® CRL-2593™), were cultured to 80% confluency in α -MEM supplemented with 1 $\mu\text{g ml}^{-1}$ gentamycin, 2 mM glutamine and 10% fetal calf serum, before trypsinising and mixing with alginate at a final concentration of 1×10^6 cells ml^{-1} . 300 mM PO_4 and 1 wt% brushite seeds were added to the alginate and 0.9% saline was added to give a final alginate concentration of 1.8 wt%. Alginate was also prepared in the same way without phosphate solution or brushite seeds. Microbeads containing cells were produced by electrostatic extrusion, as described previously [43]. The gelling solution used either 300 mM CaCl_2 or 1 M CaCl_2 containing 0.9% NaCl and was adjusted to pH 5 with 50 mM or 100 mM NaAc, respectively, or 50 mM CaCl_2 for non-mineralised control samples containing no phosphate or brushite seeds. 10 ml of alginate microbeads were left in the gelling solution for 10 min prior to washing with PBS and then culture media, and were then suspended in 10 ml of culture media and placed in an incubator. To assess the cell viability post-encapsulation a combination of a calcein-AM / ethidium homodimer-1 assay (LIVE/DEAD® Viability/Cytotoxicity Kit, L-3224, Molecular Probes®) and an AlamarBlue® viability assay (DAL1100, Molecular Probes®) were used. This combination of assays was used because of difficulties in accurately counting the cells stained using the LIVE/DEAD assay in the mineralised samples, which were much more optically dense than the non-mineralised controls. The AlamarBlue assay relies on optical measurements of the incubating media and is therefore not influenced by the optical properties of the samples. Viability was monitored at 1, 3, 10 and 15 d post-encapsulation on 6 repeat samples of known mass (between 0.4–0.6 g). At each point in time the live/dead cell count in the non-mineralised control samples was taken and AlamarBlue reduction was measured for all the samples (optical absorption at 570 and 590 nm, Perkin Elmer Victor 3). Comparing the results obtained by the AlamarBlue reduction assay allowed the % viability of the experimental samples to be normalised to the viability

of the non-mineralised control samples measured by the live/dead assay. The viability of the control sample was normalised with respect to the total number of encapsulated cells at the start of the experiment.

3. Results and discussion

3.1. Investigating parameters for CaP precipitation within alginate microbeads

The alginate/CaP composite beads were prepared by the counter diffusion method, as described in section 2.3. This arrangement created a highly dynamic system in which the phosphate ions diffused out of the bead, Ca^{2+} diffused into the bead, and gelling of the alginate and precipitation of CaP happened simultaneously. Formation of the mineral consumed phosphate ions, which lowered the pH locally in the hydrogel, as can be seen from equations (1) and (2). As a result, a local pH-gradient within the alginate beads was formed, and the pH in the gelling bath decreased over time, see figure 1. Both the gelling and the mineral precipitation processes consumed calcium ions.

In the first instance, we investigated an approach to produce alginate/brushite composites similar to that proposed by Amer *et al* [32], although with a reversed Ca/P ratio and a smaller bead size. The reversed Ca/P ratio was needed to form stable alginate gels [43]. This is due to the fact that the affinity between phosphate ions and calcium ions is greater than that between alginate and calcium ions. Consequently, if the calcium concentration in the gelling bath is too low, the available Ca-ions are consumed by the forming mineral phase and a stable alginate gel is not formed.

Surprisingly, no evidence of monetite or brushite was found within the hydrogel network. Contrary to their observations, the mineral phase within the beads produced in this study was poorly crystalline HAp, as seen in the lower spectrum of figure 2. An optical image of a representative sample can be seen in figure 3(a). It was also observed that some of the phosphate precursor diffused out of the beads and formed brushite-precipitates in the gelling bath. It is not only the Ca/P ratio that plays a role in the formation of CaP-precipitates; the pH is a determining factor for the nucleation of the different phases [24]. Unfortunately, no information about pH is given in the work of Amer *et al*. In this work, the pH in the gelling bath was observed to change from an initial value of pH 7 to as low as pH 3 during bead formation. This large drop in pH can also contribute to destabilising the gel. The pK_a of alginate ranges from 3.4 to 4.4 depending on the type of alginate and the conditions [45]. At such a low pH the alginate can begin to lose its charge and hence affinity for Ca^{2+} . This effect in combination with the consumption of Ca^{2+} due to mineral formation can lead to destabilisation of the gel bead, seen as wrinkles in figure 3(b). Similar observations have been reported previously, although the charge neutralisation was then due to an oppositely charged polymer, not pH [46].

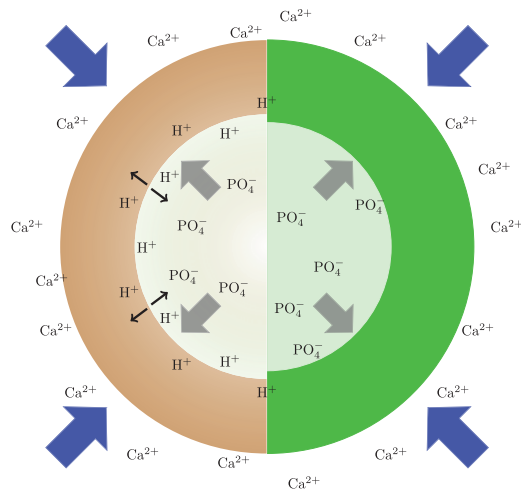


Figure 1. A schematic diagram illustrating the gelling and mineralising system. After the alginate drop has entered the gelling bath, Ca^{2+} diffuses inwards (blue arrows), the phosphate ions (PO_4^-) diffuse outwards (grey arrows), gelling and mineralising occurs at the front of the Ca^{2+} diffusion illustrated by a colour difference in the figure. On the right, the green colour indicates gelled alginate. On the left, the brown colour illustrates mineral formation and the associated local release of H^+ , their diffusion being indicated by black arrows. The mineral front trails slightly behind the gelling front.

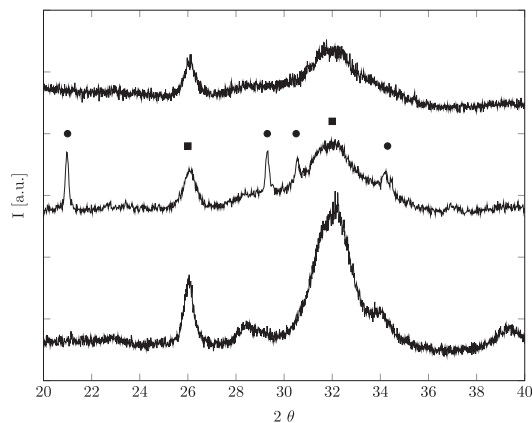
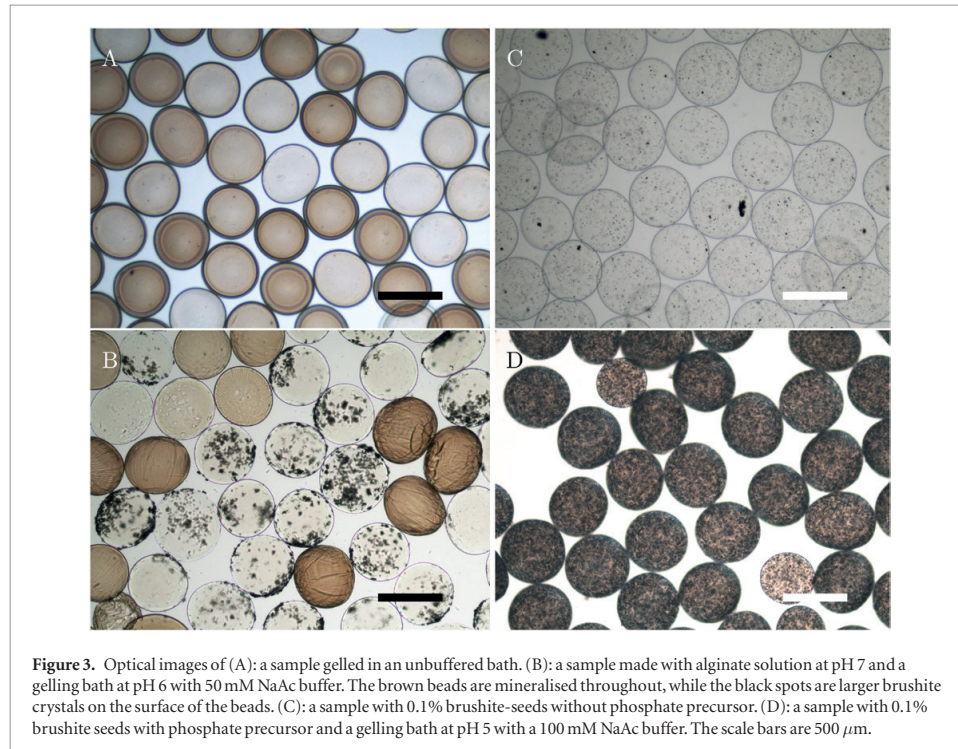


Figure 2. XRD-spectra for samples made with 300 mM phosphate in the alginate solution and 1 M calcium chloride in the gelling bath. Bottom: no buffer. Middle: a representative sample from the pH-study with a 50 mM NaAc buffer. Top: a sample with a 500 mM NaAc buffer. ● denotes brushite, ■ denotes HAp.

In order to investigate the role of pH on both the nucleation and growth of different CaP crystal phases, a series of experiments was performed where the initial pH in both the alginate solution and the gelling bath was systematically varied between pH 5 and pH 7 (a total of nine combinations) by the addition of a buffer (see Materials and methods). For a sample formed using a 50 mM buffer, upon inspection with optical microscopy (figure 3(b)), it was clear that the mineralisation was inhomogeneous in the sense that individual beads were mineralised differently. This sample was representative for most of the experiments. Note that this buffer concentration was not sufficient to

keep the pH stable during bead formation. This time-dependent change in the pH-value was believed to be the cause of the inhomogeneity observed in figure 3. The XRD-results showed that the mineral formed was, in most cases, not pure phase, but a mixture of brushite and HAp, as can be seen in the top spectrum of figure 2, and in some cases minor amounts of OCP. The estimated amount of mineral for the different samples varied between $2\text{--}49 \pm 3$ weight percent of dry mass, corresponding to $0.1\text{--}1.8 \pm 0.2$ weight percent mineral content in the hydrated gel.

The buffer strength was increased to 100 and 500 mM in an attempt to stabilise the pH at pH 5. In



both cases the change in pH was lower, as expected, although these experiments resulted in phase pure HAp within the alginate composite as can be seen in figure 2 for a sample with a 500 mM buffer. A possible explanation for this is that the ideal pH for the formation of brushite is somewhere below pH 5, although if the pH within the microbead is too low, the phosphate precursor might diffuse out of the alginate network before any mineral is formed. Hence, at no buffering, HAp is formed initially and the pH drops quickly to a value where no new crystals are nucleated. For strong buffering the pH does not drop into the region where brushite formation is favoured. A lower concentration of buffer (50 mM) allowed for the formation of some brushite, but the process was poorly controlled. For further experiments an initial pH 5 in the gelling bath was chosen as a compromise between brushite formation and cell survival. The buffer concentration was also increased to 100 mM in order to ensure more stable conditions over time in the gelling bath.

The variation in mineral amount and the occurrence of several phases indicated a complex crystallisation process within the alginate microbeads, sensitive to the local supersaturation, pH, precursor concentration and precursor ratios, all of which changed during bead formation. A lack of control over the process was identified, as the resulting mineral phase and amount varied between experiments performed under the same conditions. However, a clear trend from these experiments was that a lower pH in the alginate solution led to a lower amount of mineral within the hydrogel beads,

regardless of the initial pH in the gelling bath. A possible explanation for this is that the higher local pH within the gel network immediately after the droplet entered the gelling bath affected the local supersaturation and allowed for faster nucleation of the mineral. In cases where the initial pH within the beads was lower, more of the phosphate precursor diffused out into the gelling bath before precipitation occurred. The high initial pH is incompatible with the formation of brushite, at least in a controlled manner. To overcome this, brushite seed crystals were incorporated in the alginate solution in order to promote the early growth of brushite and to gain control over which phases nucleated in the sample.

3.2. Control of brushite formation within an alginate matrix using seed crystals

To promote the growth of brushite within the alginate network, brushite seeds were introduced into the alginate solution at three different concentrations: 0.1, 1 and 5 weight percent (hereby referred to as low, medium and high concentration of seeds). The seed crystals had a size range of approximately 30 μm , measured by a Coulter counter. The dried seeds were ground using a mortar and pestle prior to mixing with the alginate solution to distribute the seeds evenly and to avoid clogging the needle. The phase purity of the seeds was verified with XRD. The beads were then made with alginate solutions containing seeds and phosphate precursor. The pH of the gelling bath was kept at pH 5 with a 100 mM sodium acetate buffer and contained 1 M CaCl_2 and 0.9% NaCl.

Table 1. The results for seeded beads gelled in 1 M CaCl₂, 0.9 wt% NaCl, 100 mM NaAc.

Seed conc.	PO ₄ mM	Final pH	Dry mass %	Wet mass %	Brushite %
0.1%	300	4.88	71 ± 3	4.5 ± 0.6	95
0.1%	0	5.00	0 ± 3	0.0 ± 0.1	100
1%	300	4.85	79 ± 3	6.9 ± 1.2	99
1%	0	5.00	32 ± 3	0.8 ± 0.2	100
5%	300	4.73	85 ± 3	10.6 ± 2.5	98
5%	0	5.00	72 ± 3	4.7 ± 0.5	100

Note: The mass percentage refers to the mineral content, while the last column refers to the brushite percentage of this mineral.

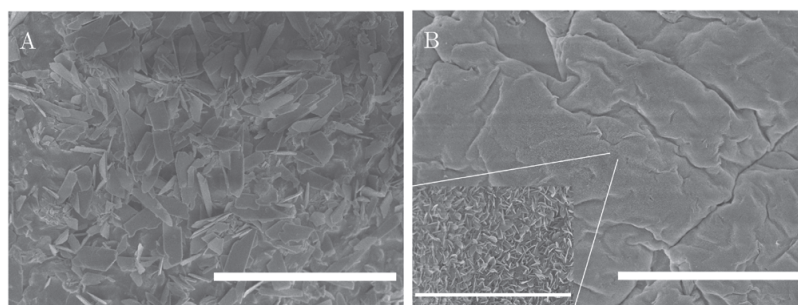


Figure 4. SEM micrograph of the surface an alginate microbead made with medium seed concentration and phosphate precursor. (A): before and (B): after 168 h in SBF. The scale bars are 30 μm and 2 μm for the inset.

Table 1 summarises the results obtained for the seeded experiments in the conditions described above. All the samples made with a phosphate precursor and brushite seeds contained close to pure phase brushite with 71 ± 3 to $86 \pm 3\%$ mineral amount (dry mass) corresponding to 4.5 ± 0.6 to $10.6 \pm 2.5\%$ wet mass. Figures 3(c) and (d) show optical images of low concentration seeded beads with and without a phosphate precursor. Comparing figures 3(a) and (b) to figure 3(d), the mineralisation of the beads was clearly more homogeneous when seed crystals were incorporated in the alginate solution. As can be seen from table 1, there was an increase in mineral content from the seeded control sample without a phosphate precursor to the beads with seeds and a phosphate precursor. Calculations based on the TGA-data indicated that similar amounts of new mineral were formed in all the samples. This increase can either arise from the growth of the seeds, the nucleation of new crystals or a combination of these.

Optical microscopy indicated the formation of new mineral crystals, as can be seen when comparing figures 3(c)–(d). This was confirmed by SEM images of the surface and cross-sections. Figure 4(a) shows the surface of a medium concentration seeded bead. A large number of crystals can be observed on the surface which were not observed for beads with brushite seeds, but without a phosphate precursor (figure S2 supplementary information (stacks.iop.org/BMM/11/015013/mmedia)). The SEM images from the cross-section of a low concentration seeded bead (figure 5) clearly show mineral crystals (white arrows) situated within the alginate network. These are much

smaller in size than the seed crystals, which suggests that they were nucleated during bead fabrication.

Although the mineralisation was homogeneous between the beads, the mineral distribution inside the alginate network was not homogeneous. The mineral formed a denser shell on the outside, and the beads appeared less mineralised towards the centre. This was as expected from previous work with the counter-diffusion method at high supersaturation [14]. The difference in mineral content can be seen in figure 5, where images from the centre and the edge of a cross-section from a bead are shown. There is also an image (figure 5(c)) of a seed crystal showing the difference in size between the seeded crystals and nucleated crystals. Note the difference in size of the seed crystal and surface crystals compared to the crystals within the network (figure 4(a) versus figure 5(a)). The smaller crystals within the network suggested a different growth rate than for the crystals on the surface.

To assess the quality of the XRD analysis, control experiments were performed. Three samples of 33.3% brushite and 66.7% HAp were made individually and characterised. Rietveld analysis resulted in $38.8 \pm 0.7\%$ brushite. For a series of six mixtures ranging from 0 to 100% brushite, the analysis consistently overestimated the amount of brushite by 3.2 ± 2.4 percentage points. These results indicate that the analysis had good precision, albeit with a systematic overestimation. One should note a large increase in the brushite signal between the control and 0 h sample in the XRD spectra shown in figure 6. The control sample contained only seeds (0.1%) and no mineral precursor while the 0 h

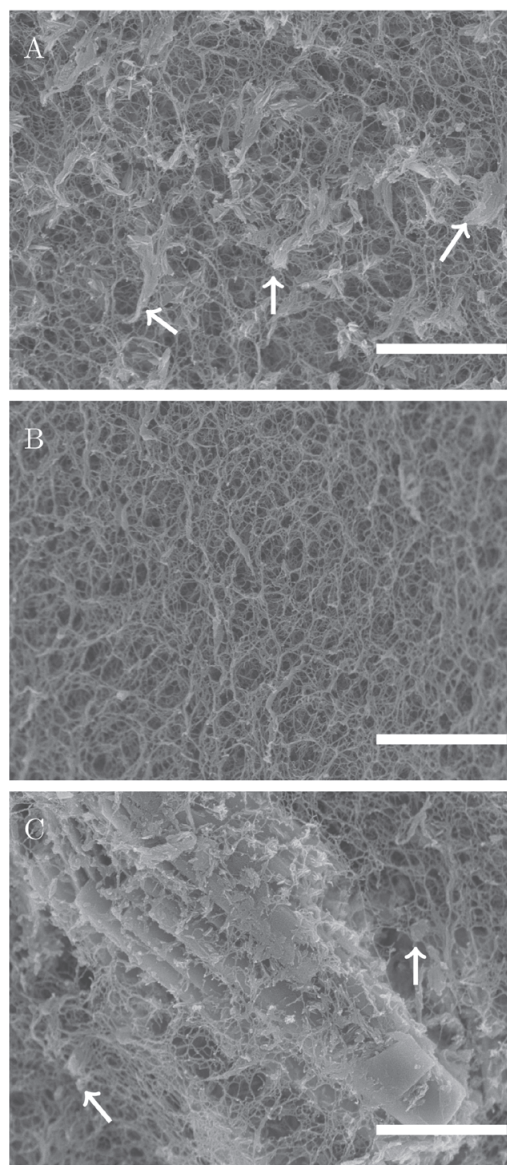
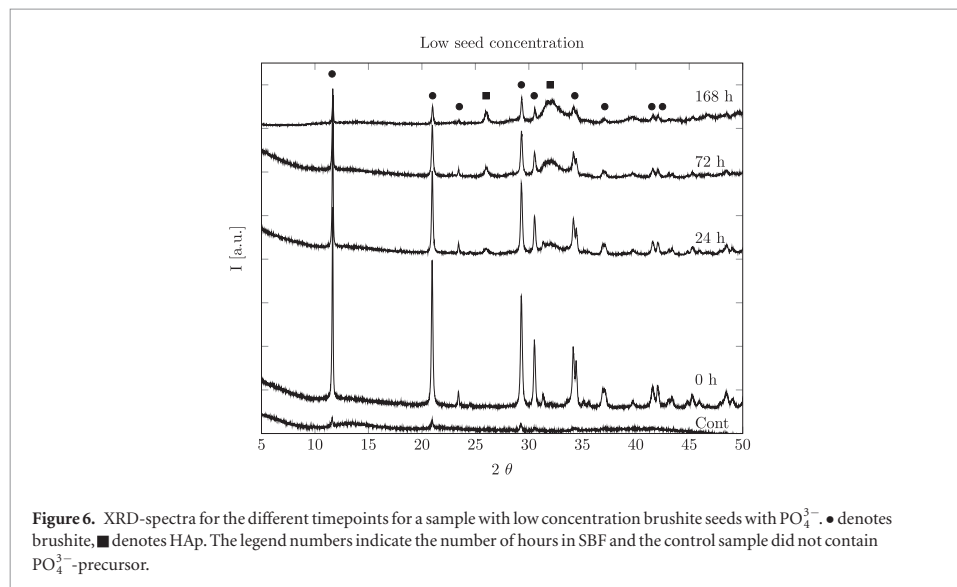


Figure 5. SEM micrographs of the cross-section of a low concentration seeded bead. (A): mineralised network in the outer region, (B): less mineralised network towards the centre. (C): the surroundings of a brushite seed. The white arrows indicate the selected mineral crystals. The scalebar is 1 μm .

sample was mineralised with 300 mM phosphate. There was a large increase in the brushite signal, indicating growth or the formation of new brushite crystals within the sample (also seen in figure 3(d)), at the same time no peaks associated with the HAp phase were present. These peaks appeared only after storage. From the control samples of pure HAp and brushite crystals mixed at a known ratio, the HAp peaks were easily detectable in a mix with 20% HAp and 80% brushite (data not shown). This indicates that a minimal amount HAp was formed initially.

For TGA-modelling, low, medium and high concentrations of seeds corresponding to dry mass percent of 5.3, 35.7 and 73.5, assuming only alginate and CaP remains after drying, were introduced into an alginate solution without phosphate precursor. The TGA of these samples resulted in a calculated dry mass percent of 0 ± 3 , 32 ± 3 and 72 ± 3 . The expected ideal values are outside the uncertainties of the calculated values for the lower seed concentrations, although they show a similar increase in mass as would be expected, suggesting that the method is reliable although somewhat inaccurate.



For the pure alginate control there was a pronounced weight loss from 650–800 °C related to the decomposition of calcium carbonate into calcium oxide. This behaviour was not observed when the phosphate mineral was precipitated during gelling (see figure S1 and a short discussion given in the supplementary Information (stacks.iop.org/BMM/11/015013/mmedia)). Due to this change in decomposition behaviour and the overestimation of brushite from the Rietveld analysis, the TGA model overestimated the mineral content by about five percentage points dry mass for heavily mineralised samples. The values presented in figure 7 are midpoints between the original model and a model with 3% less brushite and five percentage points less estimated dry mass, with error bars reaching the two extremes.

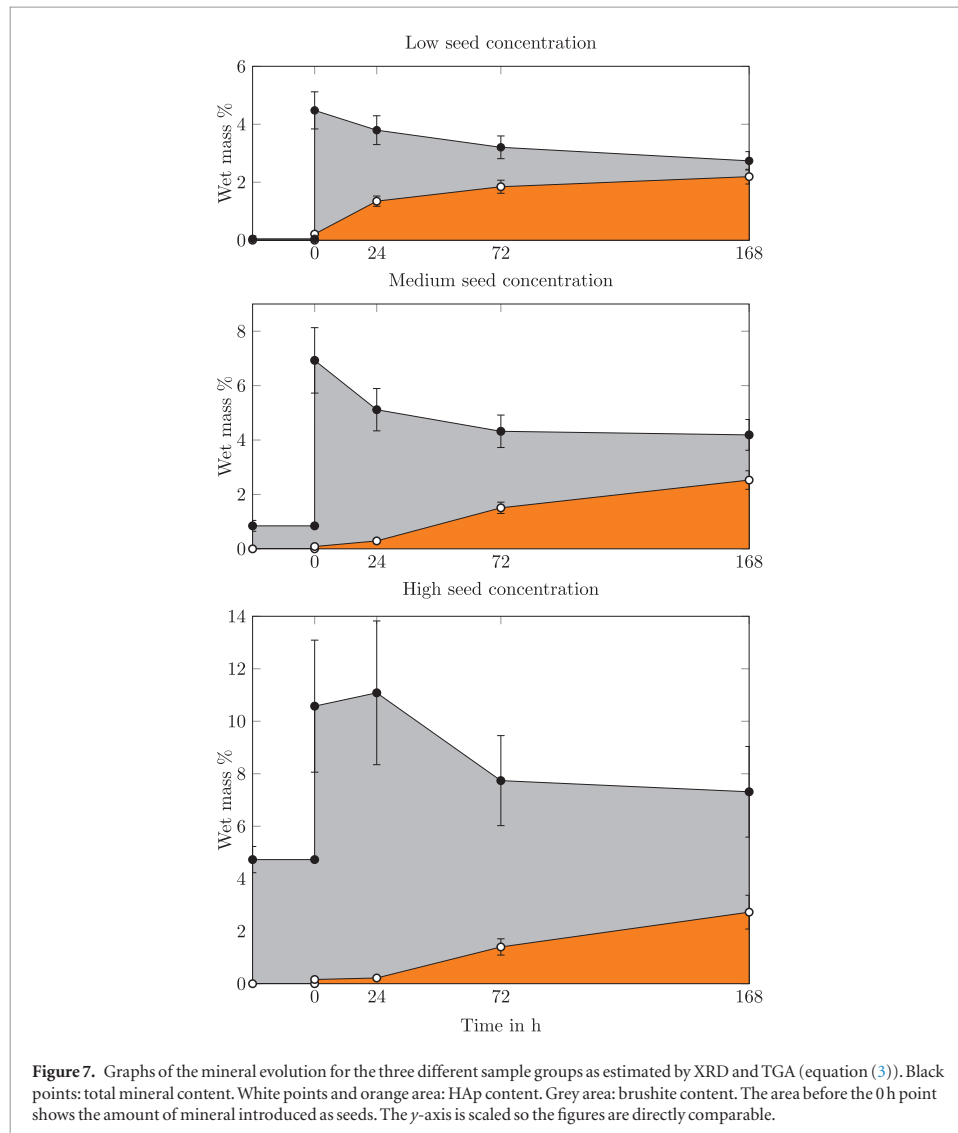
The seeds introduced into the alginate solution affected the crystallisation conditions for the whole bead, not just in the immediate proximity of the seeds. As can be seen from figure 5, new crystals of brushite were nucleated within the alginate network. This could either result from a change in the conditions of the alginate solution, where a combination of pH and supersaturation favoured the nucleation of brushite or it may have been a secondary nucleation mechanism [47]. Nucleation occurs much more readily when solute crystals are already present in the medium due to a lowered energy barrier, where parent crystals act as catalysts for nucleation [48].

3.3. Bioactivity of alginate composites in SBF

In order to evaluate the potential bioactivity of these CaP mineral–alginate composite materials, the samples were incubated in SBF for 24, 72 and 168 h before they were characterised. Figure 6 shows the XRD results for the low seed concentration sample. The results clearly show a gradual increase of HAp and decrease of the

brushite signal, which was observed for all the different seed concentrations. This data is summarised in figure 7, where a clear transformation of initial brushite into HAp is observed over time. An initial decrease in the total mineral content can also be seen. The image in figure 4(a) was taken before incubation in SBF, and the one in (b) was taken after 168 h incubation in SBF. For the composite containing a phosphate precursor there was, before incubation, a large number of brushite crystals on the surface. These appear to have dissolved and reprecipitated as smaller HAp crystals, seen in the inset in figure 4(b). This dissolution is presumably the cause of the decrease in the overall mineral content. These results also show that the lowest seed concentration transformed into HAp earlier than the other samples. As controls, alginate beads with seeds, but no phosphate precursor and alginate beads without seeds or phosphate precursor were also kept in SBF for 168 h. The seeded control showed no conversion into HAp (see figure S2 in supplementary information (stacks.iop.org/BMM/11/015013/mmedia)), while the pure alginate control showed no mineral formation.

This study was performed under static conditions and was therefore not a prediction of actual *in vivo* behaviour [49]. This was done in order to study the transformation behaviour of the mineral in a solution supersaturated with respect to HAp. The dissolution of brushite and the formation of HAp occurred under the same initial conditions in the different sample groups. Comparing these results with the work of Miller *et al* [50], who performed a study of brushite transformation in four different SBF solutions, including a TRIS-buffered solution similar to the one used in this study, the behaviour is similar except for two main points. In this study, the initial brushite was not completely dissolved or transformed within 168 h. That is probably due to the fact that static conditions were used. A more



interesting observation is that no OCP was observed in this work. This can be seen in figure 6, where two distinct peaks of OCP (9.45° and 9.77°) are absent.

FTIR analysis, as shown in figure 8, confirmed the formation of brushite for all the samples seeded with brushite, with strong absorbance bands at 986 and 1005 cm^{-1} corresponding to the ν_2 P–O symmetrical stretching mode and 1059 , 1125 and 1137 cm^{-1} corresponding to the ν_6 triply degenerated P–O stretching mode [51]. Changes in the FTIR spectrum occurred for all the samples exposed to SBF, which indicated a change from HPO_4^{2-} to PO_4^{3-} . This can be seen in the disappearance of the ν_3 P–O(H) stretching mode at 875 cm^{-1} and the appearance of a strong adsorption at 1025 cm^{-1} . Changes also occurred in the ν_4 O–P–O(H) bending mode, which is located at 578 cm^{-1} for brushite and 602 cm^{-1} for HAp [51, 52]. These changes

occurred more rapidly for the samples formed with less initial seed material. After 168 h incubation, low concentration seeded composites had almost completely lost the vibrational modes associated with brushite and the resulting spectra resembled poorly crystalline HA; by comparison, the high concentration seeded samples, however, had only partially converted by this time.

The FTIR results largely reflect what was found by XRD analysis, as shown in figure 6, although the loss of intensity of the brushite signal appears earlier for FTIR. This could suggest a loss of protons and the formation of an intermediate amorphous phase, before reprecipitation to HAp. As XRD techniques rely on crystalline samples for a signal, amorphous phases would not be detected by XRD.

The accelerated transformation of brushite into HAp at a decreased seed concentration may derive from

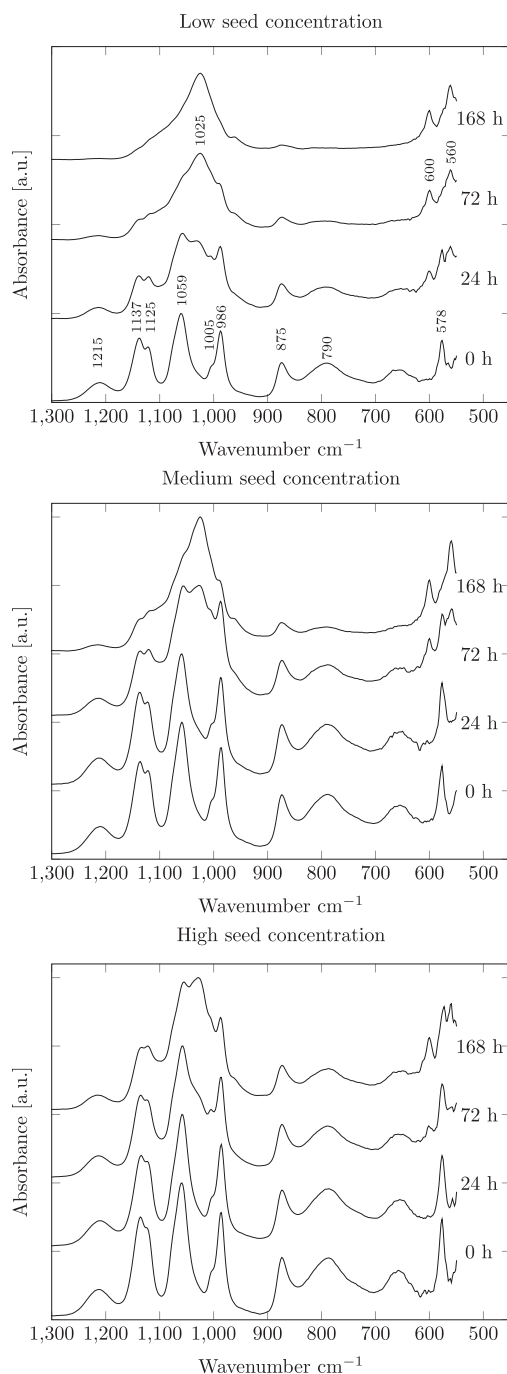
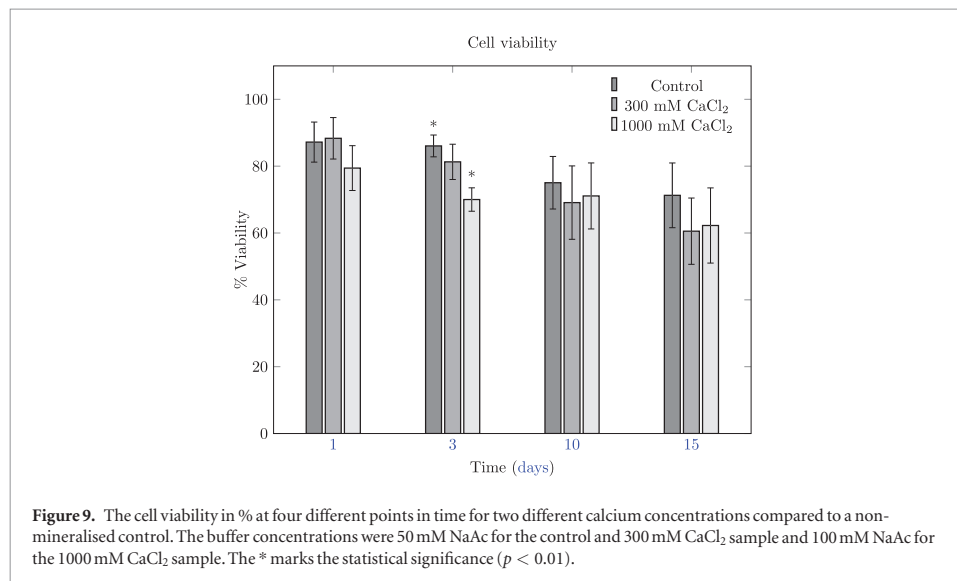


Figure 8. FTIR-spectra of the samples with 0.1%, 1% and 5% seed concentrations following the indicated periods of incubation in SBE.

the smaller size of the newly formed brushite crystals. For higher seed concentrations, a higher amount of the initial phosphate will be consumed in the crystal growth of these seeds. In the cases of higher seed loading, the consumption of ions by growth would likely have caused

a decrease in the number of newly formed particles [48]. The smaller crystals had a higher surface area and therefore dissolved more readily. The increased bioactivity of smaller crystals is further corroborated by a control sample in which beads containing a medium seed



concentration without a phosphate precursor showed no conversion into HAp after 168 h in SBF solution.

3.4. Cell encapsulation and survival

Alginate hydrogels provide a good matrix for cell encapsulation; we have previously shown that cells can also be encapsulated and survive in alginate microbeads mineralised with HAp [53,54]. Gryshkov *et al* have also shown that high voltage does not affect cell viability [55]. Previously, the mineralised alginate was synthesised under mild conditions of mineral precursor concentrations and near physiological pH. Here we used more acidic conditions to achieve the desired brushite mineral phase. Since cells cannot survive such a low pH, we tested the viability of pre-osteoblast cells post-encapsulation. Cells were encapsulated in alginate containing 1% brushite seeds, 300 mM PO₄ and gelled in 1 M CaCl₂ and 100 mM NaAc at pH 5 or 300 mM CaCl₂ and 50 mM NaAc and the viability of encapsulated cells was compared to non-mineralised control beads made with pure alginate and gelled in 50 mM CaCl₂ (see figure 9). Surprisingly there was little difference in cell viability 24 h after encapsulation between the controls and the mineralised beads gelled in 300 mM CaCl₂ ($87.2 \pm 6.0\%$ versus $88.3 \pm 6.2\%$). However, a lower viability for the mineralised samples gelled in 1 M CaCl₂ was recorded ($79.4 \pm 6.7\%$). The cell viability reduced gradually over the 15 d of the culture period for all the samples. After 15 d of culture the cell viability was $60.5 \pm 9.9\%$ and $62.2 \pm 11.2\%$ for the mineralised samples and $71.2 \pm 9.7\%$ for the non-mineralised controls. This gradual reduction was probably due to natural cell death without renewal since the cells appeared to not divide within the alginate matrix as very similar numbers of cells were observed within each bead at each point in time. Since the rate of cell death was very similar for all the samples it would

appear that the mineral made in either condition had little influence on cell viability.

4. Conclusions

Building upon our previous work regarding the counter-diffusion synthesis of alginate-calcium phosphate (HAp) composite materials, here we have formulated robust methods to control the phase purity and amount of brushite formed within alginate hydrogels. These new materials may have a significant advantage over HAp containing alginates as bone tissue engineering constructs, since brushite is metastable under physiological conditions and will convert to HAp, as we have demonstrated in simulated body fluid, and may act as a reservoir for essential ions for bone remodelling. Reliable nucleation of the preferred brushite phase inside the alginate network proved more complicated than in aqueous solution in the absence of alginate, where control over the initial parameters of pH and stoichiometry was enough to predict the resulting phase. The incorporation of brushite seed crystals into the alginate solution prior to gelation resulted in improved control and reproducibility of the mineral phase and by adjusting the number of seeds and amount of precursor concentration, the amount of mineral could also be tuned. The bioactivity of the precipitated mineral was shown to be higher than that of mixtures of preformed mineral incorporated in an alginate matrix, likely due to the smaller crystal size of the mineral precipitated within the alginate matrix. Furthermore, we found that our synthesis method was well tolerated by pre-osteoblast cells, and cell viability was similar to the non-mineralised control samples post-encapsulation and survived well over a period of 15 d. This is significant for the intended use of these materials as

support structures for cells in the context of bone tissue regeneration.

Acknowledgments

We acknowledge the Research Council of Norway for financial support (FRINATEK project 214607). We thank Dr O Sigurjonsson, Reykjavik University, Iceland for providing us with the cell line used in this study. We also thank Dr B L Strand for fruitful advice regarding alginate.

References

- [1] Hollister S J 2009 *Adv. Mater.* **21** 3330–42
- [2] Rokstad A M A, Lacik I, de Vos P and Strand B L 2014 *Adv. Drug Deliv. Rev.* **67–8** 111–30
- [3] Place E S, Evans N D and Stevens M M 2009 *Nat. Mater.* **8** 457–70
- [4] Hoffman A S 2002 *Adv. Drug Deliv. Rev.* **54** 3–12
- [5] Dragan E S 2014 *Chem. Eng. J.* **243** 572–90
- [6] Amini A R, Laurencin C T and Nukavarapu S P 2012 *Crit. Rev. Biomed. Eng.* **40** 363–408
- [7] Drury J L and Mooney D J 2003 *Biomaterials* **24** 4337–51
- [8] Kolambkar Y M, Dupont K M, Boerckel J D, Huebsch N, Mooney D J, Hutmacher D W and Guldberg R E 2011 *Biomaterials* **32** 65–74
- [9] Cohen J 1998 *J. Bone Joint Surg. Am.* **80** 1554
- [10] Rho J Y, Kuhn-Spearing L and Zioupos P 1998 *Med. Eng. Phys.* **20** 92–102
- [11] Bernhardt A, Despang F, Lode A, Demmler A, Hanke T and Gelinsky M 2009 *J. Tissue Eng. Regen. Med.* **3** 54–62
- [12] Yokoi T, Kawashita M, Kikuta K and Ohtsuki C 2010 *J. Cryst. Growth* **312** 2376–82
- [13] Rajkumar M, Meenakshisundaram N and Rajendran V 2011 *Mater. Charact.* **62** 469–79
- [14] Xie M, Olderooy M O, Zhang Z, Andreassen J P, Strand B L and Sikorski P 2012 *RSC Adv.* **2** 1457
- [15] Li Z, Su Y, Xie B, Wang H, Wen T, He C, Shen H, Wu D and Wang D 2013 *J. Mater. Chem. B* **1** 1755
- [16] Luo Y, Lode A, Sonntag F, Nies B and Gelinsky M 2013 *J. Mater. Chem. B* **1** 4088
- [17] Zhu C, Bao G and Wang N 2000 *Annu. Rev. Biomed. Eng.* **2** 189–226
- [18] Suárez-González D, Barnhart K, Saito E, Vanderby R, Hollister S J and Murphy W L 2010 *J. Biomed. Mater. Res. A* **95** 222–34
- [19] Lin H R and Yeh Y J 2004 *J. Biomed. Mater. Res. B* **71** 52–65
- [20] Albrektsson T and Johansson C 2001 *Eur. Spine J.* **10** S96–101
- [21] Johansson M S and Nancollas G H 1992 *Crit. Rev. Oral Biol. Med.* **3** 61–82 (PMID: 1730071)
- [22] Mirtchi A, Lemaître J and Munting E 1989 *Biomaterials* **10** 634–8
- [23] Tamimi F, Sheikh Z and Barralet J 2012 *Acta Biomater.* **8** 474–87
- [24] Elliott J 1994 *Structure and Chemistry of the Apatites and Other Calcium Orthophosphates* (Amsterdam: Elsevier) (doi: 10.1016/B978-0-444-81582-8.50001-8)
- [25] Apelt D, Theiss F, El-Warrak A, Zlinszky K, Bettschart-Wolfisberger R, Böhner M, Matter S, Auer J and von Rechenberg B 2004 *Biomaterials* **25** 1439–51
- [26] Klammert U, Ignatius A, Wolfram U, Reuther T and Gbureck U 2011 *Acta Biomater.* **7** 3469–75
- [27] Kanter B, Geffers M, Ignatius A and Gbureck U 2014 *Acta Biomater.* **10** 3279–87
- [28] Habibovic P, Gbureck U, Doillon C, Bassett D, Vanblitterswijk C and Barralet J 2008 *Biomaterials* **29** 944–53
- [29] Gbureck U, Hölzel T, Klammert U, Würzler K, Müller F A and Barralet J E 2007 *Adv. Funct. Mater.* **17** 3940–5
- [30] Nanzyo M, Shibata Y and Wada N 2002 *Soil Sci. Plant Nutrition* **48** 847–53
- [31] Koburger S, Bannerman A, Grover L M, Müller F A, Bowen J and Paxton J Z 2014 *Biomater. Sci.* **2** 41
- [32] Amer W, Abdelouahdi K, Ramanarivo H R, Fihri A, El Achaby M, Zahouily M, Barakat A, Djessas K, Clark J and Solhy A 2014 *Mater. Sci. Eng. C* **35** 341–6
- [33] Kelton K 1991 *Solid State Phys.* **45** 75–177
- [34] Kashchiev D and van Rosmalen G M 2003 *Cryst. Res. Technol.* **38** 555–74
- [35] Boistelle R and Lopez-Valero I 1990 *J. Cryst. Growth* **102** 609–17
- [36] Wuthier R E, Rice I G S, Wallace J E B, Weaver R L, Legeros R Z and Eanes E D 1985 *Calcif. Tissue Int.* **37** 401–10
- [37] Abbona F, Madsen H and Boistelle R 1986 *J. Cryst. Growth* **74** 581–90
- [38] Abbona F, Christensson F, Angela M and Madsen H 1993 *J. Cryst. Growth* **131** 331–46
- [39] Kokubo T and Takadama H 2006 *Biomaterials* **27** 2907–15
- [40] Böhner M and Lemaître J 2009 *Biomaterials* **30** 2175–9
- [41] Rohanová D, Boccaccini A R, Yunus D M, Horkavcová D, Bezovská I and Helebrant A 2011 *Acta Biomater.* **7** 2623–30
- [42] Mandel S and Tas A C 2010 *Mater. Sci. Eng. C* **30** 245–54
- [43] Xie M, Olderooy M O, Andreassen J P, Selbach S M, Strand B L and Sikorski P 2010 *Acta Biomater.* **6** 3665–75
- [44] Drager K I, Østgaard K and Smidsrød O 1989 *Appl. Microbiology Biotechnol.* **31** 79–83
- [45] Haug A 1964 *Composition and Properties of Alginate* (Trondheim: N.T.H. Trykk)
- [46] Strand B L, Gåserød O, Kulseng B, Espevik T and Skjåk Bræk G 2002 *J. Microencap.* **19** 615–30
- [47] Garside J 1985 *Chem. Eng. Sci.* **40** 3–26
- [48] Frawley P J, Mitchell N A, O'Ciardhá C T and Hutton K W 2012 *Chem. Eng. Sci.* **75** 183–97
- [49] Rámila A and Vallet-Reg M 2001 *Biomaterials* **22** 2301–06
- [50] Miller M A, Kendall M R, Jain M K, Larson P R, Madden A S and Tas A C 2012 *J. Am. Ceram. Soc.* **95** 2178–88
- [51] Casciani F and Condrate R A 1979 *Spectrosc. Lett.* **12** 699–713
- [52] Rehman I and Bonfield W 1997 *J. Mater. Sci.: Mater. Med.* **8** 1–4
- [53] Westhrin M, Xie M, Olderooy M O, Sikorski P, Strand B L and Standal T 2015 *Plos One* **10** e0120374
- [54] Olderooy M, Xie M, Westhrin M, Andreassen J P, Zhang Z, Strand B L, Standal T and Sikorski P 2012 *Eur. Cells Mater.* **23** 53
- [55] Gryshkov O, Pogozhykh D, Zernetsch H, Hofmann N, Mueller T and Glasmacher B 2014 *Mater. Sci. Eng. C* **36** 77–83

Supplementary Information: Controlled mineralisation and recrystallisation of brushite within alginate hydrogels

Sindre H. Bjørnøy¹, David Bassett¹, Seniz Ucar², Jens-Petter Andreassen², Pawel Sikorski¹

¹ Department of Physics, Norwegian University of Science and Technology, Trondheim, Norway

² Department of Chemical Engineering, Norwegian University of Science and Technology, Norway

E-mail: pawel.sikorski@ntnu.no

TGA and XRD analysis

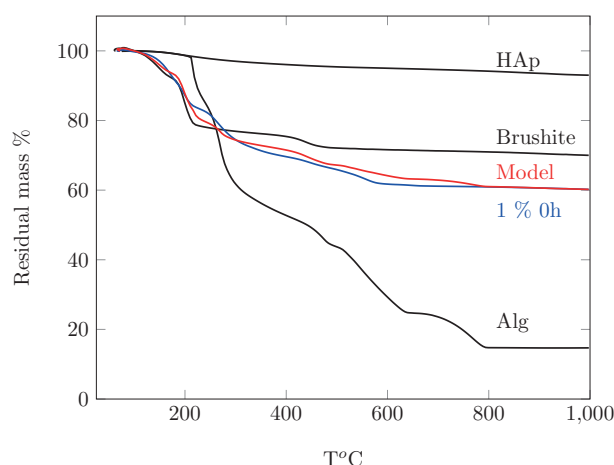


Figure S1 Illustration of the method used to determine mineral amount from TGA-data. Black curves: HAp, DCPD and alginate. Blue curve: 1 % seeds. Red curve: Model with $f_D=0.82$ and $f_H = 0$.

Figure S1 shows the principle of the method used to determine the mineral amount. The curves for control samples of pure alginate, pure brushite and pure HAp are added and fitted to the experimental curve. For samples with more than one mineral phase, the relative amount of each phase was found by Rietveld analysis. ICDD standards used for Rietveld analysis: Brushite: PDF# 04-013-3344¹ and HAp: PDF# 00-055-0592².

The reason for the discrepancy between the model and the experimental data in the range of circa 500-800°C is not known. The pure alginate sample has a pronounced weight loss from 650-800°C due to the decomposition of CaCO_3 into CaO . There are two possible explanations why this is not observed in the experiments. It could be that the presence of mineral influences the reaction where Ca reacts with the carbon from the burning alginate and prevents the

formation of CaCO_3 . Another explanation could be that the presence of mineral affects the temperature at which the CaCO_3 decomposes into CaO . Newkirk and Aliferis has shown that the temperature at which the decomposition of NaCO_3 occur can be altered due to its chemical environment.³ They observed that simply by changing the crucible material which the sample was kept in the decomposition temperature changed. Also by mixing silica grains with the NaCO_3 , the decomposition temperature was reduced and this effect was increased for smaller grains providing a large surface area. We speculate that a similar effect might be present in this case, and the mineral present in our sample provides a large surface area due to the small crystal size. As the model is based on adding a fraction of the pure alginate curve and fractions of the mineral curves, it does not take into account changes in the thermal behaviour of the different compounds. We therefore chose to fit our model to match the final weight of the experimental sample rather than minimize the discrepancy between the curves.

Bioactivity

Figure S2 shows that seeded beads without phosphate precursor did not transform after 1 week in SBF.

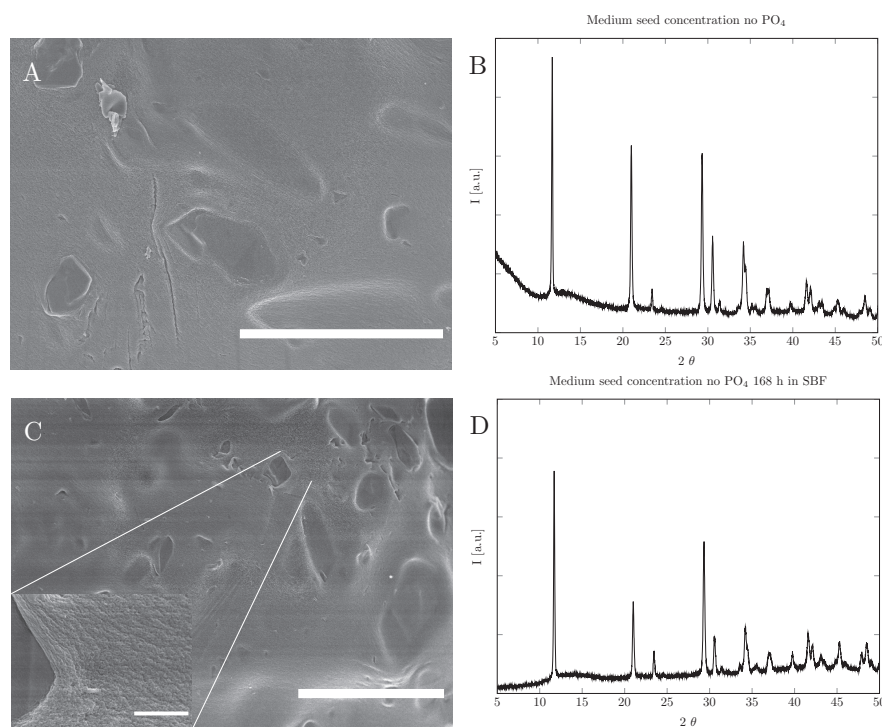


Figure S2 SEM micrograph of the surface of an alginate microbead (A) and a corresponding XRD-spectra (B) of a sample made with medium seed concentration and without phosphate precursor. C and D: data for the same samples collected after 168h incubation in SBF. No mineral formation is visible on the surface of the bead. The XRD-spectra show no indication of HAp formation. Scale bars are 30 μm and 2 μm for inset.

References

- [1] Curry N A and Jones D W 1971 *J. Chem. Soc. A Inorganic, Phys. Theor.* 3725 ISSN 0022-4944 URL <http://pubs.rsc.org/en/content/articlehtml/1971/j1/j19710003725>
- [2] Tas A C 2012 *Powder Diffr.* **16** 102–106 ISSN 0885-7156 URL http://journals.cambridge.org/abstract_S0885715600005765
- [3] Newkirk A E and Aliferis I 1958 *Analytical Chemistry* **30** 982–984 ISSN 0003-2700 URL <http://dx.doi.org/10.1021/ac60137a031>

Paper II



Contents lists available at ScienceDirect

Acta Biomaterialia

journal homepage: www.elsevier.com/locate/actabiomat

Full length article

Gelling kinetics and *in situ* mineralization of alginate hydrogels: A correlative spatiotemporal characterization toolbox



Sindre H. Bjørnøy^a, Stefan Mandaric^a, David C. Bassett^a, Andreas K.O. Åslund^a, Seniz Ucar^b, Jens-Petter Andreassen^b, Berit L. Strand^c, Pawel Sikorski^{a,*}

^a Department of Physics, NTNU, Norwegian University of Science and Technology, 7491 Trondheim, Norway

^b Department of Chemical Engineering, NTNU, Norwegian University of Science and Technology, 7491 Trondheim, Norway

^c Department of Biotechnology, NTNU, Norwegian University of Science and Technology, 7491 Trondheim, Norway

ARTICLE INFO

Article history:

Received 25 May 2016

Received in revised form 4 July 2016

Accepted 27 July 2016

Available online 3 August 2016

Keywords:

Alginate

Hydrogel

Modeling

Raman spectroscopy

ABSTRACT

Due to their large water content and structural similarities to the extracellular matrix, hydrogels are an attractive class of material in the tissue engineering field. Polymers capable of ionotropic gelation are of special interest due to their ability to form gels at mild conditions. In this study we have developed an experimental toolbox to measure the gelling kinetics of alginate upon crosslinking with calcium ions. A reaction–diffusion model for gelation has been used to describe the diffusion of calcium within the hydrogel and was shown to match experimental observations well. In particular, a single set of parameters was able to predict gelation kinetics over a wide range of gelling ion concentrations. The developed model was used to predict the gelling time for a number of geometries, including microspheres typically used for cell encapsulation. We also demonstrate that this toolbox can be used to spatiotemporally investigate the formation and evolution of mineral within the hydrogel network via correlative Raman microspectroscopy, confocal laser scanning microscopy and electron microscopy.

Statement of Significance

Hydrogels show great promise in cell-based tissue engineering, however new fabrication and modification methods are needed to realize the full potential of hydrogel based materials. The inclusion of an inorganic phase is one such approach and is known to affect both cell-material interactions and mechanical properties. This article describes the development of a correlative experimental approach where gel formation and mineralization has been investigated with spatial and temporal resolution by applying Raman microspectroscopy, optical and electron microscopy and a reaction–diffusion modeling scheme. Modeling allows us to predict gelling kinetics for other geometries and sizes than those investigated experimentally. Our experimental system enables non-destructive study of composite hydrogel systems relevant for, but not limited to, applications within bone tissue engineering.

© 2016 Acta Materialia Inc. Published by Elsevier Ltd. All rights reserved.

1. Introduction

Alginates are a group of biopolymers widely used in biomedical applications and research, largely due to low immunogenicity, low toxicity and ease of forming stable hydrogels under cell compatible and near physiological conditions [1–8]. Alginate hydrogels with different physical forms, often made with encapsulated cells, have

been fabricated, including micro- and macro-scale beads, alginate fibers, films, foams and 3D gels [9–15]. Recent research areas of particular interest and innovation include a wide variety of both hard and soft tissue engineering applications as well as cell encapsulation for the treatment of diseases such as diabetes [16,17]. Chemically modified alginates are also being investigated as extracellular matrix mimics [18,19]. To be able to design and fabricate new types of hydrogel based biomaterials, including hydrogel composites, a better understanding of the gel formation process and *in situ* modification strategies is needed [20,21]. When hydrogels are formed from polymers capable of ionotropic gelation, i.e. crosslinking by exogenous inorganic ions, the gel formation is a

* Corresponding author.

E-mail addresses: sindre.bjornoy@ntnu.no (S.H. Bjørnøy), david.bassett@ntnu.no (D.C. Bassett), andreas.aslund@ntnu.no (A.K.O. Åslund), seniz.ucar@ntnu.no (S. Ucar), jens-petter.andreassen@ntnu.no (J.-P. Andreassen), berit.l.strand@ntnu.no (B.L. Strand), pawel.sikorski@ntnu.no (P. Sikorski).

<http://dx.doi.org/10.1016/j.actbio.2016.07.046>

1742-7061/© 2016 Acta Materialia Inc. Published by Elsevier Ltd. All rights reserved.

complex reaction–diffusion process, involving both transport of gelling and non-gelling ions, diffusion of the ungelled polymer and the formation of junction zones. For alginate, a polysaccharide consisting of mannuronic (M) acid and guluronic (G) acid residues, these junction zones consist of aligned polymers with repeating units of the G-monomer, termed the egg-box model [22,23]. In addition, it has been shown that MG-blocks also form stable junction zones [24]. A detailed understanding of these processes would not only allow for optimization of cell encapsulation, but also enable the formation of gels with complex geometries, such as fibers, films, microbeads and hollow spheres. In addition, if one is able to combine this knowledge with a detailed understanding of *in situ* modification methods, for example by incorporation of solid inorganic components, fibrous reinforcement or hydrogel-hydrogel composites, it would open new avenues for development of composite materials for application within tissue engineering and biomedical research and technology.

Modification of hydrogels with calcium phosphate (CaP) minerals to mimic the microenvironment of bone is one strategy to realize new classes of such composite materials [25–27]. We have focused on controlled mineralization of alginate hydrogels *in situ*, in a process which is compatible with cell encapsulation [28,29]. In such a system, CaP mineral is formed within the hydrogel network at the time of gelling. However the mineral phase undergoes several transformation and maturation steps, and both initial precipitation and subsequent storage will effect the properties of the final CaP phase. Processes such as crystal nucleation and growth within the gel network, solution mediated transformations and local changes in pH induced by gel formation and/or mineral precipitation are important [30–32]. Kinetics of alginate gelling have previously been investigated in non-mineralized systems and this knowledge has been applied to facilitate the formation of alginate structures with different geometries [33–37]. Mikkelsen and Elgsaeter developed a reaction–diffusion model which describes both gel formation kinetics, as well as the density distribution of alginate in calcium-alginate gels formed by the diffusion of gelling ions [36]. Thu et al. has estimated that the alginate gel front moves at a velocity of about $100 \mu\text{m min}^{-1}$ corresponding to $1.67 \mu\text{m s}^{-1}$ when 50 mM CaCl_2 solution was used [35]. However high spatial and temporal resolution experimental data is lacking, making progress in better understanding of the process difficult. High spatial and temporal resolution data on the gel front velocity combined with information about polymer concentration profiles, could be implemented in already existing numerical models, which in turn could be used to aid the rational design of hydrogel fabrication processes in other systems and geometries such as mineralized films, cell encapsulation matrices and microfluidic-based fabrication of alginate microbeads and fibers. Extensive knowledge of the gel system would allow for optimal process design. For example, one could maximize cell viability during cell encapsulation in microbeads, fibers or films, by finding the optimal ion concentrations and gelling times needed to make stable gels, at the same time minimizing cell exposure to potentially detrimental physicochemical conditions.

The situation is even more complex when a mineral phase, such as CaP, is precipitated within the hydrogel at the time of gelling. The process involves a complex interplay between many aspects, including fluxes of the reaction substrates and gelling ions, ion consumption due to gel formation, supersaturation controlled nucleation and growth of the mineral phase, spatial and temporal evolution of pH and transformation of the mineral phases [38]. A model experimental system in which these process could be studied *in situ*, in real time and with a range of physical methods would allow for a quantitative description of all these process. In the long run, this type of data could be used to construct complex models of the mineralization process, accounting for nucleation, growth and

transformation rates of various CaP phases. This goal is however beyond the scope of this contribution, but it remains as a future challenge.

In this work we present an experimental framework for studying the spatially and temporally resolved gelling and *in situ* mineralization of alginate/calcium phosphate composites. To this experimental framework we apply a range of characterization techniques including dark field and confocal microscopy, scanning electron microscopy, and Raman spectroscopy to investigate the kinetics of gel formation and mineralization in real time. We then describe the development of methods to study the interplay between the hydrogel and mineral phases in hitherto undescribed detail.

2. Experimental

2.1. Alginate and gelling solution

All chemical reagents were purchased from Sigma–Aldrich, Norway unless otherwise stated. De-ionized water (DIW, 10–15 MΩcm) was used in all of the experiments. Sodium alginate (*Laminaria hyperborea*, Protanal LF 200S, $M_w = 2.74 \times 10^5 \text{ g mol}^{-1}$, FMC BioPolymer AS, fraction of G-monomers: $F_G = 0.68$, $F_{GG} = 0.57$ and $F_{CM} = 0.11$) was used in the entire work, except for the alginate labeled with Fluoresceinamine (*Laminaria hyperborea*, Protanal SF60, $M_w = 2.2 \times 10^5 \text{ g mol}^{-1}$, FMC BioPolymer AS, fraction of G-monomers: $F_G = 0.67$, $F_{GG} = 0.58$, $F_{GGG} = 0.52$) The fluorescently labeled alginate was made as described by Strand et al. [39].

Stock solutions of 1 M CaCl_2 and 1 M CaCl_2 and 0.9% (w/v) NaCl (VWR) were made in DIW. Buffering was done with 25 mM 3-(N-Morpholino) propanesulfonic acid (MOPS) at pH 6.5 and 7.4 for the gelling experiments and with 50 mM Tris(hydroxymethyl) aminomethane (TRIS) and 50 mM sodium acetate (NaAc) for mineralization experiments at pH 7 and 5 respectively. Gelling experiments refer to experiments where alginate solutions without a phosphate precursor have been used. Mineralization experiments refer to experiments where alginate solutions containing a phosphate precursor have been used. In all cases, gelling solution refers to a solution containing CaCl_2 . The concentration of calcium and the pH in the gelling solution is specified where necessary.

For the gelling experiments, 2% (w/v) alginate solution was prepared by dissolving sodium alginate in DIW. For the mineralization experiments 1.8% alginate solutions containing 0.9% NaCl, with either 200 mM or 300 mM phosphate were prepared by dissolving sodium alginate and a mixture of $\text{Na}_2\text{HPO}_4 \cdot 7\text{H}_2\text{O}$ and $\text{NaH}_2\text{PO}_4 \cdot 2\text{H}_2\text{O}$ (Thermo Fisher Scientific). The ratio of the phosphate precursors were chosen to give a final pH between 5 and 7. All sodium alginate solutions were stored at 4 °C between experiments.

2.2. Alginate flow cells

In order to conduct the experiments, a simple flow cell was constructed. The flow cell consisted of an alginate droplet sandwiched between two microscope slides separated by strips of 140 μm thick double-sided tape. A 1.5 μL droplet of alginate solution was placed onto the center of the slide and covered by either a second microscope slide or a cover slip as shown in Fig. 1a. Gentle pressure was applied in order to compress the droplet into a disc. 150 μL of gelling solution was then applied into the spacing between the slides to initiate the gelling.

2.3. Dark-field microscopy

The gelling reaction was studied in an Olympus IX-70 Inverted Microscope. The objective used was Olympus UPlanFl 4x/0.13NA in

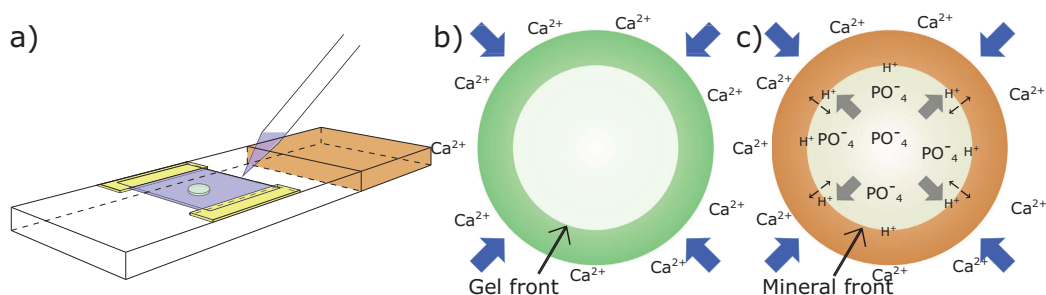


Fig. 1. (a) Illustration of the flow cell for gelling experiments. (b) and (c) Schematic cross-sections of a gelling and mineralizing hydrogel bead or disc. The blue arrows denote calcium flux, the gray arrows denote phosphate flux, and the black arrows denote H^+ flux. The solid green color represents gelled alginate, while brown color represents mineral formation. (For interpretation of the references to colour in this figure caption, the reader is referred to the web version of this article.)

combination with a Ph1 condenser annulus. This objective did not have a phase ring which lead to a non-traditional contrast mechanism provided by a mixture of phase contrast and dark-field contrast. However, the settings were chosen on purpose, as this mode provided the best contrast for observation of the moving gel front. A high speed camera (Photron SA-3) connected to the microscope side port filmed the gelling. The gel front velocity was determined from the videos using a custom developed script and MATLAB (R2014b). Briefly, the Canny edge detector operator with low threshold was used to detect the gel front, producing a binary image of all high contrast features in the image. The gel front was isolated by excluding all static features and all edges below a threshold size and was then fitted with an ellipse. The gel front radius was calculated by averaging the two ellipse axes. All samples were close to circular. The gel front position was plotted as a function of time, and the gel front velocity was found by calculating the slope of the linear region of the resulting plot.

2.4. Confocal laser scanning microscopy

The gelling of Fluoresceinamine-labeled alginate was performed in the flow cells described above and observed with a Leica TCS SP5 Confocal Laser Scanning Microscope (CLSM). A Leica HCX PL FLUOTAR 5.0x/0.15NA dry objective was used in combination with argon laser 488 nm line. The resulting time series were analyzed in MATLAB.

2.5. pH measurements with CLSM

In addition to measurements of the gel front, CLSM was also used in combination with a pH-sensitive dye to measure the local pH. Rhodamine 6 and ethylenediamine was refluxed in methanol for 6 h resulting in a pH-sensitive fluorescent molecule, named R6G-EDA, according to previous reports [40,41]. R6G-EDA was used at a concentration of 20 μ M in both the alginate- and the gelling-solutions. Sulfhorhodamine 101 (SR101), a pH-insensitive dye, was added to give a concentration of 5 μ M to both solutions. An argon laser (LASOS LGK 7872 ML05, wavelength 514 nm) and a diode pumped solid state laser (LASOS DPSS, wavelength 561 nm) were scanned sequentially line by line in order to avoid cross-talk between the two dyes. Emission filters at 525–555 nm and 575–625 nm were used for R6G-EDA and SR101, respectively. The lasers were set at the same intensity in the measurements as during the calibration, and low noise Leica HyD detectors were used in photon counting mode. The scan speed was set at 100 Hz, which, with a resolution of 256×256 pixels, limited the temporal resolution of the pH measurements to 0.1 frame per second. A 3×3 pixel median filter was applied to the images

and the ratio between the R6G-EDA images and SR101 images was calculated for each pixel. This ratio was converted to a pH-value by comparison with a standard curve based on measurements of known pH-values of the calcium-solution. The standard curve was made based on eight samples of known pH. The samples contained 1 M $CaCl_2$, 0.9% NaCl, 20 μ M R6G-EDA, 5 μ M SR101 and either 50 mM sodium acetate or TRIS buffer and ranged from pH 4 to 7.5 in 0.5 intervals. Three images were recorded at different locations for each of the eight pH values, and pixel ratios were found as described above. The SR101/R6G-EDA ratio was used for pH-values above pH 5.5 while the R6G-EDA/SR101-ratio was used for pH-values below 5.5. The measured intensity ratios were fitted with a fourth degree polynomial for SR101/R6G-EDA and a seventh degree polynomial for R6G-EDA/SR101. The measurements and resulting fits can be seen in Fig. S.1a in the Supplementary Info. These curves were then used to convert the intensity ratio in an image pixel into a pH value. Fig. S.2b in the Supplementary Info shows a correlation plot of the known pH-values vs. the measured pH with the method described.

2.6. Raman microspectroscopy

Raman microspectroscopy was performed using a Renishaw InVia Reflex Spectrometer equipped with a 532 nm laser (RL532C100) through a Leica 10X 0.25NA lens. The flow cell for these experiments was made in the same way as described earlier, although the regular microscope slides were replaced with Raman grade CaF_2 -slides from Crystran Ltd, UK (see Fig. S.2). Spatial information was obtained by collecting measurements while scanning the laser across the hydrogel discs. Line scans were performed by scanning 50 points along the radius of hydrogel discs, resulting in one point approximately every 15 μ m. 10 spectra were collected for 3 s each and co-added to produce a single spectrum for each point. Database samples for Raman analysis of brushite (DCPD), octacalcium phosphate (OCP) and hydroxyapatite (HAp) were prepared according to methods described by Elliott and phase purity was confirmed with powder X-ray diffraction (D8 Advance DaVinci, Bruker AXS) prior to Raman measurements, see Fig. S.3 [42].

2.7. Scanning electron microscopy

For scanning electron microscopy (SEM) studies, the samples made in the flow cell were rinsed with DIW after a given time inside the flowcell. The flowcell was separated and the alginate discs were dehydrated in increasing concentrations of ethanol and critical point dried using CO_2 (Emitech K850 critical point dryer). Dried samples were attached to SEM stubs with carbon tape

and sputter coated (Cressington 208 HR) with 5 nm platinum/palladium (80/20). Imaging was performed with an accelerating voltage between 1 and 10 kV (Hitachi S-5500 S(T) EM).

2.8. Numerical solution of gelling model

Numerical modeling of the gelling process was based on a simple reaction–diffusion model originally proposed by Mikkelsen–Elgsaeter and an alginate–calcium interaction scheme commonly referred to as the egg-box model [22,34,36]. Combined with adjustments for calcium binding stoichiometry proposed by Thu et al. the following system of differential equations have been obtained: [35]

$$\frac{\partial c}{\partial t} = D_c \nabla^2 c - N_c \frac{\partial g}{\partial t} \quad (1)$$

$$\frac{\partial a}{\partial t} = \nabla [D_a \nabla a] - \frac{\partial g}{\partial t} \quad (2)$$

$$\frac{\partial g}{\partial t} = kca^2 + kag \quad (3)$$

Here, c , a , and g are the total concentration of calcium, ungelled alginate and gelled alginate, respectively (c and a are given as the concentration of alginate monomers, equivalent to the molar concentration of carboxyl groups). D_c and D_a are the diffusion constants for calcium ions and ungelled alginate molecules. N_c is a stoichiometric coefficient describing the number of calcium-ions per alginate-dimer, dependent on both the guluronic acid content of the alginate as well as the affinity between calcium ions and alginate blocks. Finally, in this model k is an effective reaction rate constant [36]. The model has in principle four adjustable parameters: N_c , D_c , D_a , k , in addition to the CaCl_2 and alginate concentrations which were determined by the experimental conditions.

The system of differential equations was solved numerically in MATLAB using the built-in solver `pdepe` for one dimensional parabolic–elliptic partial differential equations. In all cases, 1000 time steps were used and an evenly spaced grid of 2000 points was used for the spatial dimension along the radius of an alginate cylinder or alginate sphere for which the gel front position as a function of time was calculated. The reaction–diffusion model was solved in cylindrical or spherical coordinate system using the option of the `pdepe` solver for disc and sphere geometries respectively.

Comparison between the gel front position predicted by the model and observed experimentally was used to determine the adjustable parameters in the model. Previously reported values of the diffusion constant for calcium ions in free solution of $0.78 \times 10^{-9} \text{ m}^2 \text{ s}^{-1}$ was used for D_c [43]. The diffusion of Ca^{2+} in the alginate gel is largely unaffected by the gel network since the diffusion of molecules with a molecular weight below $2 \times 10^4 \text{ g mol}^{-1}$ are expected to behave the same as in free solution [44]. A diffusion constant for ungelled alginate of $1 \times 10^{-11} \text{ m}^2 \text{ s}^{-1}$ was used, since the gel front kinetics do not strongly depended on the diffusion constant of alginate [34]. The two remaining parameters of the model N_c and k were determined by fitting the predicted gelling kinetics to the experimental data and calculating the root-mean-square error. A systematic search through the parameter space was used in order to exclude local minima.

3. Results and discussion

3.1. Kinetics of alginate gel formation

The design of the flow cell is shown in Fig. 1a. Fig. 1b and c illustrate the processes that can be studied in the flow cell system. In the first instance we investigated the kinetics of alginate gel forma-

tion in order to verify the experimental design and to investigate the dependence of gel formation kinetics on gelling ion concentration, pH and the presence of additives such as NaCl. Following introduction of the calcium solution to the flow cell, the gel front could be observed both in dark field (DF) microscopy (Fig. 2) as well as in CLSM when fluorescently labeled alginate was used (Fig. 3). In DF microscopy, the gel front was visible as a narrow bright band and significant contrast between gelled and ungelled alginate was observed, presumably due to the difference in refractive index for the two conditions. In CLSM the gel front was visible as a narrow region with reduced fluorescence (depletion zone) as shown in Fig. 3. The origin of that depletion zone is described below and has also been observed previously [34].

For DF microscopy, a series of images were recorded and analyzed to determine the velocity of the gel front, see Fig. 2a. The position of the gel front was determined using a custom MATLAB script and was plotted as a function of time, see Fig. 2b. To compare gelling kinetics for different experimental conditions, the slope of the linear region in a plot of the front position versus time was used. The advantage of our experimental system is a well defined cylindrical geometry, with a flux of gelling ions only along the radial coordinate. The alginate and gel concentrations, as well as the concentrations of gelling and non-gelling ions was uniform along the direction parallel to the flow cell normal. For this sample geometry, the gel front velocity in the linear region was measured to increase from approximately $1 \mu\text{m s}^{-1}$ up to $4.5 \mu\text{m s}^{-1}$ when the calcium concentration was increased from 50 mM to 1 M, respectively, see Fig. 2c. The gel front velocity determined from the position of the depletion zone observed in CLSM when using a fluorescently labeled alginate corresponded well to that determined by DF microscopy (Fig. 3b). This confirms that both techniques allowed direct observation of the gel front. It is therefore straightforward to investigate the influence of other experimental parameters on the gel front kinetics, such as pH and ionic strength. Using the setup described above, we have found that the gel front velocity was not substantially dependent on the addition of NaCl (see Fig. S.4a). The largest difference was observed for 1 M CaCl_2 , where the gel front velocity was increased from $4.4 \mu\text{m s}^{-1}$ to $4.9 \mu\text{m s}^{-1}$ upon addition of 0.9% NaCl. High salt concentration is expected to lower the binding between alginate and Ca^{2+} ions due to increased screening and competition with the Na^+ ions, which in turn should increase the gel front velocity. No difference was found for unbuffered samples (pH ~ 7) and samples buffered at pH 6.5 and 7.4, see Fig. S.4b.

The results obtained for disc geometries cannot be directly compared with literature values measured for spherical geometries, as the sample geometry affects the flux of ions to the gel core, and the front velocity is different for the two cases. However, our results allow for the development of a gelling model which can be used to predict gelling kinetics for spherical geometries from the parameters determined for cylindrical geometries (see below for a more detailed description of the modeling strategy). The observed gel front velocity in a disc geometry recalculated to a spherical geometry and experimental conditions as used by Thu et al. (50 mM CaCl_2 , $d = 4 \text{ mm}$, 1.8% alginate solution), gives the velocity in the linear region equal to $1.1 \mu\text{m s}^{-1}$. The average velocity for the whole gelling process and not only for the linear region for this sample size, geometry, and ionic strength was herein calculated to be $1.4 \mu\text{m s}^{-1}$, which is in good agreement with the estimate of $1.7 \mu\text{m s}^{-1}$ based on low resolution optical microscopy in the work of Thu et al. [35].

3.2. Modeling

Experimental data was used to construct a quantitative description of the gelling process by fitting the observed, time dependent

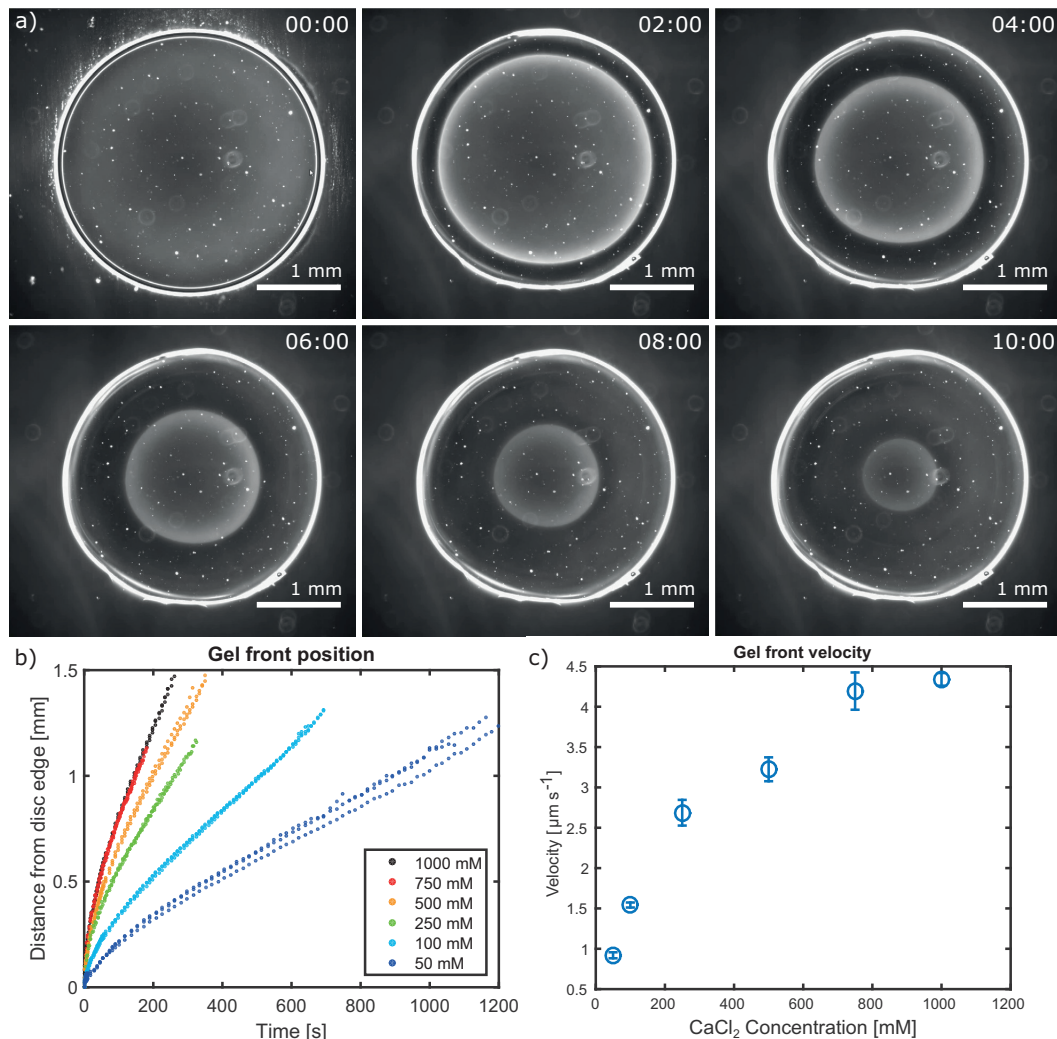


Fig. 2. (a) Gel front position as observed by DF microscopy for gelling with 100 mM CaCl_2 at indicated timepoints (minutes). (b) Gel front position as a function of time determined from DF micrographs for CaCl_2 between 50 mM and 1 M showing 3 parallel experiments for each concentration. (c) Gel front velocity as a function of CaCl_2 concentration determined from the linear region. (For interpretation to colours in this figure, the reader is referred to the web version of this paper.)

gel front position to those predicted from the reaction–diffusion model described above. The model has 4 adjustable parameters, namely the diffusion constants for ungelled alginate and calcium ions D_a and D_c , the reaction rate for egg-box formation k and the Ca^{2+} binding stoichiometry coefficient N_c [34,36]. As described in materials and methods, literature values for D_c and D_a were used here. The two remaining parameters of the model, N_c and k , were determined by comparing the predicted gelling kinetics with experimental data. We started by determining the values of the two model parameters using gel front position data from an experiment using 1 M CaCl_2 solution. As illustrated in Fig. 4a, excellent agreement between the observed and modeled gel front positions was obtained for $k \geq 275 \text{ M}^{-2} \text{ s}^{-1}$, $N_c = 0.30$ at 1 M CaCl_2 . We found that all models with k larger than this lower boundary value could explain the experimental data. This clearly indicates that the

gel front velocity is limited by the diffusion of ions and not by reaction kinetics. If the proposed modeling approach is correct, the model should be able to predict gel front position as a function of time for samples with other concentrations of CaCl_2 without recourse to modify any other model parameters. Indeed, good agreement between the observed and predicted gel front position for all investigated CaCl_2 concentrations down to 50 mM was observed. The agreement is excellent for 750 mM, 500 mM and 250 mM. For the two lowest concentrations (100 mM and 50 mM) the model predicts the correct slope (velocity of the gel front), but the experimental curve is slightly offset with respect to that predicted by the model (Fig. 4a). However, it is important to note that for the two lowest concentrations tested, the gel front was more difficult to observe in the optical techniques used here and its absolute position might be subject to a larger systematic

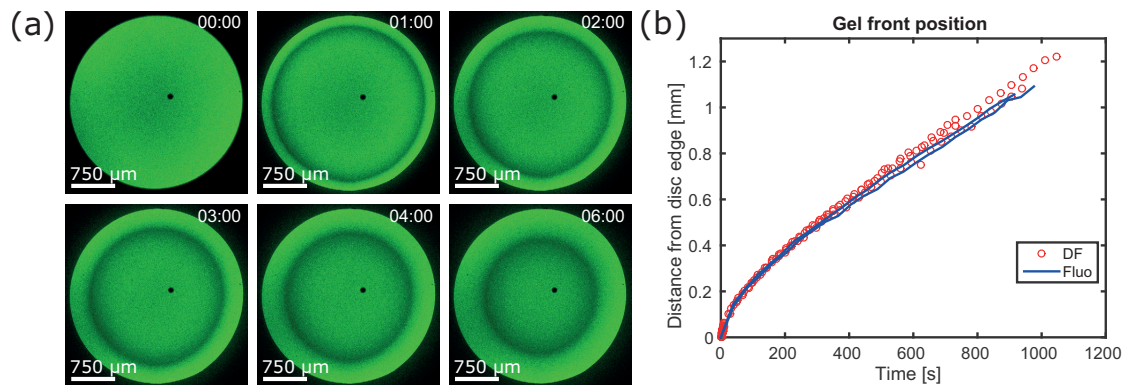


Fig. 3. (a) Time series of alginate gelling in flow cells as determined by confocal microscopy. Brightness corresponds to the fluorescence intensity of labeled alginate and the time difference between frames is 60 s. The top left image was taken immediately before the gelling solution was added. The gel front is visible as a region with reduced fluorescence moving towards the center of the disc. (b) A comparison of the gel front position as a function of time as determined by CLSM and DF microscopy showing excellent correlation between the two techniques. In both (a) and (b) the concentration of gelling solution was 50 mM CaCl_2 . (For interpretation to colours in this figure, the reader is referred to the web version of this paper.)

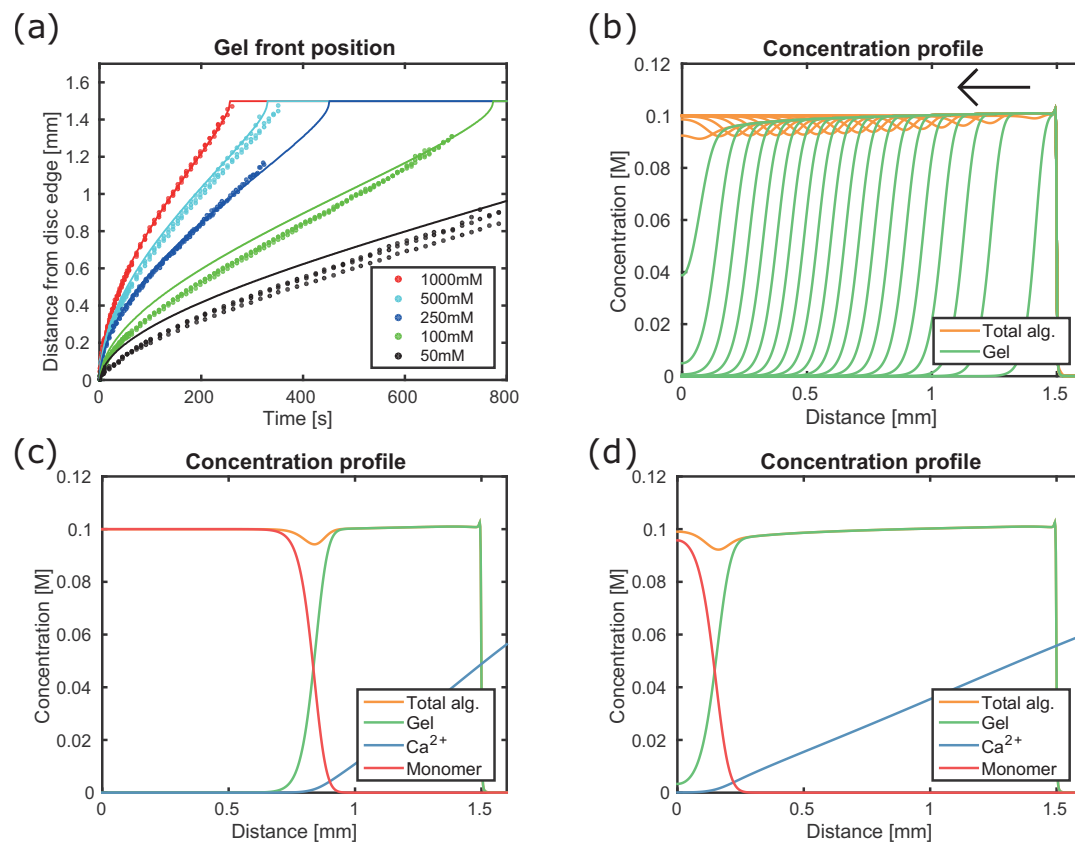


Fig. 4. (a) A comparison of the gel front position as a function of time as determined experimentally by DF microscopy (dots) compared to model predictions (line). (b) Modelling of the spatiotemporal evolution of the gelled alginate concentration (gel front) calculated for 100 mM CaCl_2 at intervals of 40 s. The movement of the gel front is indicated by an arrow. (c) and (d) Concentration profiles for Ca^{2+} (black), ungelled (blue), gelled (red) and total alginate (i.e. ungelled + gelled, green) 240 s (c) and 720 s (d) after the gelling was initiated, calculated for a gelling solution concentration of 100 mM. (For interpretation of the references to colour in this figure caption, the reader is referred to the web version of this article.)

error. This is a likely cause of the slight discrepancy in the calculated gel front velocity between the work of Thu et al. and the results presented here.

We also note that our experimental system could be used to precisely determine the diffusion constant of alginate during gel formation at various conditions using CLSM, fluorescently labeled alginate and the shape and intensity reduction in a clearly visible depletion zone by applying, for example, the theoretical framework presented recently by Braschler et al. [34]. This is, however, beyond the scope of the current work and would serve as an interesting addition. This approach could also be used to study

the reaction constant k for different types of alginates or reaction with various divalent cations in great detail.

As described by Braschler et al the determined N_c parameter is closely related to the fraction of G-units of alginate, assuming that only G-units are able to bind Ca^{2+} ions and that the binding is independent of the sequence of G and M units [34]. In practice, it is known that divalent cation binding by G-blocks in alginate is cooperative, and a longer stretch of consecutive G-units is needed to form stable junction zones [22]. It has also been shown that MG-sequences bind Ca^{2+} [24]. We can use our measured value for N_c to estimate the apparent fraction of G-units that rapidly binds

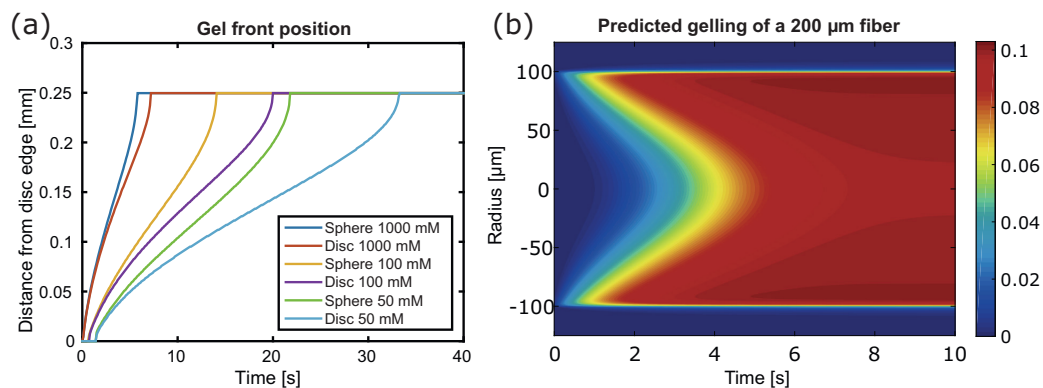


Fig. 5. (a) The calculated gel front position as a function of time for a spherical and cylindrical geometry with radius = 250 μm for different CaCl_2 concentrations (50 mM, 100 mM and 1000 mM) using the proposed model. (b) The calculated amount of gelled alginate (between 0 and 0.1 M) for a fiber with radius = 100 μm in a microfluidic device with 100 mM CaCl_2 . The X-axis represents time in the gelling channel. (For interpretation to colours in this figure, the reader is referred to the web version of this paper.)

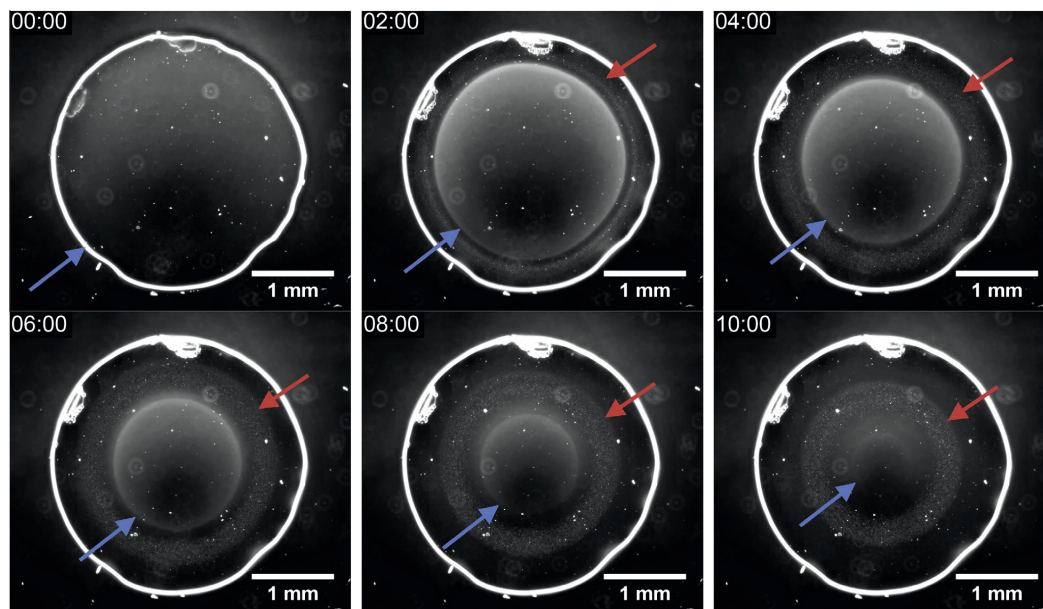


Fig. 6. Gel front and mineral front position as observed by DF microscopy of a phosphate-containing alginate disc gelled with 1 M CaCl_2 solution. The gel front indicated by blue arrows appeared weaker and moved slower as compared to previous experiments without phosphate. A moving front of minerals indicated by red arrows trailed the gel front and widened over time. Time for each frame in minutes is shown in the top left corner. (For interpretation of the references to colour in this figure caption, the reader is referred to the web version of this article.)

calcium during the initial gel formation step, F_G^* , F_G^* is still related to the stoichiometry in the egg-box model and is given as [45]:

$$F_G^* = \frac{4}{3} N_c$$

Using the equation above, F_G^* was calculated to be 0.4 and this is based only on the amount of Ca^{2+} ions consumed during the gelling process. Note that this experiment has only considered alginate sequences with the highest affinity for Ca^{2+} ions, and it is likely that more Ca^{2+} ions are bound to the polymer as the gel matures [23,46]. This cooperative binding i.e. blocks of G-monomers will bind Ca^{2+} faster than single G-monomers, is a probable reason for the discrepancy between the calculated $F_G^* = 0.4$ and the $F_G = 0.67$ given by the manufacturer.

The predicted temporal evolution of the gel front is illustrated in Fig. 4b where the gelled alginate concentration profiles (green line) and the total alginate (orange line) are plotted at 40 s intervals (these concentrations refer to alginate monomers, not alginate molecules). Here a depletion zone is clearly seen moving towards the center of the disc (at $r = 0$), which is consistent with observations made by CLSM. The origin of this depletion zone is illustrated more clearly in Fig. 4c and d where the predicted concentration profiles for Ca^{2+} (blue), ungelled (red), gelled (green) and total alginate (orange) at 240 s and 720 s after the gelling was initiated are shown. Gelling is predicted to be confined to a small region of approximately 200 μm , where the solution rapidly transitions from an ungelled Na-alginate sol to gelled Ca-alginate gel.

Fig. 5a shows the developed model applied to the prediction of gelling kinetics for two different geometries of alginate sample, discs and spheres, as a function of CaCl_2 concentration. Here, the diameter of both geometries was set to 500 μm which represents

a typical size of an alginate bead used for cell encapsulation. The model predicts that at a concentration of 50 mM CaCl_2 , the time needed to fully gel such a bead is approximately 20 s; the gelling time is reduced to 15 s and 5 s for 100 and 1000 mM CaCl_2 respectively.

Fig. 5b illustrates a simulation in which the gelling model was applied to predict how gelling would occur when an alginate fiber is produced in a coaxial flow microfluidic device [10,47]. Here, we have simulated a central alginate stream with a circular cross-section and a diameter of 200 μm which contacts the gelling solution from both sides and flows to the right with the same velocity at $t = 0$. The alginate and gelling stream flow together and Ca^{2+} diffuses into the alginate causing gel formation. Gelling begins along the fiber edges and after approximately 600 ms a shell of gelled alginate has formed around the fiber. After 3.5 s, 50% of the alginate in the fiber core is gelled and a fully gelled fiber is formed after approximately 7.5 s. Some residual inhomogeneity with respect to the gelled alginate concentration in the fibers is observed with the lowest concentration in the center, which is comparable to the sphere and disc geometries. Depending on the flow rate, this can be used to calculate the length of the channel where gelling occurs in a microfluidic device.

3.3. Mineralization

By introducing a phosphate precursor into the alginate solution, precipitation of calcium phosphate mineral may occur at the same time as the gel is formed following addition of Ca^{2+} . As illustrated in Fig. 6, deposition of the mineral phase could be directly observed using optical microscopy. Here, the alginate solution contains 300 mM of sodium phosphate. The formed mineral phase was

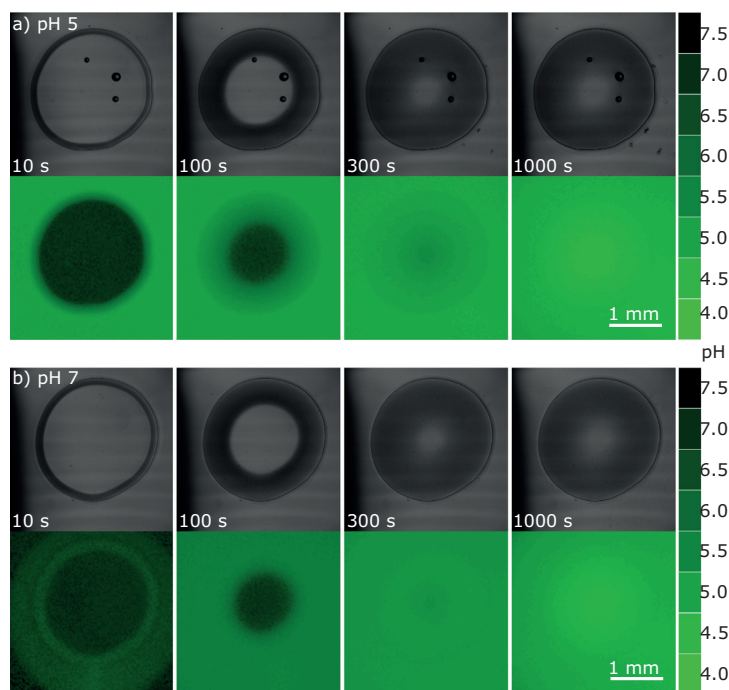


Fig. 7. (a) Bright field images (top) and pH-images (bottom) of a phosphate containing sample subjected to 1 M CaCl_2 buffered at pH 5. The intensity in the green images correspond to the pH given in the scale on the right. (b) Bright field images (top) and pH-images (bottom) of a phosphate containing sample subjected to 1 M CaCl_2 buffered at pH 7. In both cases, the initial pH of the alginate was pH 7. (For interpretation to colours in this figure, the reader is referred to the web version of this paper.)

typically visible as an opaque, light scattering region close to, but trailing slightly behind the gel front. Interestingly, the appearance of this region was not constant, but appeared to change with time, within both short (i.e. minutes) and long (i.e. tens of hours) time scales.

It is known that CaP crystallization might cause local changes in the pH of the sample due to different stoichiometry of CaP phases. To investigate this aspect of the mineralization process, CLSM in combination with two fluorescent dyes was used. The dye R6G-EDA is known to have an increasing fluorescence intensity as the degree of protonation increases and has a detectable fluorescence from pH 7.5 and accurate measurements of pH changes can be made between pH 4–6 [41]. We also applied a pH-insensitive dye, SR101, in order to correct for artifacts in fluorescence intensity measurements which may occur due to dilution, sample thickness, uneven illumination and scattering from mineral formation. This combination of dyes gave excellent sensitivity to pH in the range of pH 4–6.5, see Fig. S.1.

Fig. 7 shows bright field and R6G-EDA/SR101 ratio images of two mineralizing samples at different time points. For the sample marked pH 5, the alginate disc was buffered at pH 7 due to the phosphate content and the surrounding calcium solution was buffered at pH 5. As mineral precipitated and the surrounding solution diffused into the alginate disc, the pH was lowered. For this sample, the gelling process was completed after 300 s, however the pH

continued to drop and reached a minimum of 4.4 in the center of the disc after approximately 18 min. The sample marked pH 7 was made in a similar manner except that the gelling solution was buffered at pH 7. Here the increased fluorescence intensity was entirely due to H^+ produced during the mineralization process. This sample also showed the same trend with the lowest pH observed at the center of the disc. The pH in the center of the disc was found to drop to 4.5 after approximately 20 min. Once the pH had reached this minimum it was stable in the center of the disc for the rest of the measurement which, in both cases, lasted 33 min in total. A probable cause was the consumption of the buffer agent (phosphate buffer) within the discs in the mineralization process, resulting in a pH-gradient as the buffer agent in the surrounding solution (TRIS or sodium acetate) diffused into the gelling disc. This gradient persisted throughout the duration of the experiments.

The sample geometry allowed for *in situ* monitoring of the mineral formation and transformation using confocal Raman microspectroscopy (CRM). This is especially important, as dehydration needed for characterization using powder X-ray diffraction (XRD) or electron diffraction techniques might introduce changes in the mineral phase. Also, due to small sample size, characterization, particularly using XRD, is challenging. Fig. 8a shows Raman spectra of several minerals and species of interest for our mineralized alginate composite, including HAp, OCP, brushite, alginate and alginate-phosphate precursor solution. Fig. 8b shows a heat map

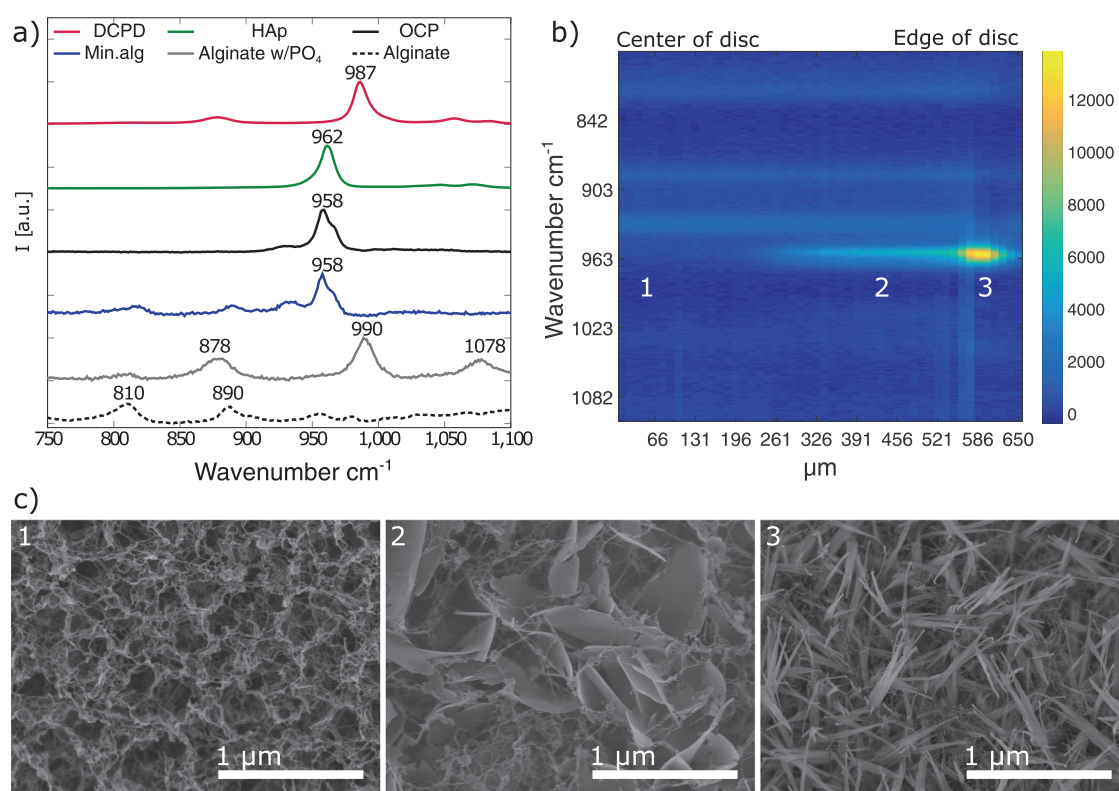


Fig. 8. (a) Raman spectra of relevant standard samples showing typical features which can be identified. (b) A heat map showing the distribution of mineral from the center towards the edge of the disc. The white numbers refer to the positions of SEM-images shown in (c). (c) SEM images of positions 50 μm from the center (1), 450 μm from the center (2) and 600 μm from the center, close to the edge (3) of a mineralized alginate disc after 24 h in the gelling solution. (For interpretation to colours in this figure, the reader is referred to the web version of this paper.)

generated by collecting Raman spectra in a radial direction across a mineralized alginate disc. Here the data was collected from a sample which was prepared with alginate containing 300 mM phosphate and gelled in 1 M CaCl_2 buffered at pH 5 with sodium acetate. In the region close to the disc edge, an intense signal located at 958 cm^{-1} , corresponding to OCP was recorded. In the region of interest, the OCP Raman spectrum consists of a main peak at 958 cm^{-1} and a distinct shoulder at 967 cm^{-1} [48]. There is also a characteristic (but weak) HPO_4 -stretch located at 1010 cm^{-1} , however, this peak was close to the background level in the used experimental conditions. The peak shape of HAp is more symmetrical (although there is a slight shoulder at lower wavenumbers, i.e. the other side than the OCP-shoulder) and via curve-fitting the two phases can be distinguished using Raman microspectroscopy [49]. A weaker signal from the alginate itself was also observed at 816 and 890 cm^{-1} as well as a broad peak from the acetate buffer at 932 cm^{-1} . The signal from alginate and buffer were unchanged throughout the radius of the disc, while the signal from the mineral was strong towards the edge and gradually diminished towards the center of the disc. No mineral was detected in a radius of $250\text{ }\mu\text{m}$ from the center of the disc.

The morphology of the formed mineral phase was investigated at high resolution using SEM after careful drying of the samples. SEM could also be applied to the same sample as CRM, therefore allowing highly accurate phase identification combined with high magnification imaging of the same area. Fig. 8c shows example images of a mineralized alginate sample, showing the difference in mineral content and morphology at different areas of the disc: at the center (1), halfway to the edge (2) and at the edge (3). Their corresponding positions are marked in Fig. 8b. In the center, no mineral was observed, corroborating the CRM measurements described earlier. Further towards the edge of the sample, mineral platelets were dispersed in the alginate network. Close to the edge of the disc, a large abundance of acicular crystals were found. The images in Fig. 8c correspond to positions 50, 450 and $600\text{ }\mu\text{m}$ respectively in Fig. 8b. The combination of these techniques can also be used to study mineral phase transformations within the hydrogel, and this concept is studied in detail elsewhere [49].

4. Conclusion

In summary, we have developed an experimental platform in which the gelling kinetics of polymers capable of ionotropic gelation can be studied with high spatial and temporal resolution. The gel front velocity for 1.8% high G-content alginate gel was measured at a range of condition with both transmitted light and fluorescence microscopy. For the disc geometry investigated in this study, this velocity ranged from 1 to $5\text{ }\mu\text{m s}^{-1}$ for CaCl_2 concentrations between 50 mM and 1 M. Modeling of the gel formation process based on a reaction–diffusion approach was implemented and the gelling front velocity was calculated for a range of geometries and CaCl_2 concentrations. The calculated values are in excellent agreement with measured or previously published data. The same platform was combined with several other analytical techniques such as confocal Raman microspectroscopy, confocal laser scanning microscopy and scanning electron microscopy to obtain temporally and spatially resolved information regarding the chemical composition, polymer concentration, evolution of pH and sub-micron morphology of regions of interest. This is especially suitable for characterization of *in situ* mineralization processes of a hydrogel system, here demonstrated by mineralization of alginate with calcium phosphate. The presented platform represents a powerful new characterization toolbox to undertake studies of gelling kinetics, *in situ* mineral formation and maturation behavior within hydrogels in exquisite detail.

Acknowledgments

The authors thank the Research Council of Norway FRINATEK project 214607 and NANO2021 project 220005 (A.K.O.Å.) for financial support.

Appendix A. Supplementary data

Supplementary data associated with this article can be found, in the online version, at <http://dx.doi.org/10.1016/j.actbio.2016.07.046>.

References

- [1] A. Steinbüchel (Ed.), Biopolymers Online, Wiley-VCH Verlag GmbH & Co. KGaA, Weinheim, Germany, 2005, <http://dx.doi.org/10.1002/3527600035>.
- [2] B.H.A. Rehm (Ed.), Alginates: Biology and Applications, Vol. 13 of Microbiology Monographs, Springer Berlin Heidelberg, Berlin, Heidelberg, 2009, <http://dx.doi.org/10.1007/978-3-540-92679-5>.
- [3] Y.A. Mørch, I. Donati, B.L. Strand, G. Skjåk-Braek, Molecular engineering as an approach to design new functional properties of alginate, *Biomacromolecules* 8 (9) (2007) 2809–2814, <http://dx.doi.org/10.1021/bm700502b>.
- [4] K.B. Fonseca, D.B. Gomes, K. Lee, S.G. Santos, A. Sousa, E.A. Silva, D.J. Mooney, P. L. Granja, C.C. Barrias, Injectable MMP-sensitive alginate hydrogels as hMSC delivery systems, *Biomacromolecules* 15 (1) (2014) 380–390, <http://dx.doi.org/10.1021/bm4016495>.
- [5] K.Y. Lee, D.J. Mooney, Hydrogels for tissue engineering, *Chem. Rev.* 101 (7) (2001) 1869–1879.
- [6] J.E. Melvik, M. Dornish, Alginate as a carrier for cell immobilisation, *Focus Biotechnol.* vol. 8A Fundam. Cell Immobil. Biotechnol., Kluwer Academic Press, 2004, pp. 165–183.
- [7] E. Alsberg, K.W. Anderson, A. Albeiruti, R.T. Franceschi, D.J. Mooney, Cell-interactive alginate hydrogels for bone tissue engineering, *J. Dent. Res.* 80 (11) (2001) 2025–2029.
- [8] G. Chan, D.J. Mooney, New materials for tissue engineering: towards greater control over the biological response, *Trends Biotechnol.* 7 (2008) 382–392.
- [9] A.M. Rokstad, I. Donati, M. Borgogna, J. Oberholzer, B.L. Strand, T. Espevik, G. Skjåk-Braek, Cell-compatible covalently reinforced beads obtained from a chemoenzymatically engineered alginate, *Biomaterials* 27 (27) (2006) 4726–4737, <http://dx.doi.org/10.1016/j.biomaterials.2006.05.011>.
- [10] S.-J. Shin, J.-Y. Park, J.-Y. Lee, H. Park, Y.-D. Park, K.-B. Lee, C.-M. Whang, S.-H. Lee, On the fly continuous generation of alginate fibers using a microfluidic device, *Langmuir* 23 (17) (2007) 9104–9108, <http://dx.doi.org/10.1021/la700818q>.
- [11] S. Sugiyama, T. Oda, Y. Aoyagi, M. Satake, N. Ohkohchi, M. Nakajima, Tubular gel fabrication cell encapsulation in laminar flow stream formed by microfabricated nozzle array, *Lab Chip* 8 (8) (2008) 1255–1257, <http://dx.doi.org/10.1039/b803850c>.
- [12] R. Pereira, A. Carvalho, D.C. Vaz, M.H. Gil, A. Mendes, P. Bártolo, Development of novel alginate based hydrogel films for wound healing applications, *Int. J. Biol. Macromol.* 52C (2012) 221–230, <http://dx.doi.org/10.1016/j.ijbiomac.2012.09.031>.
- [13] T. Huq, S. Salmieri, A. Khan, R.A. Khan, C. Le Tien, B. Riedl, C. Fraschini, J. Bouchard, J. Uribe-Calderon, M.R. Kamal, M. Lacroix, Nanocrystalline cellulose (NCC) reinforced alginate based biodegradable nanocomposite film, *Carbohydr. Polym.* 90 (4) (2012) 1757–1763, <http://dx.doi.org/10.1016/j.carbpol.2012.07.065>.
- [14] T. Andersen, J.E. Melvik, O. Gåserød, E. Alsberg, B.E. Christensen, Ionically gelled alginate foams: physical properties controlled by operational and macromolecular parameters, *Biomacromolecules* 13 (11) (2012) 3703–3710, <http://dx.doi.org/10.1021/bm301194f>.
- [15] K. Pataky, T. Bräschler, A. Negro, P. Renaud, M.P. Lutolf, J. Brugger, Microdrop printing of hydrogel bioinks into 3D tissue-like geometries, *Adv. Mater.* (Deerfield Beach, Fla.) (2011) 391–396, <http://dx.doi.org/10.1002/adma.201102800>.
- [16] T. Andersen, B.L. Strand, K. Formo, E. Alsberg, B.E. Christensen, Chapter 9, <http://dx.doi.org/10.1039/9781849732765-00227>.
- [17] J. Sun, H. Tan, Alginate-based biomaterials for regenerative medicine applications, *Materials (Basel)* 6 (4) (2013) 1285–1309, <http://dx.doi.org/10.3390/ma6041285>.
- [18] J.A. Rowley, D.J. Mooney, Alginate type and RGD density control myoblast phenotype, *J. Biomed. Mater. Res.* 60 (2) (2002) 217–223, <http://dx.doi.org/10.1002/jbm.1287>.
- [19] O. Chaudhuri, L. Gu, D. Klumpers, M. Darnell, S.A. Bencherif, J.C. Weaver, N. Huebsch, H.-P. Lee, E. Lippens, G.N. Duda, D.J. Mooney, Hydrogels with tunable stress relaxation regulate stem cell fate and activity, *Nat. Mater.* 15 (3) (2015) 326–334, <http://dx.doi.org/10.1038/nmat4489>.
- [20] M.J. Webber, E.A. Appel, E.W. Meijer, R. Langer, Supramolecular biomaterials, *Nat. Mater.* 15 (1) (2015) 13–26, <http://dx.doi.org/10.1038/nmat4474>.
- [21] A. Memic, H.A. Alhadrami, M.A. Hussain, M. Aldahabi, F. Al Nowaiser, F. Al-Hazmi, R. Oklu, A. Khademhosseini, Hydrogels 2.0: improved properties

- with nanomaterial composites for biomedical applications, *Biomed. Mater.* 11 (1) (2015) 014104, <http://dx.doi.org/10.1088/1748-6041/11/1/014104>.
- [22] G.T. Grant, E.R. Morris, D.A. Rees, P.J. Smith, D. Thom, Biological interactions between polysaccharides and divalent cations: the egg-box model, *FEBS Lett.* 32 (1) (1973) 195–198, [http://dx.doi.org/10.1016/0014-5793\(73\)80770-7](http://dx.doi.org/10.1016/0014-5793(73)80770-7).
- [23] M. Borgogna, G. Skjåk-Bræk, S. Paoletti, I. Donati, On the initial binding of alginate by calcium ions. The tilted egg-box hypothesis, *J. Phys. Chem. B* 117 (24) (2013) 7277–7282, <http://dx.doi.org/10.1021/jp4030766>.
- [24] I. Donati, S. Holtan, Y.A. Mørch, M. Borgogna, M. Dentini, G. Skjåk-Braek, New hypothesis on the role of alternating sequences in calcium-alginate gels, *Biomacromolecules* 6 (2) (2005) 1031–1040, <http://dx.doi.org/10.1021/bm049306e>.
- [25] D.W. Green, I. Leveque, D. Walsh, D. Howard, X.B. Yang, K. Partridge, S. Mann, R.O.C. Oreffo, Biomaterialized polysaccharide capsules for encapsulation organization, and delivery of human cell types and growth factors, *Adv. Funct. Mater.* 15 (6) (2005) 917–923.
- [26] Z.A.C. Schnepf, R. Gonzalez-McQuire, S. Mann, Hybrid biocomposites based on calcium phosphate mineralization of self-assembled supramolecular hydrogels, *Adv. Mater.* 18 (14) (2006) 1869–1872.
- [27] M. Xie, M.Ø. Olderøy, J.-P. Andreassen, S.M. Selbach, B.L. Strand, P. Sikorski, Alginate-controlled formation of nanoscale calcium carbonate and hydroxyapatite mineral phase within hydrogel networks, *Acta Biomater.* 6 (9) (2010) 3665–3675, <http://dx.doi.org/10.1016/j.actbio.2010.03.034>.
- [28] M. Xie, M.Ø. Olderøy, Z. Zhang, J.-P. Andreassen, B.L. Strand, P. Sikorski, Biocomposites prepared by alkaline phosphatase mediated mineralization of alginate microbeads, *RSC Adv.* 2 (4) (2012) 1457, <http://dx.doi.org/10.1039/c1ra00750e>.
- [29] S.H. Bjørnøy, D.C. Bassett, S. Ucar, J.-P. Andreassen, P. Sikorski, Controlled mineralisation and recrystallisation of brushite within alginate hydrogels, *Biomed. Mater.* 11 (1) (2016) 015013, <http://dx.doi.org/10.1088/1748-6041/11/1/015013>.
- [30] H. Tremi, H.-H. Kohler, Coupling of diffusion and reaction in the process of capillary formation in alginate gel, *Chem. Phys.* 252 (1–2) (2000) 199–208, [http://dx.doi.org/10.1016/S0301-0104\(99\)00361-4](http://dx.doi.org/10.1016/S0301-0104(99)00361-4).
- [31] F. Abbona, H. Madsen, R. Boistelle, The initial phases of calcium and magnesium phosphates precipitated from solutions of high to medium concentrations, *J. Cryst. Growth* 74 (3) (1986) 581–590, [http://dx.doi.org/10.1016/0022-0248\(86\)90205-8](http://dx.doi.org/10.1016/0022-0248(86)90205-8).
- [32] S. Ucar, S.H. Bjørnøy, D.C. Bassett, B.L. Strand, P. Sikorski, J.-P. Andreassen, Nucleation and growth of brushite in the presence of alginate, *Cryst. Growth Des.* 15 (11) (2015) 5397–5405, <http://dx.doi.org/10.1021/acs.cgd.5b01032>.
- [33] H.-S. Kim, A kinetic study on calcium alginate bead formation, *Korean J. Chem. Eng.* 7 (1) (1990) 1–6, <http://dx.doi.org/10.1007/BF02697334>.
- [34] T. Braschler, A. Valero, L. Colella, K. Pataky, J. Brugger, P. Renaud, Link between alginate reaction front propagation and general reaction diffusion theory, *Anal. Chem.* 83 (6) (2011) 2234–2242, <http://dx.doi.org/10.1021/ac103118r>.
- [35] B. Thu, O. Gåserød, D. Paus, A. Mikkelsen, G. Skjåk-Bræk, R. Toffanin, F. Vittur, R. Rizzo, Inhomogeneous alginate gel spheres: an assessment of the polymer gradients by synchrotron radiation-induced X-ray emission, magnetic resonance microimaging, and mathematical modeling, *Biopolymers* 53 (1) (2000) 60–71, [http://dx.doi.org/10.1002/\(SICI\)1097-0282\(200001\)53:1<60::AID-BIP6>3.0.CO;2-F](http://dx.doi.org/10.1002/(SICI)1097-0282(200001)53:1<60::AID-BIP6>3.0.CO;2-F).
- [36] A. Mikkelsen, A. Elgsaeter, Density distribution of calcium-induced alginate gels. A numerical study, *Biopolymers* 36 (1) (1995) 17–41, <http://dx.doi.org/10.1002/bip.360360104>.
- [37] O. Bonhomme, J. Leng, A. Colin, Microfluidic wet-spinning of alginate microfibers: a theoretical analysis of fiber formation, *Soft Matter* 8 (41) (2012) 10641, <http://dx.doi.org/10.1039/c2sm25552a>.
- [38] S. Mann, *Biomaterialization Principles and Concepts in Bioinorganic Materials Chemistry*, Oxford Univ Press, 2001.
- [39] B.L. Strand, Y.A. Mørch, K.R. Syvertsen, T. Espevik, G. Skjåk-Braek, Microcapsules made by enzymatically tailored alginate, *J. Biomed. Mater. Res.* 64A (3) (2003) 540–550.
- [40] J.-S. Wu, L.-C. Hwang, K.S. Kim, J.S. Kim, Rhodamine-based Hg²⁺-selective chemodosimeter in aqueous solution: fluorescent OFF-ON, *Org. Lett.* 9 (5) (2007) 907–910, <http://dx.doi.org/10.1021/ol070109c>.
- [41] Z. Li, S. Wu, J. Han, S. Han, Imaging of intracellular acidic compartments with a sensitive rhodamine based fluorogenic pH sensor, *Analyst* 136 (2011) 3698–3706, <http://dx.doi.org/10.1039/c1an15108h>.
- [42] J. Elliott, *Structure and Chemistry of the Apatites and Other Calcium Orthophosphates*, Elsevier B.V., 1994, <http://dx.doi.org/10.1016/B978-0-444-81582-8.50001-8>.
- [43] J.H. Wang, Tracer-diffusion in Liquids. IV. Self-diffusion of Calcium Ion and Chloride Ion in Aqueous Calcium Chloride Solutions 1, *J. Am. Chem. Soc.* 75 (7) (1953) 1769–1770, <http://dx.doi.org/10.1021/ja01103a539>.
- [44] A. Martinsen, I. Storø, G. Skjåk-Braek, Alginate as immobilization material: III. Diffusional properties, *Biotechnol. Bioeng.* 39 (2) (1992) 186–194, <http://dx.doi.org/10.1002/bit.260390210>.
- [45] E.R. Morris, D.A. Rees, D. Thom, J. Boyd, Chiroptical and stoichiometric evidence of a specific, primary dimerisation process in alginate gelation, *Carbohydr. Res.* 66 (1) (1978) 145–154, [http://dx.doi.org/10.1016/S0008-6215\(00\)83247-4](http://dx.doi.org/10.1016/S0008-6215(00)83247-4).
- [46] Y. Fang, S. Al-Assaf, G.O. Phillips, K. Nishinari, T. Funami, P.A. Williams, L. Li, Multiple steps and critical behaviors of the binding of calcium to alginate, *J. Phys. Chem. B* 111 (10) (2007) 2456–2462, <http://dx.doi.org/10.1021/jp0689870>.
- [47] H. Onoe, T. Okitsu, A. Itou, M. Kato-Negishi, R. Gojo, D. Kiriya, K. Sato, S. Miura, S. Iwanaga, K. Kuribayashi-Shigetomi, Y.T. Matsunaga, Y. Shimoyama, S. Takeuchi, Metre-long cell-laden microfibres exhibit tissue morphologies and functions, *Nat. Mater.* 12 (6) (2013) 584–590, <http://dx.doi.org/10.1038/nmat3606>.
- [48] B.O. Fowler, M. Markovic, W.E. Brown, Octacalcium phosphate. 3. Infrared and Raman vibrational spectra, *Chemistry of Materials* 5 (10) (1993) 1417–1423, <http://dx.doi.org/10.1021/cm00034a009>.
- [49] S.H. Bjørnøy, D.C. Bassett, S. Ucar, B.L. Strand, J.-P. Andreassen, P. Sikorski, A correlative spatiotemporal microscale study of calcium phosphate formation and transformation within an alginate hydrogel matrix, *Acta Biomater.* 44 (2016) 254–266, <http://dx.doi.org/10.1016/j.actbio.2016.08.041>.

Supplementary Information for: Gelling kinetics and *in situ* mineralization of alginate hydrogels: a correlative spatiotemporal characterization toolbox

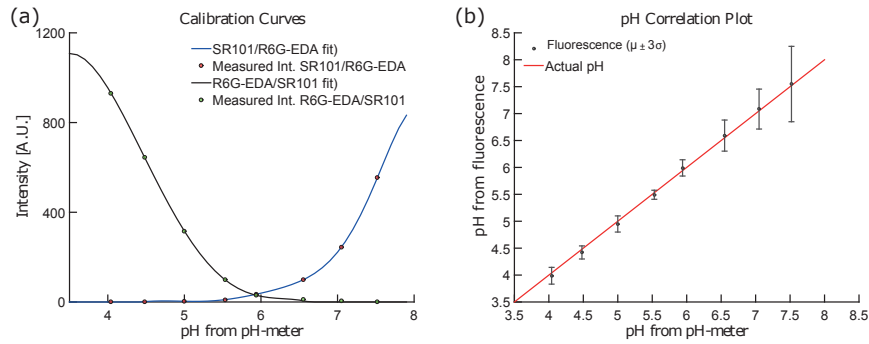


Figure S.1: A plot of the calibration curves (a) and a correlation plot (b) of the actual pH vs measured pH by CLSM. The points in b represent the average pixel value for the three images from each sample and the error bars represent the 3σ values for the deviation from the three images.

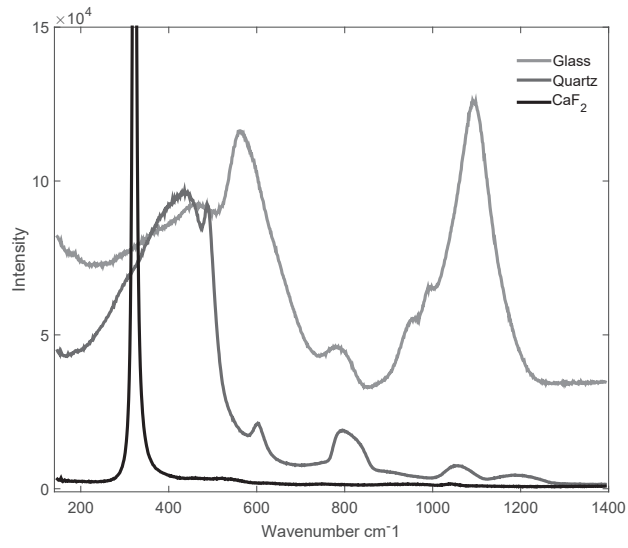


Figure S.2: A comparison of the fluorescence signal from different substrates recorded at identical conditions. The CaF_2 peak at 322 cm^{-1} has been clipped. The main region of interest in this work was situated in the $750\text{--}1100 \text{ cm}^{-1}$, leaving both glass substrates and quartz substrates inferior to CaF_2 substrates for low-signal studies. For further reading, the interested reader is directed to relevant literature.[1, 2]

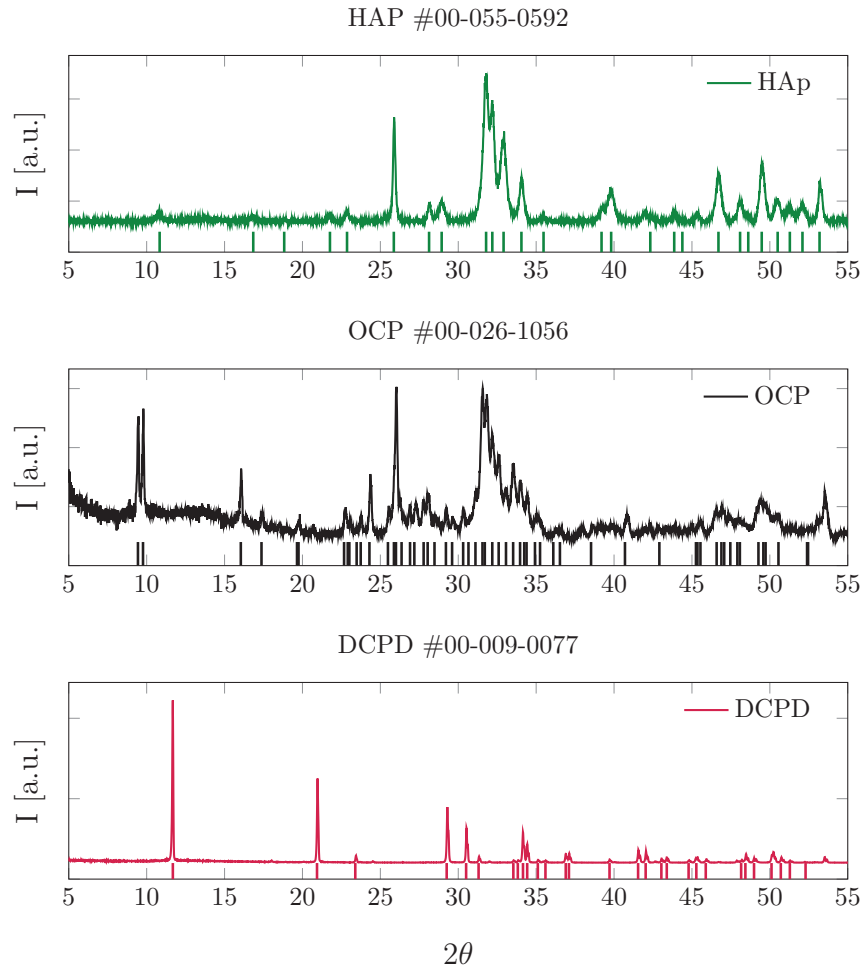


Figure S.3: XRD spectra of the samples prepared as database samples for the Raman analysis. The corresponding ICDD pdf-card number is given in the plot-titles. Part of the data is reproduced from Bjørnøy *et al.*[3]

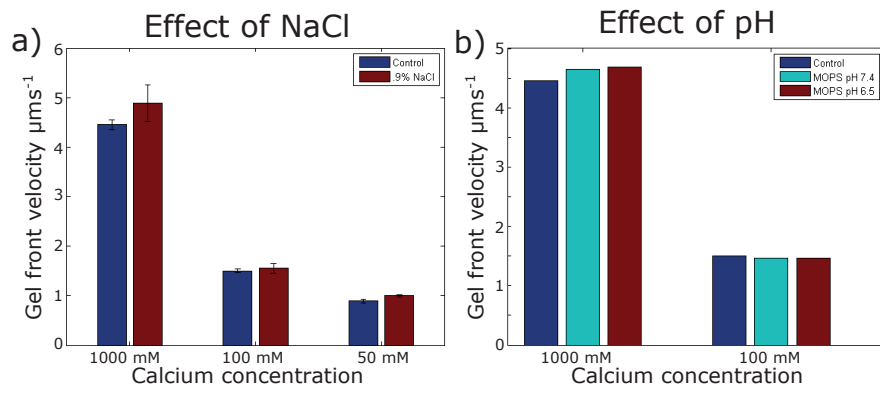


Figure S.4: **a)** shows the effect on the gel front velocity by adding NaCl to the alginate and gelling solution at different calcium concentrations. The addition of NaCl was found to have little effect. **b)** shows the effect on the gel front velocity by changes in pH at different calcium concentrations. The effect of pH in the range used here (pH 6.5 to 7.4) was found to have little effect.

References

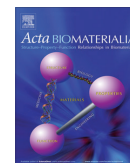
- [1] L. Gasparov, T. Jegorel, L. Loetgering, S. Middey, J. Chakhalian, Thin film substrates from the Raman spectroscopy point of view, *Journal of Raman Spectroscopy* 45 (6) (2014) 465–469.
- [2] L. T. Kerr, H. J. Byrne, B. M. Hennelly, Optimal choice of sample substrate and laser wavelength for Raman spectroscopic analysis of biological specimen, *Anal. Methods* 7 (12) (2015) 5041–5052.
- [3] S. H. Bjørnøy, D. C. Bassett, S. Ucar, B. L. Strand, J.-P. Andreassen, P. Sikorski, A correlative spatiotemporal microscale study of calcium phosphate formation and transformation within an alginate hydrogel matrix, Submitted to *Acta Biomaterialia*.

Paper III



Contents lists available at ScienceDirect

Acta Biomaterialia

journal homepage: www.elsevier.com/locate/actabiomat

Full length article

A correlative spatiotemporal microscale study of calcium phosphate formation and transformation within an alginate hydrogel matrix



Sindre H. Bjørnøy^a, David C. Bassett^a, Seniz Ucar^b, Berit L. Strand^c, Jens-Petter Andreassen^b, Pawel Sikorski^{a,*}

^a Department of Physics, NTNU, Norwegian University of Science and Technology, 7491 Trondheim, Norway

^b Department of Chemical Engineering, NTNU, Norwegian University of Science and Technology, 7491 Trondheim, Norway

^c Department of Biotechnology, NTNU, Norwegian University of Science and Technology, 7491 Trondheim, Norway

ARTICLE INFO

Article history:

Received 28 May 2016

Received in revised form 16 August 2016

Accepted 19 August 2016

Available online 24 August 2016

Keywords:

Alginate

Hydrogel

Raman spectroscopy

Calcium phosphate

ABSTRACT

The modification of soft hydrogels with hard inorganic components is a method used to form composite materials with application in non-load-bearing bone tissue engineering. The inclusion of an inorganic component may provide mechanical enhancement, introduce osteoconductive or osteoinductive properties, or change other aspects of interactions between native or implanted cells and the material. A thorough understanding of the interactions between such components is needed to improve the rational design of such biomaterials. To achieve this goal, model systems which could allow study of the formation and transformation of mineral phases within a hydrogel network with a range of experimental methods and high spatial and time resolution are needed. Here, we report a detailed investigation of the formation and transformation process of calcium phosphate mineral within an alginate hydrogel matrix. A combination of optical microscopy, confocal Raman microspectroscopy and electron microscopy was used to investigate the spatial distribution, morphology and crystal phase of the calcium phosphate mineral, as well as to study transformation of the mineral phases during the hydrogel mineralization process and upon incubation in a simulated body fluid. It was found, that under the conditions used in this work, mineral initially formed as a metastable amorphous calcium phosphate phase (ACP). The ACP particles had a distinctive spherical morphology and transformed within minutes into brushite in the presence of brushite seed crystals or into octacalcium phosphate, when no seeds were present in the hydrogel matrix. Incubation of brushite–alginate composites in simulated body fluid resulted in formation of hydroxyapatite. The characterization strategy presented here allows for non-destructive, *in situ* observation of mineralization processes in optically transparent hydrogels with little to no sample preparation.

Statement of Significance

The precipitation and transformations of calcium phosphates (CaP) is a complex process, where both formation kinetics and the stability of different mineral phases control the outcome. This situation is even more complex if CaP is precipitated in a hydrogel matrix, where one can expect the organic matrix to modulate crystallization by introducing supersaturation gradients or changing the nucleation and growth kinetics of crystals. In this study we apply a range of characterization techniques to study the mineral formation and transformations of CaP within an alginate matrix with spatiotemporal resolution. It demonstrates how a detailed investigation of the mineral precipitation and transformations can aid in the future rational design of hydrogel-based materials for bone tissue engineering and studies of biomineralization processes.

© 2016 Acta Materialia Inc. Published by Elsevier Ltd. All rights reserved.

* Corresponding author.

E-mail addresses: sindre.bjornoy@ntnu.no (S.H. Bjørnøy), david.bassett@ntnu.no (D.C. Bassett), seniz.ucar@ntnu.no (S. Ucar), berit.l.strand@ntnu.no (B.L. Strand), jens-petter.andreassen@ntnu.no (J.-P. Andreassen), pawel.sikorski@ntnu.no (P. Sikorski).

<http://dx.doi.org/10.1016/j.actbio.2016.08.041>

1742-7061/© 2016 Acta Materialia Inc. Published by Elsevier Ltd. All rights reserved.

1. Introduction

Hydrogels combined with inorganic materials are attractive candidates in the search for an injectable composite material for hard tissue regeneration. The hydrogel can be used as a carrier

material for cells, drugs or other bioactive molecules and also act as a scaffold for tissue formation [1]. The inorganic phase provides nucleation sites and the necessary ions for *in vivo* bone formation and also modifies the mechanical properties of the resulting composite material [2,3]. In cases where calcium phosphate (CaP) has been used as the inorganic phase, hydroxyapatite (HAp) has long been the material of choice due to its similarity to the mineral found in bone [4–6]. However, HAp is thermodynamically stable under *in vivo* conditions, and therefore will not readily dissolve and provide ions for bone formation. Therefore, in recent years, less stable CaP phases such as Octacalcium phosphate (OCP) and brushite (the abbreviation DCPD has been used in sample names and figure legends to indicate brushite) have attracted increasing interest in this regard [7]. These acidic phases are often present in the early stages of precipitation *in vitro*, even at mildly alkaline conditions, as they tend to nucleate more easily than HAp [8]. In the more complex *in vivo* environment, evidence of such precursors has been elusive. Whether this stems from the influence of templating molecules or is due to dehydration or other artifacts during sample preparation is not entirely clear. Peptide motifs from dentin matrix proteins have been shown to accelerate the formation of crystalline HAp *in vitro*, which supports the first scenario [9]. On the other hand, using *in situ* characterization techniques or minimal sample preparation there have been reports of several non-apatitic precursor phases during early mineralization, including amorphous phosphate (ACP) and OCP [10]. More recently, ACP has been shown to act as a precursor to HAp during osteogenesis within a ceramic tissue engineering scaffold loaded with bone marrow mesenchymal stem cells and implanted in a murine model [11]. Also, cellularly derived ACP nanospheres have been shown to transform into crystalline platelets of HA upon contact with the collagen matrix of continuously mineralizing fin bones of zebrafish [12]. Similar mineralization pathways have also been suggested for other types of biominerals, such as calcium carbonate found in sea urchins and mollusks [13].

Our group focuses on the formation of alginate–CaP composite materials by counter-diffusion in which mineral is precipitated simultaneously with hydrogel crosslinking. This approach allows control over the resulting CaP phase and has recently been investigated in particular for the formation of HAp and brushite [14,15]. In order to produce phase pure alginate–brushite composites, seed crystals were used to initiate nucleation, since conditions which normally produce brushite when precipitated in solution, resulted in HAp inside the gel network, irrespective of the precursor concentrations and initial pH [15]. Further investigation into this phenomena revealed an inhibitory effect of alginate on the growth and nucleation of brushite in the presence of small amounts of alginate [16].

A thorough understanding of CaP formation and transformation processes is essential for both fundamental studies of biomineralization and for the development of synthetic hard tissue engineering scaffold biomaterials. CaP mineralization, although dependent on reaction conditions such as pH and ionic strength, is often dictated by kinetics rather than thermodynamics. In addition, the crystallization process may be influenced by both (bio) organic molecules and spatial confinement [17–25]. This represents a particular scientific challenge, since it is difficult to precisely monitor mineralization processes *in situ*. We have recently presented a new approach that enables the correlative application of a range of characterization techniques to closely monitor crystallization processes within hydrogels [26]. Here we apply this toolbox to study the formation and transformation of CaP–mineral within an alginate matrix at low pH (approx. pH 5) and the influence of brushite seeds dispersed in the matrix under otherwise identical conditions. The non-destructive characterization techniques were also used to monitor the transformation behavior of minerals within alginate

hydrogels during incubation in simulated body fluid (SBF), providing a means to measure the same samples over several time points. This resulted in a thorough spatiotemporal description of the gel and mineral formation, maturation and transformation pathways at the microscale in unprecedented detail.

2. Experimental

2.1. Flow cell samples

De-ionized water (DIW, with a resistivity of 10–15 MΩcm) was used in all of the experiments. Alginate solutions were prepared with 1.8 mass% alginate (LF200S, $M_w = 2.74 \times 10^5$ g mol⁻¹, $F_C = 0.68$, FMC Biopolymer, Sandvika, Norway), 0.9 mass% NaCl (27810.295, VWR, Philadelphia, PA, USA) and a mixture of Na₂HPO₄·7H₂O (206515000, Thermo Fisher Scientific, Oslo, Norway) and NaH₂PO₄·2H₂O (04269, Sigma Aldrich, Oslo, Norway) to a phosphate concentration of 100 mM or 300 mM at pH 7. A 1.5 μL droplet of alginate solution was placed between two glass slides separated by 140 μm in order to produce a disc. A 1 M CaCl₂ (C8106, Sigma Aldrich, Oslo, Norway) solution buffered either at pH 5 with sodium acetate (NaAc) (A6283, Sigma Aldrich, Oslo, Norway) or at pH 7 with tris(hydroxymethyl) aminomethane (TRIS) (252859, Sigma Aldrich, Oslo, Norway) was introduced into the flow cell initiating the gelling and mineralization process as the calcium diffused into the disc. The reaction occurs in a large excess of calcium ions to ensure proper gelation of the alginate. SBF was made according to Kokubo *et al.* [27]. Samples were placed in 50 mL of SBF and the solution was replenished with fresh SBF every 24 h.

2.2. Preparation of crystals for seeding and Raman analysis

Brushite seed crystals were made by mixing 500 mL of 0.4 M Ca(NO₃)₂·4H₂O (31218, Sigma Aldrich, Oslo, Norway) and 500 mL of 0.4 M KH₂PO₄ (P3786, Sigma Aldrich, Oslo, Norway) and 26 mM KOH (221473, Sigma Aldrich, Oslo, Norway). The resulting precipitate was aged for 2 h before they were washed and filtered with DIW and ethanol. The size of the crystals was measured using a Coulter Counter Multisizer 3 (Beckman Coulter, CA, USA). The seed crystals were ground using an agate pestle and mortar in order to disrupt any aggregation and 0.2 mass% were added to alginate solutions under stirring. The solutions were left stirring for 1 h to ensure uniform distribution of the seed crystals.

OCP and HAp were made according to methods described by Elliott [28]. Briefly, OCP was made by hydrolysis of brushite crystals in 0.5 M NaAc (pH > 9) at 37 °C for 1 week. The solution was replenished daily. HAp was made by slowly dripping a solution with 640 mM Ca(NO₃)₂ into an equal volume of 250 mM (NH₄)₂HPO₄ (215996, Sigma Aldrich, Oslo, Norway) under rapid stirring. Both solutions had an initial pH above 10 and NH₄OH (221228, Sigma Aldrich, Oslo, Norway) was used to maintain pH above 10. The resulting precipitate was aged over night.

The resulting crystals were in all cases washed and filtered using DIW and ethanol and crystalline phase purity was measured using powder XRD (D8 Advance DaVinci, Bruker AXS GmbH, Karlsruhe, Germany) prior to Raman measurements, see Figs. S1–S3 in the Supplementary Information.

2.3. Characterization

Dark-field and phase contrast images of alginate samples with varying phosphate content, see Table 1, were recorded using an optical microscope (Eclipse TS100, Nikon Instruments Europe BV, Amsterdam, Netherlands) through a 4× lens at 4 FPS for the first

Table 1

An overview of the composition of the different alginate samples studied. Alginate concentration was in all cases 1.8 mass%. AlgP0 and AlgP0DCPD were not buffered.

Sample	Phosphate conc. [mM]	Initial pH	DCPD seed conc. [mass %]
AlgP0	0	~7	–
AlgP100	100	7	–
AlgP300	300	7	–
AlgP0DCPD	0	~7	0.2
AlgP300DCPD	300	7	0.2

15 s and at 0.2 FPS during the remaining gelation process. The images were analyzed with MATLAB (2014b) in order to extract the velocity at which the gel front moved, briefly a series of images of the moving gel front was recorded and the position of the front was fitted with an ellipse. A gel front radius was calculated by averaging the two ellipse axis (in all cases the shape was close to circular) and the position of the front was plotted as a function of time. The approximately linear region of the resulting plot was used to calculate the gel front velocity, cf. Fig. S4. Further details of the analysis are given elsewhere [26].

Selected samples were critical point dried (Emitech K850 critical point dryer, Quorum Technologies Ltd, East Sussex, England), mounted on aluminum stubs using carbon tape and coated with 3–5 nm platinum/palladium (Cressington 208 HR, Cressington Scientific Instruments Ltd, Watford, England) before SEM-analysis (S-5500, Hitachi, Tokyo, Japan).

Raman microspectroscopy (InVia Reflex, Renishaw, Gloucestershire, England) was performed by making 120 measurements (integration time 1 s, 30 accumulations) at one spot directly after the gelling solution had been introduced. Line scans consisting of recorded spectra (integration time 1 s, 30 accumulations) from 50 points along the radius of mineralized alginate discs were also collected 1 h and 24 h after the gelling solution had been introduced. All measurements were performed with a 535 nm laser through a 10× lens. Confocality was reduced at the expense of spatial resolution in order to obtain an average signal from the whole thickness of the disc.

By adding 20 μM R6G-EDA (rhodamine 6G modified with ethylenediamine according to published methods [29,30]) and 5 μM sulforhodamine 101 (SR101, S7635, Sigma Aldrich, Oslo, Norway) pH measurements were performed using confocal laser scanning microscopy (TCS SP5, Leica Microsystems, Wetzlar, Germany). Images were recorded at 0.1 FPS for a duration of 33 min. Details of the measurements settings and analysis are presented elsewhere [26]. Briefly, the intensity ratio between a pH-sensitive and pH-insensitive dye was compared to a standard curve made using the same measurement conditions in order to calculate the pH in each pixel of the images.

3. Results and discussion

Previously we have shown that the velocity of the alginate gel front was limited by inwards diffusion of Ca^{2+} [26]. Tanaka *et al.* have shown that the diffusion of molecules with a molecular weight lower than 2×10^4 is the same in water, as it is in gels made with 2% or 4% alginate, indicating that viscosity does not affect the diffusion of small molecules in this system [31]. With the addition of phosphate to this system, there is a simultaneous consumption of calcium ions due to precipitation of a mineral phase within the gel network. Therefore it follows that the gel front velocity is likely to reduce. To investigate this experimentally we studied the gel front evolution in our flow cell with additional phosphate present in the hydrogel phase using optical microscopy. Fig. 1a–c shows a typical phosphate containing sample during the gelation process.

Due to a difference in refractive indexes between gelled and ungelled alginate, the position of the gel front was clearly visible in phase contrast microscopy, see Fig. 1a. Using dark field microscopy, the mineralized gel was clearly visible due to the fact that it scattered more of the incoming illumination, seen in Fig. 1b and c. Fig. 1d shows a bar plot of the gel front velocities recorded for the different samples.

As expected, the gel front velocity was greatest for phosphate free samples and decreased with increasing phosphate concentration. Table 1 provides a summary of the conditions used for the different samples. An interesting characteristic of the mineralization process was observed in dark field microscopy: the leading edge of the mineralization zone contained a narrow region which scattered more light, indicated by asterisks in Fig. 1b and c. This region, appearing as a brighter band, moved inwards immediately behind the gel front as the mineralization progressed and was formed at the same time or just after influx of the Ca-ions and the resulting gelling of alginate (cf. Fig. 1b and c). This change of position indicated that the origin of this region was a metastable phase which transformed or dissolved after a relatively short time (~120 s as estimated from the images). The nature of this phase is investigated in detail below. In this geometry, supersaturation with respect to CaP was highest close to the gel front and would be quickly reduced once the mineral phase had formed. It is therefore likely that this transient zone was located close to the region with the highest supersaturation, and contained a metastable form of CaP.

We have previously shown the potent effect of brushite seed crystals on phase selection within alginate hydrogels and with the added benefit of our spatiotemporal characterization toolbox we further investigate this effect here [15]. It has previously been shown that alginate, and especially the guluronate residues (G-blocks) which have a high affinity for calcium, have an inhibitory effect on the nucleation (and growth) of calcium phosphate crystals [16]. Chelation of calcium ions is a likely explanation for the nucleation inhibition, while non-specific interactions between alginate and crystals and specific interactions between G-blocks and active growth sites are probable causes of growth inhibition. Considering this inhibitory effect of alginate on the nucleation (and growth) of calcium phosphate, as observed by us and others, we expected that the addition of seed crystals would increase the Ca^{2+} consumption rate, as it would not rely on nucleation of new crystals [16,32]. We tested this hypothesis by incorporating 0.2 mass% brushite seed crystals with an average size of 30 μm in alginate containing 300 mM phosphate precursor and monitored gel front velocity and crystal growth. For these samples, one might expect the gel front velocity to be reduced to a larger extent compared to samples without seed crystals, due to an increased consumption of Ca^{2+} . However, no significant difference was observed experimentally (Fig. 1d). A transient zone similar to the one observed for unseeded samples was also observed close to the mineral front for seeded samples, see Fig. 2. These observations indicate that a similar process was responsible for the initial reduction in the calcium and phosphate concentrations for both seeded and unseeded samples. For brevity, we term the three observed regions ungelled, transient and gelled; however, note that the transient zone has also been crosslinked and is to be considered a gelled region. Details of this transformation process focusing on phase composition, transformation kinetics and morphology of the formed mineral phases are described below.

To characterize the phase composition of the mineral formed in the experiments described above in real time, we used confocal Raman micro-spectroscopy (CRM) since this technique allows both spatial and temporal resolution of small sample volumes (typical sample volume was 1.5 μL). In addition CRM can be used, contrary

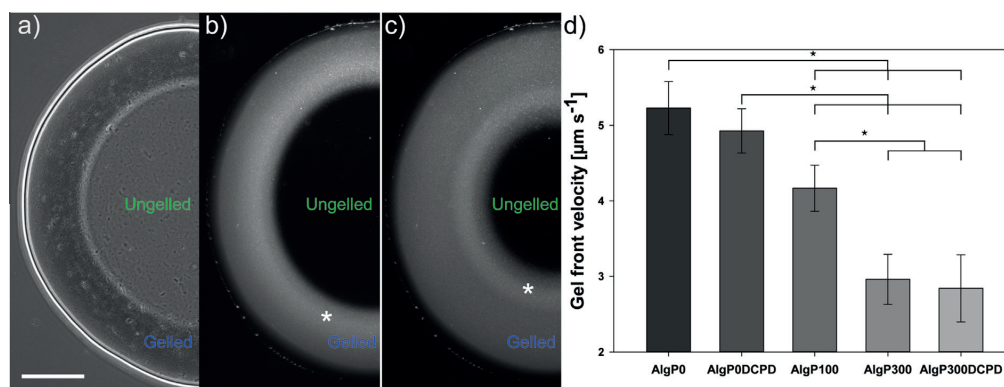


Fig. 1. (a) A phase contrast image of a partially gelled AlgP300 sample. The gel front is clearly visible between the gelled and the ungelled part. Scalebar: 500 μm . (b) A dark field micrograph showing the gelation and mineralization of an alginate disc after 150 s. (c) The same sample as in b after 300 s. A moving bright band of mineral is marked by an asterisk in b and c. (d) Bar plot of the gel front velocity as a function of phosphate concentration and the presence of brushite seeds. The asterisk marks statistically different values (One way ANOVA, $p < 0.05$).

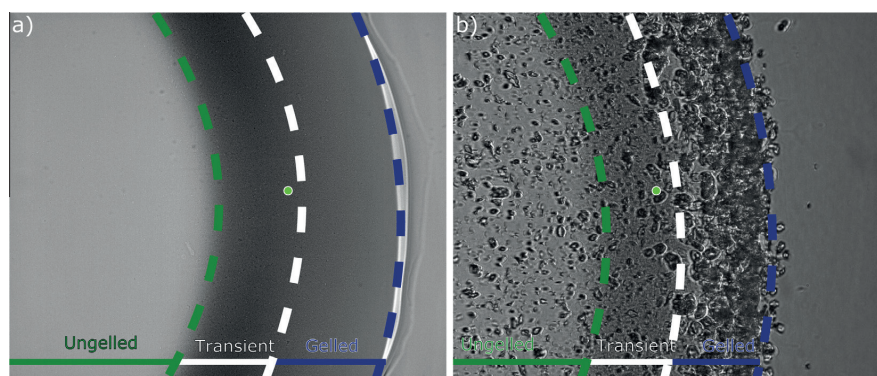


Fig. 2. Phase contrast microscopy images showing an AlgP300 (a) and an AlgP300DCPD (b) sample during the gelling process. Three regions are marked in the images: the ungelled region shown in green, the transient zone shown in white, and a gelled region shown in blue. The marker indicates the approximate position of the CRM time scan. The frame width of the images is 845 μm . (For interpretation of the references to colour in this figure legend, the reader is referred to the web version of this article.)

to IR-spectroscopy, to monitor hydrogels in their native hydrated state [33]. Initially, Raman spectra were collected from an area approximately 200 μm from the edge of the sample, as indicated in Fig. 2. 120 scans were recorded consecutively for one hour from the same location following the introduction of Ca^{2+} to allow observation of mineral evolution. Fig. 3a shows Raman spectra of an AlgP300 sample at the indicated time points. These spectra have not been normalized, and are scaled according to the measurement time. The spectrum denoted 0 s was recorded from the alginate droplet before the calcium solution had been introduced and contains four main peaks: the three peaks with highest intensity originate from the phosphate ions in the solution. The peaks at 879 cm^{-1} and 1078 cm^{-1} were assigned to symmetric stretching of $\text{P}(\text{OH})_2$ and $\text{P}=\text{O}_2$ respectively for H_2PO_4^- , while the peak at 990 cm^{-1} was due to symmetric stretching of $\text{P}=\text{O}_3$ in HPO_4^{2-} [34]. The weaker $\text{P}-\text{OH}$ stretching from this ion was found by curve fitting at 852 cm^{-1} overlapping with the 879 cm^{-1} peak from H_2PO_4^- . The weak peak located around 810–816 cm^{-1} was assigned to the alginate polymer [35]. Alginate also has a peak located at 890–892 cm^{-1} , which overlaps with one of the H_2PO_4^- peaks and could not be resolved. As calcium was introduced the HPO_4^{2-} peak intensity was quickly reduced, while the H_2PO_4^- peak intensities

were gradually reduced. We note that the transient zone did not give any strong Raman signal. However, a weak and broad peak located at 955 cm^{-1} which, over time, split into two overlapping peaks located at 946 cm^{-1} and 957 cm^{-1} was observed. The intensity of the 946 cm^{-1} peak was reduced while the 957 cm^{-1} peak increased in intensity, became sharper and shifted towards higher wavenumbers as time progressed, as shown in Fig. 3a. The appearance and reduction in intensity of this broad peak corresponded to the appearance and disappearance of the transient region observed in optical microscopy. Peak sharpening is indicative of increased crystallinity and the observed peak shift is indicative of mineral maturation similar to that which was previously observed in a bone tissue model [10]. Different literature sources report the Raman signal from amorphous calcium phosphate ACP to be a broad peak centered at 945–955 cm^{-1} [9,10,36]. Although the signal was weak, this was interpreted as an indication that the mineral in the transient region was amorphous. After 15 min a peak appeared around 928–935 which was assigned to the C–C stretching of acetate, which was due to the buffer diffusing into the hydrogel [37]. The same measurements were repeated on a similar sample infused with a TRIS-buffered Ca^{2+} solution at pH 7. The same weak ACP peak at 955 cm^{-1} was observed here without the

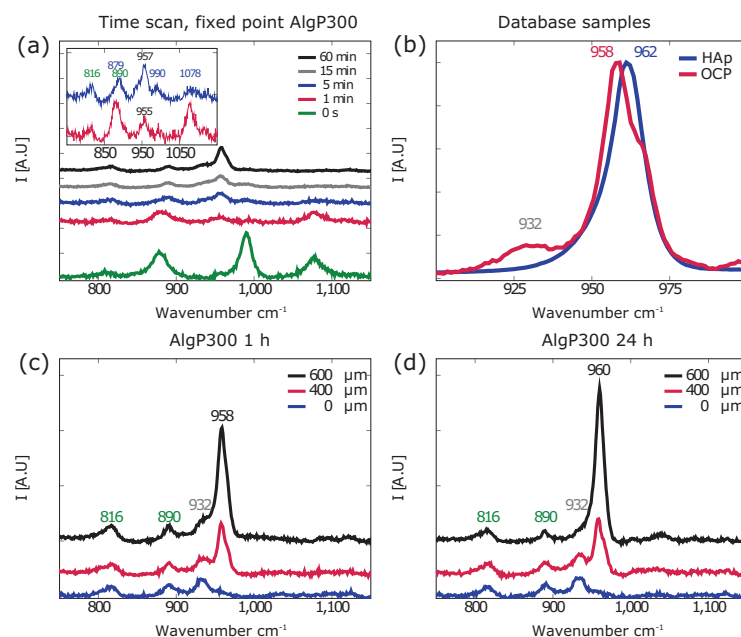


Fig. 3. (a) Raman spectra of an AlgP300 sample from a single spot at 5 time points. The inset shows the 1 min and 5 min spectra with a reduced y-axis range in order to accentuate the peaks. (b) Raman spectra from the main peak of pure phase samples of HAp and OCP prepared in solution. Note the difference in peak shape between HAp and OCP. (c) and (d) Raman spectra from a line scan of an AlgP300 sample after 1 and 24 h respectively. The spectra names refer to distance from the center of the discs. The numbers in the graph specify peak positions in cm^{-1} .

interfering acetate peak at 932 cm^{-1} , see [Supplementary Information Fig. S5b](#).

After 1 h, a line scan consisting of 50 points from the edge of the disc towards the center was recorded in order to investigate any spatial differences along the radius. The line scan was repeated over the same area after 24 h in the mother liquor. [Fig. 3c](#) and [d](#) shows Raman spectra recorded from three such points in an AlgP300 sample after 1 h and 24 h, respectively. The position of the spectra are given as a distance from the center. The phosphate in CaP-phases such as brushite, HA and tricalcium phosphate (TCP) have easily distinguishable Raman spectra [38]. However, it is more challenging to differentiate between HA and OCP. Crane *et al.* used a weak peak, arising from ν_1 HPO_4 stretching, positioned around 1010 cm^{-1} to identify OCP [10]. As a result of the experimental design in this work, the 1010 cm^{-1} peak was almost at the same level as the background noise (cf. [Supplementary Information Fig. S5a](#)), and was not deemed suitable. Instead the peak shape and position of the main phosphate peak was used to determine the dominating phase. Fowler *et al.* have thoroughly assigned the different Raman bands of OCP and show a main peak situated around $956\text{--}959\text{ cm}^{-1}$ with a strong shoulder at $966\text{--}967\text{ cm}^{-1}$, both arising from ν_1 PO_4 stretching [39]. The ν_1 PO_4 stretching of HAp is reported to be a single peak located at $959\text{--}962\text{ cm}^{-1}$ with a weak and broad shoulder at around 950 cm^{-1} leading to an asymmetric peak shape of the main phosphate peak of HAp [40]. The difference in peak shape between OCP and HAp are clearly visible in the spectra of pure phase samples shown in [Fig. 3b](#). Therefore, fitting of the recorded spectra in a region between 920 and 980 cm^{-1} was used to determine the dominating crystal phase, shown in red (OCP) and blue (HAp) in [Fig. 4](#). [Fig. 4a](#) and [b](#) shows micrographs of an AlgP300 sample after 1 h and 24 h incubation in the mother liquor. The line scans from the sample are visualized in [Fig. 4c](#) and [d](#), where the intensity of the peak located at

958 cm^{-1} (the main phosphate peak in the spectra arising from ν_1 PO_4 stretching [38]) has been plotted as a function of distance from the center for the two samples. The intensity at 987 cm^{-1} , corresponding to the main peak of brushite has also been plotted. The lines mark the position of the CRM line scans and the numbers refer to the position of SEM-images shown in [Fig. 7](#). It was found that the mineral present in the hydrogel after 1 h was mainly OCP, although a narrow band towards the edge of the disc was predominantly HAp, see [Fig. 4c](#). After storage for 24 h in the gelling solution, a more heavily mineralized band was seen in optical microscopy along the edge of the disc, see [Fig. 4b](#). The Raman intensity in the outer region of the disc and the width of the HAp dominated region had both increased compared to the 1 h sample, as shown in [Fig. 4d](#). No brushite was observed within the alginate network in these experiments, the small rise in the black curve is due to background noise.

The same set of CRM measurements was repeated for samples containing 0.2 mass% brushite seeds mixed into the alginate solution with 300 mM phosphate, denoted AlgP300DCPD. A weak broad peak located at 955 cm^{-1} was also seen for these samples, however instead of shifting towards higher wavenumbers, it disappeared as the brushite peak at 987 cm^{-1} increased in intensity, as seen in the inset of [Fig. 5a](#). The initial peak at 955 cm^{-1} was present for less than a minute, which corresponds to the appearance of the transient region observed by optical microscopy. [Fig. 5b](#) shows the Raman spectrum for a pure phase brushite sample. After 1 h and 24 h, line scans were performed. Three spectra from chosen positions at both time points are shown in [Fig. 5c](#) and [d](#). Micrographs of this sample after 1 h and 24 h incubation in the mother liquor are shown in [Fig. 6a](#) and [b](#). The intensity at 960 cm^{-1} and 987 cm^{-1} have been plotted as a function of distance from the center in [Fig. 6c](#) and [d](#). In contrast to the line scan for unseeded samples, which was relatively smooth with the Raman signal intensity

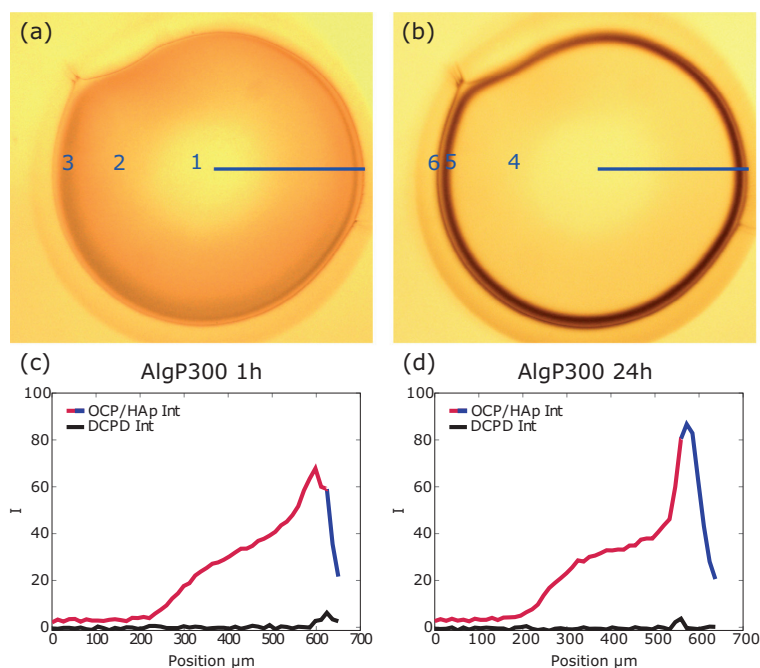


Fig. 4. Optical images and Raman data for an unseeded hydrogel disc ($\varnothing \approx 1.3$ mm) with 300 mM phosphate gelled and mineralized in a 1 M calcium solution at pH 5. (a) After 1 h in the gelling solution. (b) After 24 h in the gelling solution. The numbers correspond to positions of the SEM-images shown in Fig. 7. (c) A line scan (shown by the blue line in (a)) showing the intensity of the 958 cm^{-1} peak, corresponding to the dominant phase as determined by curve fitting, either OCP in red and HAp in blue. The intensity of the 987 cm^{-1} peak, corresponding to DCPD, is shown in black. (d) A line scan (blue line in (b)) over the same area of the same sample after 24 h in the gelling solution. (For interpretation of the references to colour in this figure legend, the reader is referred to the web version of this article.)

highest at the edge of the disc and gradually decreasing towards the center, the seeded samples resulted in a more jagged signal which persisted into the center of the disc. This was interpreted as a result of the larger brushite crystals present in the hydrogel. These crystals were larger than the laser beam spot size and more dispersed within the hydrogel network. As a result the Raman signal originating from the mineral crystals appear more discrete along the line scan for the AlgP300DCPD samples. For the AlgP300 samples, the crystals were much smaller than the spot size and a more averaged signal from both mineral and hydrogel was obtained in every point spectrum. Both optical images and CRM measurements indicated that there was less mineral towards the center, but nevertheless growth of the seeds occurred throughout the sample. A micrograph of the sample before CaCl_2 was introduced can be seen in the [Supplementary Information \(Fig. S6\)](#). A line scan was repeated in the same area following 24 h incubation in the mother liquor, seen in Fig. 6d. The brushite peak at 987 cm^{-1} disappeared towards the edge of the disc and was replaced by a peak located at 960 cm^{-1} , indicating conversion of brushite to HAp. There was no evidence in the Raman data that OCP was part of the transformation pathway when brushite had precipitated first.

To determine the crystal morphology and distribution of the mineral within the hydrogel network, selected samples were prepared for SEM-analysis. Fig. 7 shows images recorded for an AlgP300 sample kept in the gelling solution for 1 h (a–c) and for 24 h (d–f). Their corresponding positions (1 = a, 2 = b etc.) are shown in Fig. 4. Fig. 7a shows an image recorded from the center of a disc. No mineral could be seen in this area corroborating the CRM and optical microscopy results. The images in Fig. 7b and c

shows a combination of nodules intertwined with alginate fibers (black arrowheads) and flaky plate-like crystals (white arrowheads). These crystals were more numerous in Fig. 7c which was recorded at a position closer to the edge of the disc. Following storage for 24 h in the gelling solution, mineral located in the same region as Fig. 7b had grown considerably and appeared more plate-like (Fig. 7d). The Raman signal from the same region did not increase in intensity and showed no sign of peak sharpening which indicates that the amount of mineral or degree of crystallinity did not change. The larger crystals seen in Fig. 7d as compared to Fig. 7b are then likely the result of Ostwald ripening, where larger crystals have grown at the expense of smaller crystals without changing the total amount of mineral within this region. Peak fitting of the OCP dual-peak revealed that the center of the two peaks was shifted from 957 to 958 cm^{-1} and 965 to 966 cm^{-1} , respectively. The exact origin of this shift is not known, however it could be a similar maturation process as previously described for HAp [10]. The images in Fig. 7e and f, show an abundance of well formed crystals. Within the hydrogel, large platelets with feathered edges were found (Fig. 7e), contrasting to well defined acicular crystals at the outermost region of the disc (Fig. 7f). See Fig. S7 in the [Supplementary Information](#) which shows a lower magnification overview to confirm the uniform mineral distribution over the different regions. Raman spectra from these regions revealed that the mineral in Fig. 7b–d was OCP while the mineral in e and f was HAp.

Fig. 8 shows an AlgP300DCPD sample prepared at pH 5 and kept in the gelling solution for 1 h (a–c) and 24 h (d–f). For samples stored for 1 h, large brushite crystals were observed throughout the alginate matrix, as shown in Fig. 8a and b. The size of these

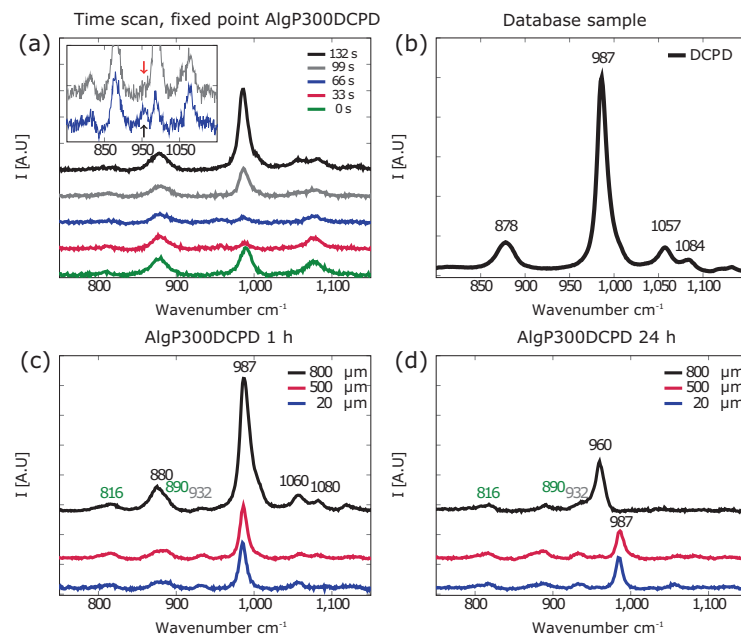


Fig. 5. (a) Raman spectra of an AlgP300DCPD sample from a single spot at 5 time points. The inset shows a close up of the 66 s and 99 s plots where a peak located at 955 cm^{-1} is visible after 66 s (black arrow) and gone after 99 s (red arrow). (b) Raman spectra of phase pure DCPD prepared in solution. (c) and (d) Raman spectra from a line scan of an AlgP300DCPD sample after 1 and 24 h respectively. (For interpretation of the references to colour in this figure legend, the reader is referred to the web version of this article.)

brushite crystals, and the absence of smaller crystals, indicated that nucleation of new crystals did not occur within the hydrogel network. This was further supported by observations described below, where the mineralization process was visualized immediately after precipitation of the mineral phase. No evidence of small brushite crystals was found and dissolution of ACP which was consumed by growth of brushite seeds was observed (cf. Fig. 9e). In addition, a dense layer of crystals on the outer surface of the disc was also present. This layer, shown in Fig. 8c was probably a result of the high supersaturation in this region, in combination with uninhibited growth into the surrounding solution. After 24 h, this surface layer was not present and the crystal structure close to the surface of the disc had changed from large brushite platelets to acicular HAp crystals similar to those observed in the same region of the AlgP300 samples, (cf. Figs. 8f and 7f). This sample fractured during mounting and the surface to the left in Fig. 8d shows a cross-section of the disc. A magnified image of this section, shown in Fig. 8e, reveals that the crystals were also needle-like further into the alginate network in contrast to unseeded samples which had platelets in the same region. This also confirms that the crystals were present throughout the thickness of the disc. CRM analysis of this region showed that these crystals were HAp.

Both optical microscopy and CRM showed that a metastable phase was present in the early stages of mineralization in the alginate discs. Based on observations from optical microscopy we estimate that, once formed, this phase was stable for no more than 120 s. In order to study the morphology of this phase, samples were kept in the gelling solution until the gel formed approximately halfway through the disc, after which they were flushed with DIW. This was immediately followed by opening the flow cells and plunging the hydrogel discs into 96% ethanol in order to prevent any dissolution or transformation of precipitated CaP phases. The samples were exposed to the gelling solution for

approximately 3 min, leaving three distinct regions corresponding to the regions shown in Fig. 2. Fig. 9a–c shows an AlgP300 sample prepared at pH 5 and arrested after 3 min reaction time. In the overview image (Fig. 9a) the gelled region, transient region and ungelled region are marked with the same colors as in Fig. 2. The image in Fig. 9b was recorded within the gelled region, nodules and flaky crystals similar to the ones observed for 1 h samples were present (cf. Fig. 7b). The transient region, shown in Fig. 9c contained spherical particles with a size range between 30 and 400 nm. These particles were uniformly distributed within the alginate network. Several nodules, intimately connected with alginate fibers, were also observed in this region. These nodules were larger and less numerous than the spherical particles which suggests that the transformation of the spherical particles into nodules and later flaky platelets is solution based and not a solid state transformation.

Fig. 9d–f shows an AlgP300DCPD sample prepared at pH 5 and arrested after 3 min reaction time. Spherical particles were also observed for this sample in the transient zone (marked white in Fig. 9d). 9e shows a brushite seed crystal located in the transient zone. The spherical particles were not observed in the immediate vicinity of this seed, shown at higher magnification in Fig. 9f. In the gelled region, (marked blue in Fig. 9d), no spherical particles were observed and an abundance of brushite crystals (size range 20–80 μm) could be seen within the hydrogel, similar to those observed by optical microscopy. The absence of spherical particles in the gelled region, and the consumption of these particles around the brushite seeds indicated that they consisted of a metastable phase which appeared to reprecipitate into growing DCPD crystals. This is consistent with CRM observations. The SEM observations are strong indications that this transformation happens via a dissolution–recrystallization process.

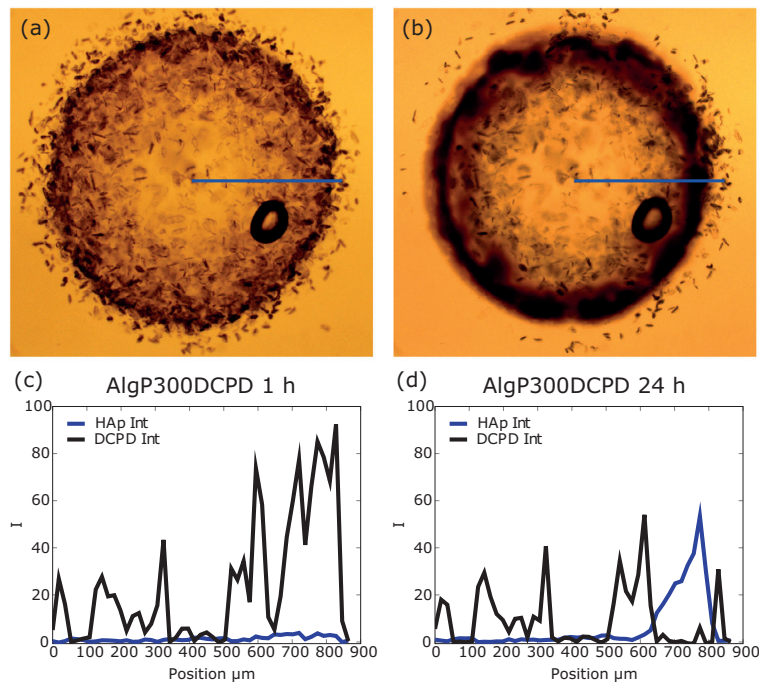


Fig. 6. Optical images and Raman data for an AlgP300DCPD hydrogel disc ($\phi \approx 1.6$ mm) gelled and mineralized in a 1 M calcium solution at pH 5. (a) After 1 h in the gelling solution. (b) After 24 h in the gelling solution. (c) A line scan (shown by the blue line in (a)) with the intensity of the 960 cm^{-1} peak corresponding to HAp shown in blue and the intensity of the 987 cm^{-1} peak, corresponding to DCPD, is shown in black. (d) A line scan of the same sample after 24 h in the gelling solution. (For interpretation of the references to colour in this figure legend, the reader is referred to the web version of this article.)

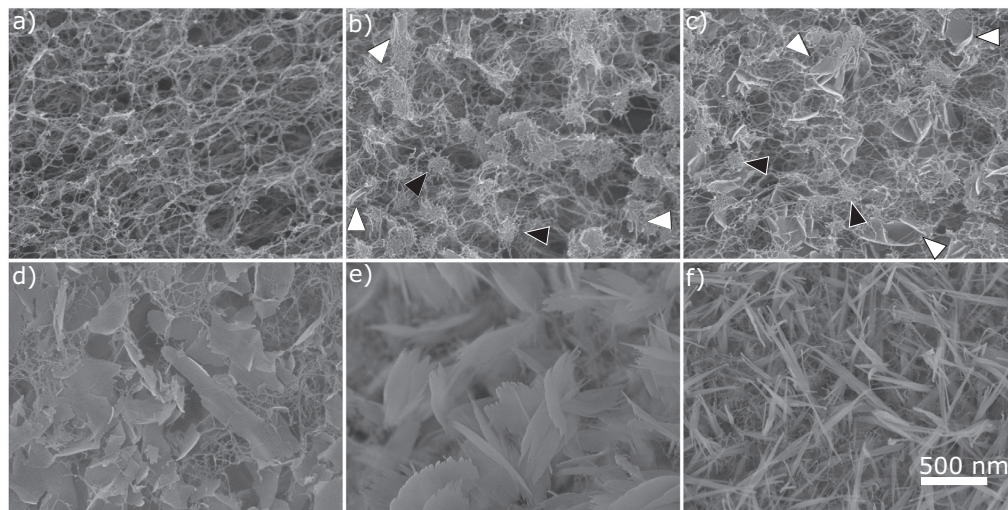


Fig. 7. SEM-images of an AlgP300 sample gelled and mineralized in a 1 M CaCl_2 solution at pH 5. (a), (b) and (c) are recorded from a sample incubated in the gelling solution for 1 h, while (d), (e) and (f) are recorded from a sample incubated in the gelling solution for 24 h. Black arrowheads indicate to selected alginate/mineral nodules. White arrowheads indicate selected flaky plate like crystals. The scale bar applies to all of the images in this figure.

Fig. 9g–i shows magnified images of spherical particles found in the transient region of an AlgP300DCPD sample prepared at pH 5 (g), an AlgP300 sample prepared at pH 5 (h) and an AlgP300 sam-

ple prepared at pH 7 (i). The spherical particles had a non-uniform diameter ranging from 30 to 400 nm and appeared identical regardless of the initial conditions in which they were made. Elliott

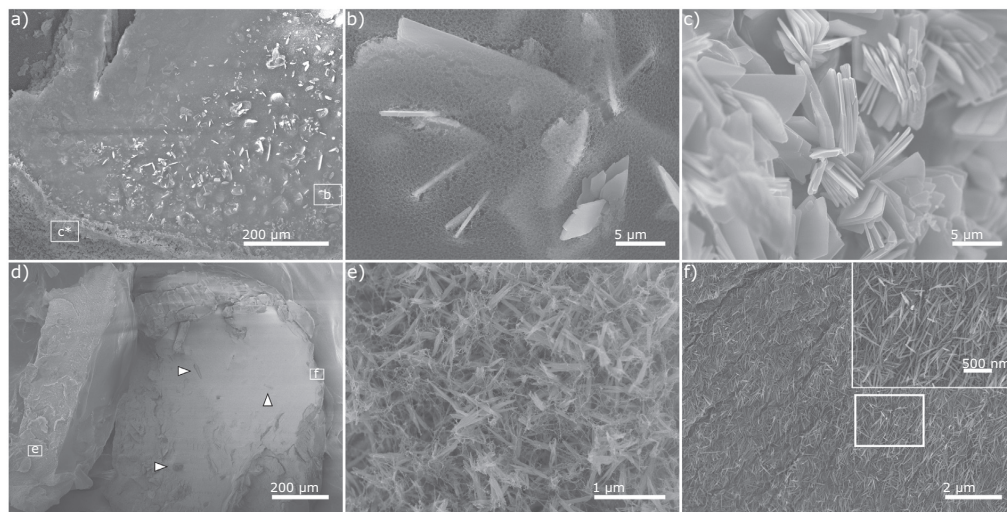


Fig. 8. SEM-images of an AlgP300DCPD sample gelled and mineralized in a 1 M calcium solution at pH 5. The sample shown in (a), (b) and (c) was incubated in the gelling solution for 1 h and shows large brushite crystals within the alginate network and a dense layer of crystals at the surface, seen in (c). The sample shown in (d) (this image is a collage of two separate images), (e) and (f) was incubated in the gelling solution for 24 h and shows a few remaining brushite crystals marked with white arrowheads and acicular HAp crystals within the alginate network. White boxes show the position of higher magnification images. The asterisk denotes the image was from a similar region in the sample geometry.

reports that ACP is often present as spherical particles in the range of 20–120 nm, which fits well with our conclusion that these particles are ACP [28]. The SEM analysis in combination with CRM suggests that ACP was formed initially which then rapidly transformed into OCP or HAp for unseeded samples and into brushite for samples seeded with brushite crystals. In both cases transformation into the more stable HAp phase occurred gradually and all transformations were likely to have taken place via a dissolution–reprecipitation process.

pH is an important factor in determining nucleation and growth of different CaP-phases [41]. In solution, ions diffuse readily and the pH can be expected to be uniform throughout the sample volume. The situation was somewhat more complex within the system studied in this work. The alginate was initially buffered at pH 7, and the gelling solution was buffered at pH 5 or pH 7 and as CaP precipitated, H^+ was released locally. In order to gain information regarding the dynamics of the pH in the system, optical measurements with a pH-sensitive dye were performed. We have previously shown this method to be highly sensitive to changes in pH between 4 and 6.5 [26]. Fig. 10a shows the pH value for three different samples averaged from a $121 \times 121 \mu m$ area in the center of the alginate discs as a function of time from when the gelling solution was introduced. The measurements show a local generation of H^+ at the mineralization front which consequently diffused inwards to the center of the disc and outwards into the surrounding solution. This can be seen in Fig. 10b and c where a reduction in pH was observed both in the center of the discs and in the surrounding solution. In the sample subjected to a calcium solution of pH 5, part of the decrease in pH is due to the inwards diffusion of the acidic calcium solution. However, the similarity in the shape of the curves in Fig. 10a indicates that the generation of H^+ is the main reason for the change in pH regardless of the initial pH in the gelling solution. In addition, careful examination of the curve denoted AlgP300 pH5 edge in Fig. 10b reveals a slight u-shape. This u-shape is more clear in Fig. 10c, where both the alginate solution and the calcium solution was initially pH 7. In this case, the only source of H^+ was the precipitation of CaP. This shape indicates

the outward diffusion of H^+ generated from the mineral formation. It can be seen that the surrounding calcium solution experienced a reduction in pH as the local generation of H^+ exceeded the buffering capacity. A subsequent increase in pH occurred as the solution regained its buffering capacity due to its comparatively larger volume. In both cases the pH in the center and at the halfway point are expected, with time, to reach the same pH-value of the surrounding solution.

As seen in Fig. 10a, the pH in the center of the discs changed most within 150–350 s after the introduction of the gelling solution. The results from the SEM and CRM analysis show that ACP is the dominant mineral phase within this time frame. This suggests that formation of ACP is the main cause of H^+ release. The subsequent transformation into OCP or brushite appear to have occurred under similar conditions, i.e. pH < 5, for all sample types as can be seen from the similar shape of the curves in Fig. 10a. In cases where brushite seeds were present, the amorphous phase was then consumed due to growth of brushite crystals, likely via a dissolution–reprecipitation pathway. For unseeded samples, consumption of the amorphous phase occurred via nucleation and growth of OCP at the same pH-conditions as for the seeded samples. It is likely that the alginate inhibited the nucleation of brushite, as one would expect this phase to nucleate at a pH-value less than 5 [16,41]. As some of the phosphate was consumed in the mineralization process, the buffering capacity of the alginate solution was reduced. Due to the local generation and fast diffusion of H^+ , the central region of the disc experienced the lowest recorded pH, as can be observed in Fig. 10b and c. Due to a lower concentration of buffer in the surrounding solution, the diffusion of the buffer was slower than the mineral front, leading to a prolonged duration of reduced pH in the center of the discs, see Fig. S10 in the Supplementary Information for a brief discussion of this effect. We speculate that not only the consumption of the available phosphate in the sample, but also a reduction in pH led to the unmineralized zone in the center of gelled discs. This is because pH is an effective variable on supersaturation and reduced pH would lead to lower supersaturation which in turn results in reduced

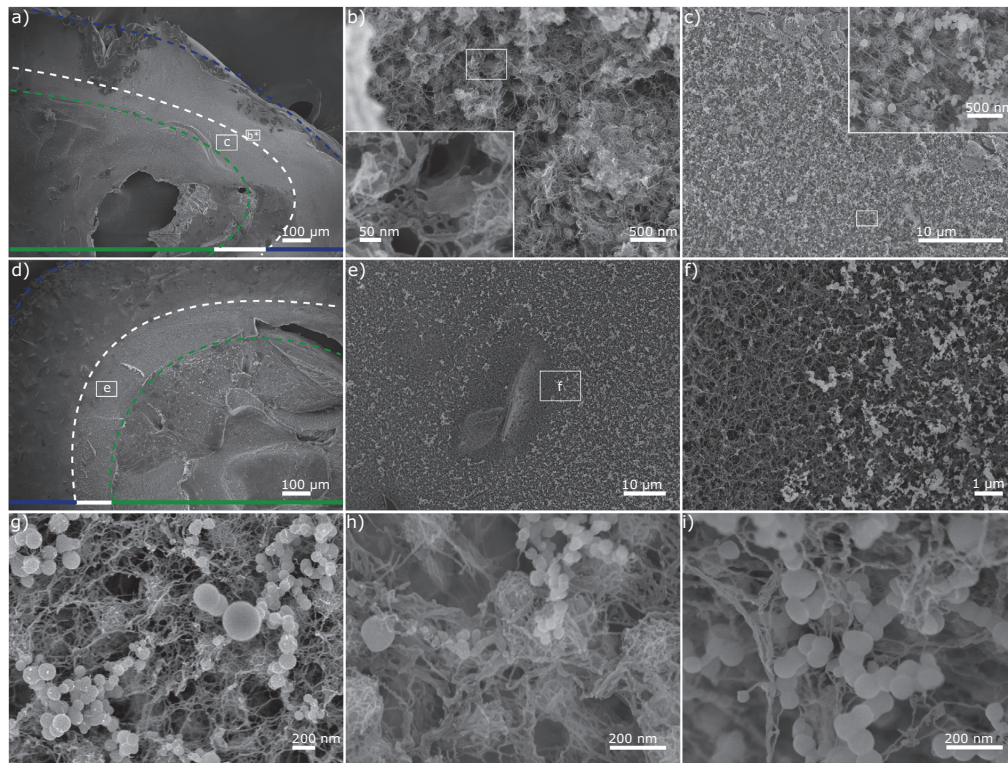


Fig. 9. SEM images of an AlgP300 sample ((a), (b), (c), (h) and (i)) and an AlgP300DCPD sample ((d), (e), (f) and (g)) gelled at pH 5 and arrested after 3 min reaction time. The image in (a) shows a low magnification overview with the gelled, transient and ungelled regions marked with blue, white and green respectively. (b) and (c) are higher magnification images from the gelled and transient regions respectively. (d) is a low magnification overview of a seeded sample with similar regions marked as in (a). (e) and (f) are magnified images of an area surrounding a seed, showing how the metastable phase has been consumed by the crystal seed. Images (g) (AlgP300DCPD made at pH 5), (h) (AlgP300 made at pH 5) and (i) (AlgP300 made at pH 7) show similar morphologies of particles found in the transient zone of samples made under different conditions. White boxes show the position of higher magnification images. The asterisk denotes the image was from a similar region in the sample geometry. (For interpretation of the references to colour in this figure legend, the reader is referred to the web version of this article.)

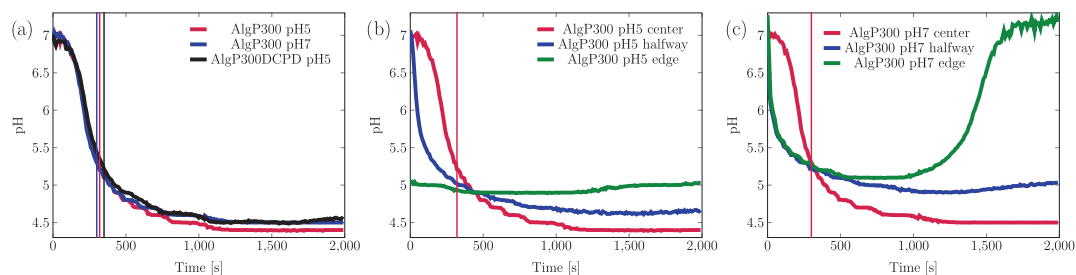


Fig. 10. (a) pH-data gathered from a $121 \times 121 \mu\text{m}$ square in the center of discs produced under three different conditions (given in the legend). The vertical lines mark the time point at which the samples were gelled, as determined by optical microscopy. The graphs in (b) and (c) show AlgP300 samples subjected to gelling solution of pH 5 and pH 7 respectively. The pH value was recorded (also $121 \times 121 \mu\text{m}$ area averages) over time from 3 positions; at the edge close to the surrounding solution, at a point halfway into the disc and from the center. It can be seen in both conditions that the surrounding solution experiences a drop in pH followed by an increase back to the initial buffered pH. This phenomenon is more obvious in (c).

nucleation of new crystals. This may also explain why in seeded samples crystals grew throughout the geometry (cf. Figs. 6 and S9) since this process was not dependent on nucleation.

Incubating materials in simulated body fluid (SBF) has previously been used to indicate the ability of samples to nucleate

HAP in physiological conditions [27]. The relevance of this incubation to predict *in vivo* behavior is a matter of debate [42]. In particular, there have been investigations with both false positives and false negatives, leaving no definitive trend [43]. However, the method is also often used to form an apatite layer on synthetic

scaffold which is believed to enhance the bone bonding ability of the implant [2,44–46,21]. In this work, it was used to study how the incorporation of CaP in the alginate matrix affected the formation of HAp, and demonstrate the ability to monitor this transformation with spatiotemporal resolution, not to predict an *in vivo* response. AlgP300DCPD samples were examined with CRM (shown in Supplementary Information, Fig. S9) and SEM as prepared (Fig. 11a–c) and following 24 h (Fig. 11d–f) and 168 h (Fig. 11g–i) incubation in SBF. As a control, alginate samples which contained brushite seeds, but no phosphate precursor, were also incubated and analyzed with CRM. For the mineralized samples, a large number of brushite crystals were observed to be protruding out from the hydrogel surface initially, as shown in Fig. 11a. Fig. 11b shows a region close to the edge of the sample where a shell of large brushite crystals could be observed along the edge and individual crystals were also observed embedded in the alginate network. Fig. 11c shows brushite crystals from a region nearer the center of the disc, revealing that large crystals were also present in this region, in contrast to the unseeded samples (cf. Fig. 7a). Following 24 h incubation in SBF there was a reduction in the abundance of large brushite crystals in all areas of the sample (Fig. 11d). A dense band of small plate like aggregated crystals had formed from the edge and 100–200 μm towards the center of the disc (Fig. 11e). As shown in Fig. 11f, some of the individual brushite crystals had

these new crystals encrusted directly on their surfaces. The new crystalline phase was confirmed to be HAp with CRM (see Fig. S9 in Supplementary Information). The dense layer of brushite crystals at the periphery of the sample had completely transformed into HAp, however the micro-scale morphology of these crystals was still intact (see Fig. S8). Following one week storage in SBF, all of the large brushite crystals within the alginate network had dissolved (Fig. 11g) and a dense shell of HAp had formed along the edge of the disc (Fig. 11h). This shell extended ca. 200 μm towards the center of the disc (Fig. 11g), and the alginate network was heavily mineralized throughout the thickness of the disc (observed from samples which fractured during preparation). Fig. 11h and i clearly demonstrates that HAp formed uniformly along the edge of the disc and non-uniformly at the location of brushite crystals further into the disc. This indicated that the source of HAp formation was driven by both dissolution of brushite crystals and inwards diffusion of the SBF-solution along the edge while further into the disc, the primary source for HAp nucleation and growth was the dissolution of the resident brushite crystals. The non-mineralized control samples did not show any HAp formation within the alginate network, however after 1 week of incubation, some HAp had formed on the interface between the hydrogel and the surrounding solution (see Fig. S9). This shows that the mineralized hydrogel promotes the formation of HAp at

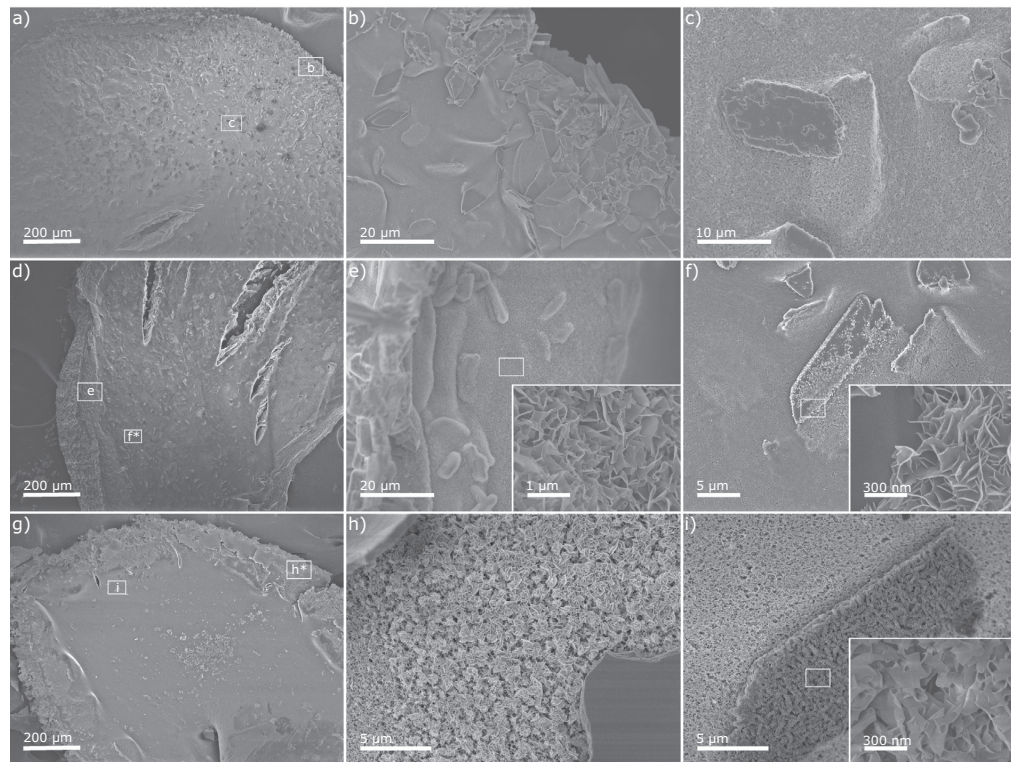


Fig. 11. SEM images of an AlgP300DCPD sample after 0 h (a–c), 24 h (d–f) and 168 h (g–i) incubation in SBF. (a), (d) and (g) show a low magnification overview images at the different time points. White boxes show the position of higher magnification images. The asterisk denotes the image was from a similar region in the sample geometry. (b) shows the extensive growth of brushite crystals along the edge of a disc. (c) shows a higher magnification image of brushite crystals present further into the disc. (e) shows a region close to the edge of a disc where a uniform region of flaky HAp crystals (a high magnification image can be seen in the inset) is visible as well as areas where the morphology of previous brushite crystals that have been converted into HAp. (f) shows the nucleation of HAp (seen as flaky crystals in the high magnification inset) close to and on the surface of a brushite crystal after 24 h incubation. (h) shows a region close to edge after 168 h incubation where a uniform band of flaky HAp crystals could be seen. (i) shows nanocrystals which have assumed the morphology of an initial brushite crystal.

physiological pH, probably due to an increased, localized supersaturation provided by the dissolution of brushite.

4. Conclusion

In summary, we have shown that by combining a simple experimental design with several correlative advanced characterization techniques, new insight into the mineralization processes within hydrogels can be obtained. Simultaneous gelling and mineralization of an alginate hydrogel was performed and spatiotemporally monitored using a thin disc geometry that was particularly convenient for optical based *in situ* characterization techniques. At high supersaturation, crystal seeds do not affect the initial nucleation of ACP, but merely directs the reprecipitation as the ACP dissolves in the dynamic system, i.e. reduced pH as shown by measurements and reduced supersaturation due to consumption of precursors. We have also conclusively discriminated between HAp and OCP via peak fitting of the ν_1 PO₄ stretch in the Raman spectrum, and shown that this can be monitored *in situ* in the hydrogel matrix used herein. Transformation of brushite into HAp following incubation in SBF was also monitored, thereby demonstrating utility of this characterization toolbox for non-destructive, *in situ* evaluation of hydrogel based hard tissue scaffold biomaterials.

Acknowledgement

The authors thank the Research Council of Norway for financial support (FRINATEK project 214607).

Appendix A. Supplementary data

Supplementary data associated with this article can be found, in the online version, at <http://dx.doi.org/10.1016/j.actbio.2016.08.041>.

References

- [1] S. Van Vlierberghe, P. Dubruel, E. Schacht, Biopolymer-based hydrogels as scaffolds for tissue engineering applications: a review, *Biomacromolecules* 12 (5) (2011) 1387–1408, <http://dx.doi.org/10.1021/bm200083n>.
- [2] K. Gkioni, S.C. Leeuwenburgh, T.E. Douglas, A.G. Mikos, J.A. Jansen, Mineralization of hydrogels for bone regeneration, *Tissue Eng. B Rev.* 16 (6) (2010) 577–585, <http://dx.doi.org/10.1089/ten.teb.2010.0462>.
- [3] A.K. Gaharwar, N.A. Peppas, A. Khademhosseini, Nanocomposite hydrogels for biomedical applications, *Biotechnol. Bioeng.* 111 (3) (2014) 441–453, <http://dx.doi.org/10.1002/bit.25160>.
- [4] H.-R. Lin, Y.-J. Yeh, Porous alginate/hydroxyapatite composite scaffolds for bone tissue engineering: preparation, characterization, and *in vitro* studies, *J. Biomed. Mater. Res. B Appl. Biomater.* 71 (1) (2004) 52–65, <http://dx.doi.org/10.1002/jbm.b.30065>.
- [5] M. Rajkumar, N. Meenakshisundaram, V. Rajendran, Development of nanocomposites based on hydroxyapatite/sodium alginate: synthesis and characterization, *Mater. Characterizat.* 62 (5) (2011) 469–479, <http://dx.doi.org/10.1016/j.matchar.2011.02.008>.
- [6] Z. Li, Y. Su, B. Xie, H. Wang, T. Wen, C. He, H. Shen, D. Wu, D. Wang, A tough hydrogel/hydroxyapatite bone-like composite fabricated *in situ* by the electrophoresis approach, *J. Mater. Chem. B* 1 (12) (2013) 1755, <http://dx.doi.org/10.1039/c3tb00246b>.
- [7] M.S. Johnsson, G.H. Nancollas, The role of brushite and octacalcium phosphate in apatite formation, *Crit. Rev. Oral Biol. Med.* 3 (1) (1992) 61–82, <http://dx.doi.org/10.1177/10454411920030010601>.
- [8] R. Boistelle, I. Lopez-Valero, Growth units and nucleation: the case of calcium phosphates, *J. Cryst. Growth* 102 (3) (1990) 609–617, [http://dx.doi.org/10.1016/0022-0248\(90\)90420-P](http://dx.doi.org/10.1016/0022-0248(90)90420-P).
- [9] T. Tsuji, K. Onuma, A. Yamamoto, M. Iijima, K. Shiba, Direct transformation from amorphous to crystalline calcium phosphate facilitated by motif-programmed artificial proteins, *Proc. Natl. Acad. Sci. U.S.A.* 105 (44) (2008) 16866–16870, <http://dx.doi.org/10.1073/pnas.0804277105>.
- [10] N.J. Crane, V. Popescu, M.D. Morris, P. Steenhuis, M.A. Ignelzi, Raman spectroscopic evidence for octacalcium phosphate and other transient mineral species deposited during intramembranous mineralization, *Bone* 39 (3) (2006) 434–442, <http://dx.doi.org/10.1016/j.bone.2006.02.059>.
- [11] G. Campi, A. Ricci, A. Guagliardi, C. Giannini, S. Lagomarsino, R. Cancedda, M. Mastrogiacomo, A. Cedola, Early stage mineralization in tissue engineering mapped by high resolution X-ray microdiffraction, *Acta biomater.* 8 (9) (2012) 3411–3418, <http://dx.doi.org/10.1016/j.actbio.2012.05.034>.
- [12] J. Mahamid, B. Aichmayer, E. Shimoni, R. Ziblat, C. Li, S. Siegel, O. Paris, P. Fratzl, S. Weiner, L. Addadi, Mapping amorphous calcium phosphate transformation into crystalline mineral from the cell to the bone in zebrafish fin rays, *Proc. Natl. Acad. Sci. U.S.A.* 107 (14) (2010) 6316–6321, <http://dx.doi.org/10.1073/pnas.0914218107>.
- [13] L.B. Gower, Biomimetic model systems for investigating the amorphous precursor pathway and its role in biomineralization, *Chem. Rev.* 108 (11) (2008) 4551–4627, <http://dx.doi.org/10.1021/cr800443h>.
- [14] M. Xie, M.O. Olderøy, J.P. Andreassen, S.M. Selbach, B.L. Strand, P. Sikorski, Alginate-controlled formation of nanoscale calcium carbonate and hydroxyapatite mineral phase within hydrogel networks, *Acta Biomater.* 6 (9) (2010) 3665–3675, <http://dx.doi.org/10.1016/j.actbio.2010.03.034>.
- [15] S.H. Bjørnøy, D.C. Bassett, S. Ucar, J.-P. Andreassen, P. Sikorski, Controlled mineralisation and recrystallisation of brushite within alginate hydrogels, *Biomed. Mater.* (2016) 015013, <http://dx.doi.org/10.1088/1748-6041/11/1/015013>.
- [16] S. Ucar, S.H. Bjørnøy, D.C. Bassett, B.L. Strand, P. Sikorski, J.-P. Andreassen, Nucleation and growth of brushite in the presence of alginate, *Cryst. Growth Des.* (2015), <http://dx.doi.org/10.1021/acs.cgd.5b01032>.
- [17] L. Gower, D. Tirrell, Calcium carbonate films and helices grown in solutions of poly(aspartate), *J. Cryst. Growth* 191 (1–2) (1998) 153–160, [http://dx.doi.org/10.1016/S0022-0248\(98\)00002-5](http://dx.doi.org/10.1016/S0022-0248(98)00002-5).
- [18] H. Colfen, S. Mann, Higher-order organization by mesoscale self-assembly and transformation of hybrid nanostructures, *Angew. Chem. Int. Ed.* 42 (21) (2003) 2350–2365, <http://dx.doi.org/10.1002/anie.200200562>.
- [19] F.C. Meldrum, H. Colfen, Controlling mineral morphologies and structures in biological and synthetic systems, *Chem. Rev.* 108 (11) (2008) 4332–4432, <http://dx.doi.org/10.1021/cr8002856>.
- [20] F. Nudelman, K. Pieterse, A. George, P.H.H. Bomans, H. Friedrich, L.J. Brylka, P.A.J. Hilbers, G. de With, N.A.J.M. Sommerdijk, The role of collagen in bone apatite formation in the presence of hydroxyapatite nucleation inhibitors, *Nat. Mater.* 9 (12) (2010) 1004–1009, <http://dx.doi.org/10.1038/nmat2875>.
- [21] K. Bleek, A. Taubert, New developments in polymer-controlled, bioinspired calcium phosphate mineralization from aqueous solution, *Acta Biomater.* 9 (5) (2013) 6283–6321, <http://dx.doi.org/10.1016/j.actbio.2012.12.027>.
- [22] H. Ping, H. Xie, B.-L. Su, Y.-B. Cheng, W. Wang, H. Wang, Y. Wang, J. Zhang, F. Zhang, Z. Fu, Organized intrabifibrillar mineralization, directed by a rationally designed multi-functional protein, *J. Mater. Chem. B* 3 (2015) 4496–4502, <http://dx.doi.org/10.1039/C5TB00386E>.
- [23] B. Cantaert, E. Beniash, F.C. Meldrum, Nanoscale confinement controls the crystallization of calcium phosphate: relevance to bone formation, *Chemistry (Weinheim an der Bergstrasse, Germany)* 19 (44) (2013) 14918–14924, <http://dx.doi.org/10.1002/chem.201302835>.
- [24] Y.-W. Wang, H.K. Christenson, F.C. Meldrum, Confinement increases the lifetimes of hydroxyapatite precursors, *Chem. Mater.* 26 (20) (2014) 5830–5838, <http://dx.doi.org/10.1021/cm501770r>.
- [25] A.K. Rajasekharan, M. Andersson, Role of Nanoscale confinement on calcium phosphate formation at high supersaturation, *Cryst. Growth Des.* 15 (6) (2015) 2775–2780, <http://dx.doi.org/10.1021/acs.cgd.5b00139>.
- [26] S.H. Bjørnøy, S. Mandaric, D.C. Bassett, A.K.O. Åslund, S. Ucar, J.-P. Andreassen, B.L. Strand, P. Sikorski, Gelling kinetics and *in situ* mineralization of alginate hydrogels: A correlative spatiotemporal characterization toolbox, *Acta Biomater.* 44 (2016) 243–253, <http://dx.doi.org/10.1016/j.actbio.2016.07.046>.
- [27] T. Kokubo, H. Takadama, How useful is SBF in predicting *in vivo* bone bioactivity?, *Biomaterials* 27 (15) (2006) 2907–2915, <http://dx.doi.org/10.1016/j.biomaterials.2006.01.017>.
- [28] J. Elliott, Structure and Chemistry of the Apatites and Other Calcium Orthophosphates, Elsevier B.V., 1994, <http://dx.doi.org/10.1016/B978-0-444-81582-8.50001-8>.
- [29] J.-S. Wu, I.-C. Hwang, K.S. Kim, J.S. Kim, Rhodamine-based Hg²⁺-selective chemodosimeter in aqueous solution: fluorescent OFF-ON, *Org. Lett.* 9 (5) (2007) 907–910, <http://dx.doi.org/10.1021/ol070109c>.
- [30] Z. Li, S. Wu, J. Han, S. Han, Imaging of intracellular acidic compartments with a sensitive rhodamine based fluorogenic pH sensor, *The Analyst* 136 (2011) 3698–3706, <http://dx.doi.org/10.1039/c1an15108h>.
- [31] H. Tanaka, M. Matsumura, I.A. Veliky, Diffusion characteristics of substrates in Ca-alginate gel beads, *Biotechnol. Bioeng.* 26 (1) (1984) 53–58, <http://dx.doi.org/10.1002/bit.260260111>.
- [32] P. Malkaj, E. Pierri, E. Dalas, The crystallization of hydroxyapatite in the presence of sodium alginate, *J. Mater. Sci. Mater. Med.* 16 (8) (2005) 733–737, <http://dx.doi.org/10.1007/s10856-005-2610-9>.
- [33] S. Koburger, A. Bannerman, L.M. Grover, F.A. Müller, J. Bowen, J.Z. Paxton, A novel method for monitoring mineralisation in hydrogels at the engineered hardsoft tissue interface, *Biomater. Sci.* 2 (1) (2014) 41, <http://dx.doi.org/10.1039/c3bm60102a>.
- [34] W.L. Marshall, G.M. Begun, Raman spectroscopy of aqueous phosphate solutions at temperatures up to 450 °C: Two liquid phases, supercritical fluids, and pyro- to ortho-phosphate conversions, *J. Chem. Soc. Faraday Trans. 2* 85 (12) (1989) 1963, <http://dx.doi.org/10.1039/f29898501963>.
- [35] M.M. Campos-Vallette, N.P. Chandra, E. Clavijo, D. Leal, B. Matsuhito, I.O. Osorio-Román, S. Torres, Characterization of sodium alginate and its block fractions by surface-enhanced Raman spectroscopy, *J. Raman Spectrosc.* (2009), <http://dx.doi.org/10.1002/jrs.2517>.

- [36] G.R. Sauer, W.B. Zunic, J.R. Durig, R.E. Wuthier, Fourier transform raman spectroscopy of synthetic and biological calcium phosphates, *Calcified Tissue Int.* 54 (5) (1994) 414–420, <http://dx.doi.org/10.1007/BF00305529>.
- [37] W.W. Rudolph, D. Fischer, G. Irmer, Vibrational spectroscopic studies and DFT calculations on NaCH_3CO_2 (aq) and CH_3COOH (aq), *Dalton Trans.* 43 (8) (2014) 3174–3185, <http://dx.doi.org/10.1039/C3DT52580E>.
- [38] S. Koutsopoulos, Synthesis and characterization of hydroxyapatite crystals: a review study on the analytical methods, *J. Biomed. Mater. Res.* 62 (4) (2002) 600–612, <http://dx.doi.org/10.1002/jbm.10280>.
- [39] B.O. Fowler, M. Markovic, W.E. Brown, Octacalcium phosphate. 3. Infrared and Raman vibrational spectra, *Chem. Mater.* 5 (10) (1993) 1417–1423, <http://dx.doi.org/10.1021/cm00034a009>.
- [40] G. Penel, G. Leroy, C. Rey, E. Bres, MicroRaman spectral study of the PO_4 and CO_3 vibrational modes in synthetic and biological apatites, *Calcified Tissue Int.* 63 (6) (1998) 475–481, <http://dx.doi.org/10.1007/s002239900561>.
- [41] F. Abbona, H. Madsen, R. Boistelle, The initial phases of calcium and magnesium phosphates precipitated from solutions of high to medium concentrations, *J. Cryst. Growth* 74 (3) (1986) 581–590, [http://dx.doi.org/10.1016/0022-0248\(86\)90205-8](http://dx.doi.org/10.1016/0022-0248(86)90205-8).
- [42] M. Bohner, J. Lemaitre, Can bioactivity be tested in vitro with SBF solution?, *Biomaterials* 30 (12) (2009) 2175–2179, <http://dxdoi.org/10.1016/j.biomaterials.2009.01.008>.
- [43] A.A. Zadpoor, Relationship between in vitro apatite-forming ability measured using simulated body fluid and in vivo bioactivity of biomaterials, *Mater. Sci. Eng. C Mater. Biol. Appl.* 35 (2014) 134–143, <http://dx.doi.org/10.1016/j.mSection.10.026>.
- [44] L. Jongpaiboonkit, T. Franklin-Ford, W.L. Murphy, Growth of hydroxyapatite coatings on biodegradable polymer microspheres, *ACS Appl. Mater. Interfaces* 1 (7) (2009) 1504–1511, <http://dx.doi.org/10.1021/am9001716>.
- [45] I. Hofmann, L. Müller, P. Greil, F.A. Müller, Calcium phosphate nucleation on cellulose fabrics, *Surf. Coatings Technol.* 201 (6) (2006) 2392–2398, <http://dx.doi.org/10.1016/j.surfcoat.2006.04.007>.
- [46] K. Rodríguez, S. Renneckar, P. Gatenholm, Biomimetic calcium phosphate crystal mineralization on electrospun cellulose-based scaffolds, *ACS Appl. Mater. Interfaces* 3 (3) (2011) 681–689, <http://dx.doi.org/10.1021/am100972r>.

Supplementary Information for: A correlative
spatiotemporal microscale study of calcium phosphate
formation and transformation within an alginate
hydrogel matrix

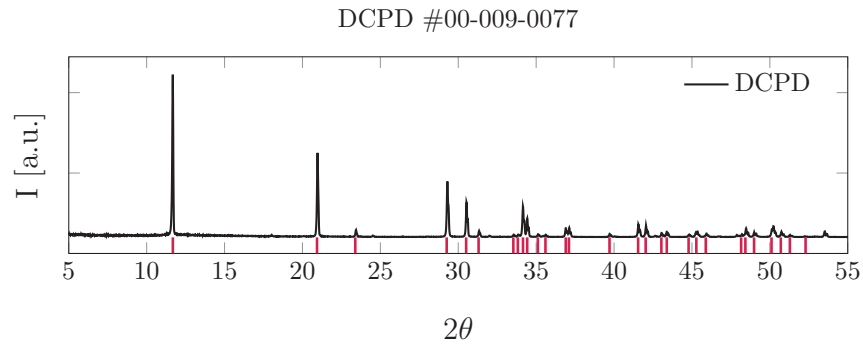


Figure S.1: The XRD-spectrum of the brushite crystals used for seeding and Raman database sample. ICDD pdf-card 00-009-0077 has been used to identify the crystal structure (shown in red lines). Reflections with less than 3 % relative intensity has been removed for clarity.

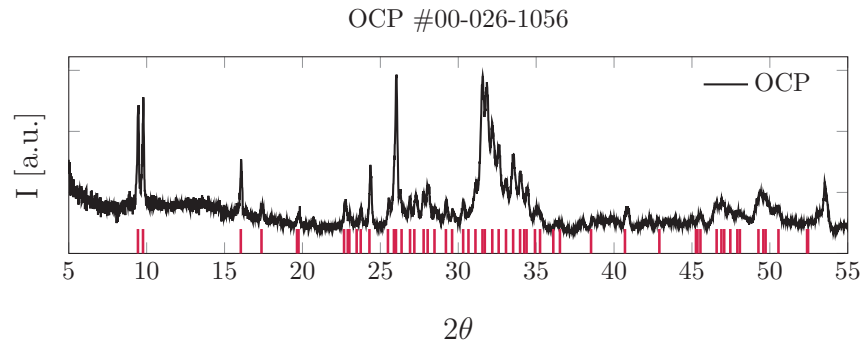


Figure S.2: The XRD-spectrum of the OCP crystals used for Raman database sample. ICDD pdf-card 00-026-1056 has been used to identify the crystal structure (shown in red lines). Reflections with less than 3 % relative intensity has been removed for clarity.

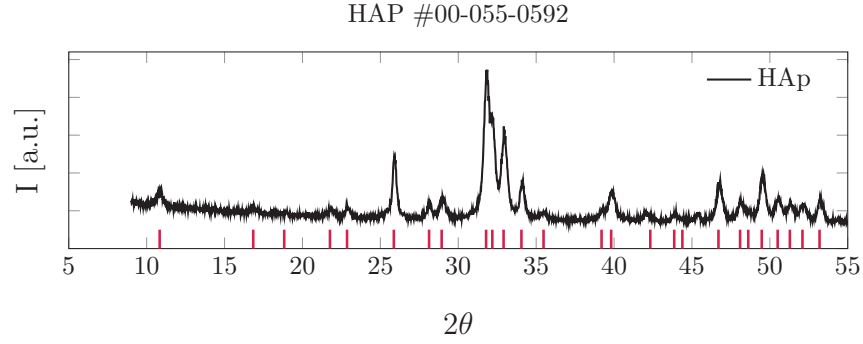


Figure S.3: The XRD-spectrum of the HAp crystals used for Raman database sample. ICDD pdf-card 00-055-0592 has been used to identify the crystal structure (shown in red lines). Reflections with less than 3 % relative intensity has been removed for clarity

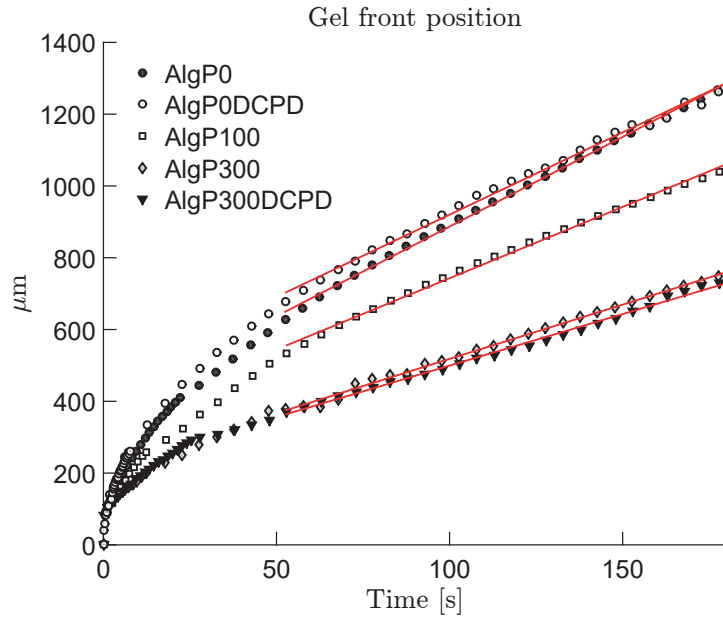


Figure S.4: Plots of typical gel front measurements at different conditions. All samples were subjected to a 1 M CaCl_2 solution at pH 5. The gel front velocity was calculated by fitting the approximately linear region of the plots. Linear fits fitted from the 50 s point are shown in red.

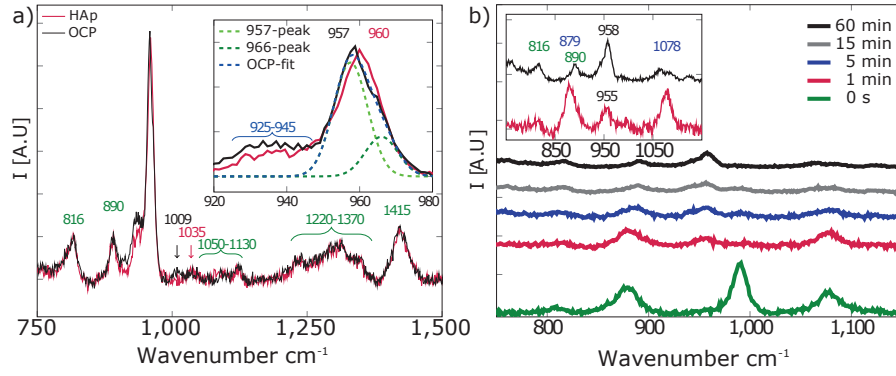


Figure S.5: **a)** A comparison of the Raman spectra of alginate with OCP and alginate with HAp. Peak designations in red and black correspond to HAp and OCP respectively. Note the HPO_4 -peak located at 1009 cm^{-1} . Peak designation in green indicate peaks arising from the alginate, while that in blue is a broad peak assigned to the acetate buffer. The inset shows details of the main peak shape. The OCP peak is shifted slightly to a lower wavenumber, and has a shoulder at 966 cm^{-1} as compared to the HAp-peak. An example of a two-peak Gaussian curve-fitting of the OCP-peak is shown. **b)** A Raman time scan for a sample gelled at pH 7. This procedure also had an initial peak around 955 cm^{-1} , however, there was a delayed appearance of the main crystalline phosphate peak as compared to samples prepared at pH 5. The inset shows details of the spectra recorded at 1 min and 60 min, highlighting the difference in the peak shape of the peak located at $955\text{--}960 \text{ cm}^{-1}$ over time.

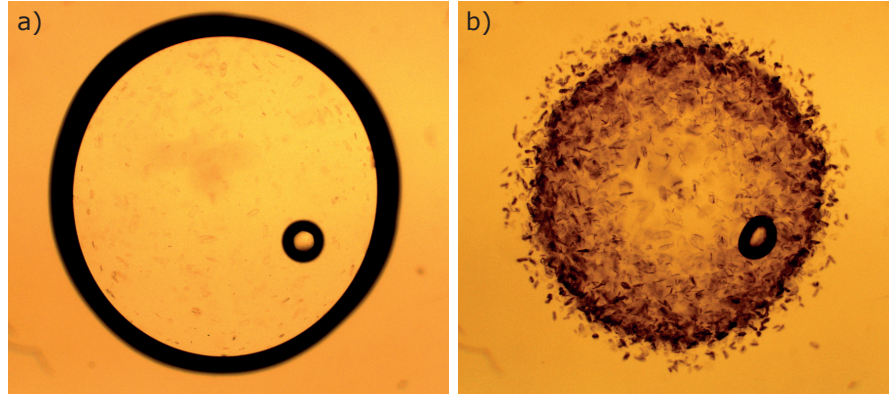


Figure S.6: An AlgP300DCPD sample ($\varnothing \approx 1.6 \text{ mm}$) shown before **(a)** and 1 h after **(b)** the introduction of CaCl_2 . Note that the brushite crystals in **a)** are barely visible as compared to **b)**. This indicated the growth of crystals across the entire sample, although it is more pronounced towards the edge of the disc.

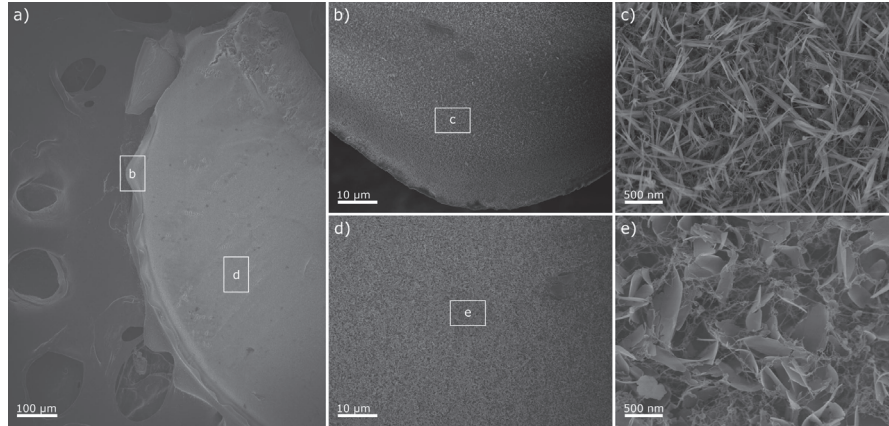


Figure S.7: **a)** shows a low magnification overview image of an AlgP300 sample stored in the mother liquor for 24 h. **b)** and **d)** are higher magnification images of the regions marked in **a)** showing the uniformity of the mineral in the respective areas. **c)** and **e)** show a more detailed crystal morphology of areas marked in the previous images.

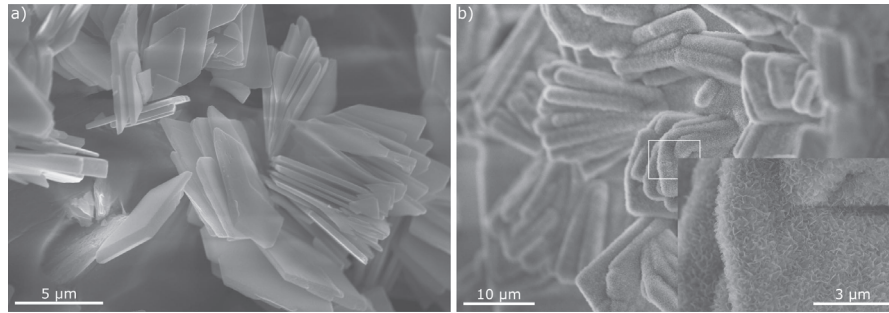


Figure S.8: A comparison of mineral located on the outer surface of an AlgP300DCPD disc prior to **(a)** and after **(b)** storage in SBF. The mineral has changed phase during incubation in SBF, but the large scale morphology remained intact, in contrast to what was observed when the discs were kept in the original gelling solution (cf. Figure 8). The inset in **b)** shows a higher magnification image of the marked region, here nanoscale HAp is evident as the *de novo* crystalline phase.

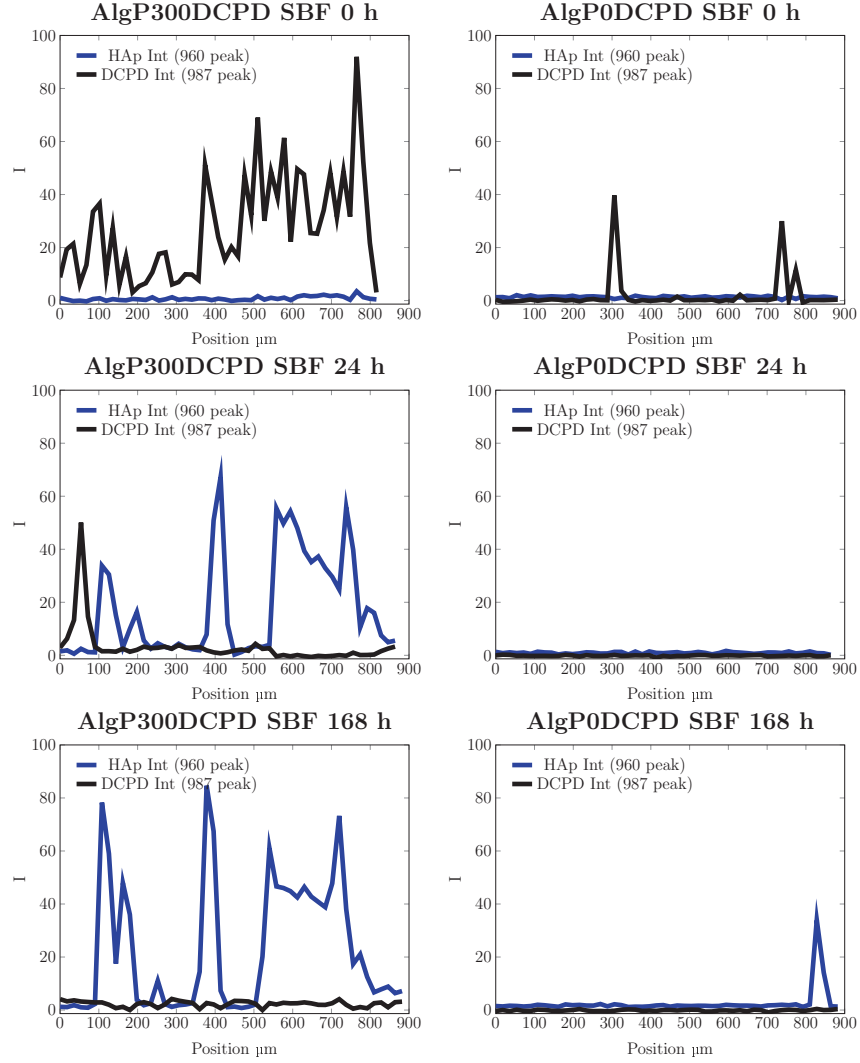


Figure S.9: A comparison of AlgP300DCPD and AlgP0DCPD (no phosphate precursor, otherwise identical) upon incubation in SBF over time. The phosphate containing sample quickly formed a broad HAp band, while there was no formation of HAp in the sample containing only brushite seeds after 24 h. After 1 week in SBF, there was complete transformation of brushite to HAp for AlgP300DCPD samples and there was a minor formation of HAp on the interface between the gelled disc and the surrounding solution for AlgP0DCPD samples.

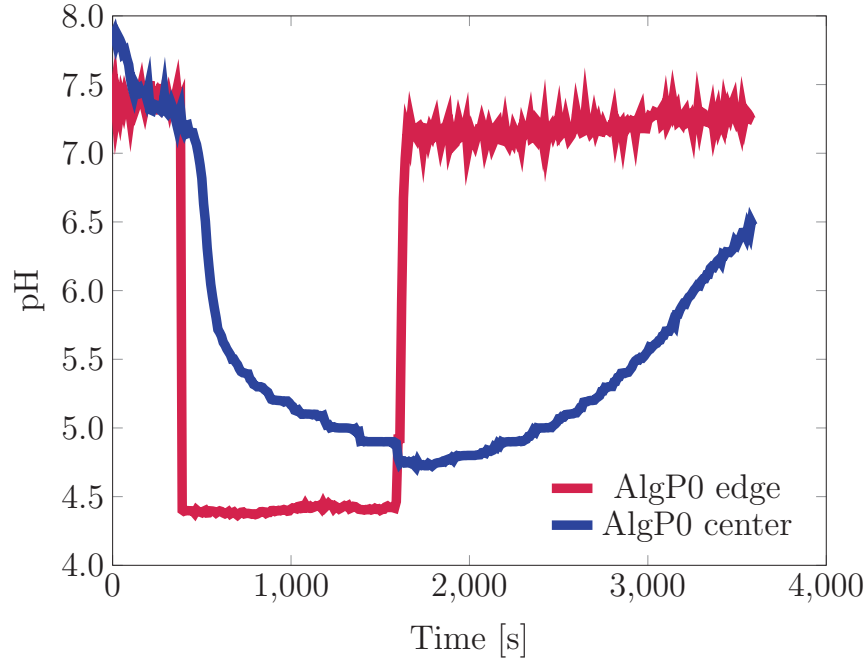


Figure S.10: A graph showing pH as a function of time at two locations for an AlgP0 sample gelled with a pH ~ 7 CaCl_2 solution and subsequently flushed with a pH ~ 4.5 solution after 400 s and a pH ~ 7 solution after 1600 s to show the rate at which the pH change as the buffers diffuse into the hydrogel. The buffers and concentrations used were the same as in the experiments in the manuscript. As the hydrogel discs were mineralized the initial formation of either amorphous CaP, OCP or brushite lead to an initial decrease in pH. One could speculate that the later transformation into the more stable HAp would sustain this lower pH, as during the transformation of OCP into HAp there is a consumption of OH^- and as brushite transforms into HAp there is also a release of H^+ . However, as the graph shows, the diffusion of buffers at this concentration into non-mineralized hydrogel discs were slow and this is probably the main cause for the sustained pH gradient between the surrounding solution and the center of the hydrogel discs, seen in Figure 10.